INFRARED MASER EMISSION FROM INTERSTELLAR HYDROXYL MOLECULES

By

Robert Frank Pelzmann, Jr.

National Aeronautics and Space Administration
Grant NGR 05-020-510

SUIPR REPORT NO. 595

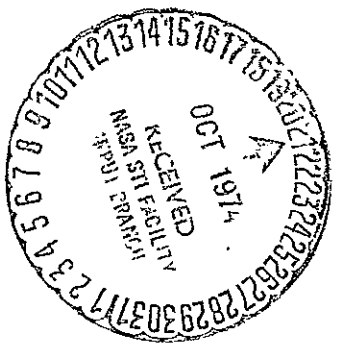

October 1974

Institute for Plasma Research
Stanford University
Stanford, California

INFRARED MASER EMISSION FROM INTERSTELLAR HYDROXYL MOLECULES

By

Robert Frank Pelzmann, Jr.

National Aeronautics and Space Administration
Grant NGR 05-020-510

SUIPR Report No. 595

October 1974

Institute for Plasma Research
Stanford University
Stanford, California

ACKNOWLEDGMENTS

Were it possible I would personally thank each person who contributed of their knowledge, understanding, or encouragement to this thesis. I would especially thank Professor Vahé Petrosian who as my mentor was the primary warden of this work. Professor Peter Sturrock's training and insight also helped crystalize this work. My appreciation also goes to Dr. John Wilcox for reading and to Ms. Evelyn Mitchell for preparing this manuscript.

I am also grateful to Drs. Larry Caroff and Ray Reynolds of the Theoretical Studies Branch of NASA Ames Research Center for their intellectual and financial support during my years of study and for their encouragement in the observational aspects of this work.

I am especially grateful to my wife Kathleen who suffered willingly the tribulations of graduate life, and to my parents whose guidance has brought me to this fulfillment of my goals.

This work was supported by the National Aeronautics and Space Administration under Grant NGR 05-020-510.

TABLE OF CONTENTS

LIST OF TABLES

LIST OF ILLUSTRATIONS

ABSTRACT

The anomalous microwave radiation from interstellar OH has been the subject of intensive investigation since its discovery in 1963. An investigation of the mechanisms put forward to explain the microwave radiation now indicates that several different far-infrared lines with wavelengths between 50 and 200 microns can also show the anomalous maser emission. Further, different pumping mechanisms produce different far-infrared lines, so that spectral studies in the far-infrared to be made in the near future will provide additional information on the conditions and pumping mechanisms of the maser regions.

The energy structure and transition rates of the OH radical have been carefully studied in rotational and vibrational energies to provide the basis for studies of the population distributions under various exciting mechanisms. The absorption of ultra-violet or near infrared radiation which Litvak and others have proposed to explain the microwave emission has been studied, as well as the absorption of low temperature blackbody radiation and collisions with molecular hydrogen. Each of these provides population inversion in some infrared lines, while dipole collisions with charged particles does not.

In applying the results of the population studies to the transfer equation a model of a uniform spherical cloud of OH is used with the pumping process occurring uniformly throughout the region. For high pumping rates the emission is unsaturated and the intensity is an exponential function of the size of the cloud. For lower pumping rates or larger sizes the region of unsaturated emission shrinks until the entire region is saturated, the intensity then becoming a linear function of the size of the emitting cloud.

— The population solutions and the intensity formula are combined to show that under the various exciting mechanisms covered far infrared line radiation between 50 and 200 microns in wavelength will be emitted isotropically from the OH clouds at intensities detectable by a 36 inch airborne infrared telescope to become operational next year at the NASA Ames Research Center. The solutions of the transfer equation may also be applied to the microwave maser emission observed from interstellar water vapor and other organic molecules to provide information on the conditions in the many dense molecular clouds which have been recently discovered. The line widths of the emission and the observed sizes of the emitting clouds is briefly considered.

CHAPTER I

INTRODUCTION

Interstellar gases are largely composed of atoms of ions at a density of about one atom per cubic centimeter. The ultraviolet radiation from stars can ionize such gases, producing electrons of temperatures characteristic of the stellar radiation, about 10^4 °K. There are also substantial amounts of neutral hydrogen and even molecular hydrogen. The gas apparently has two stable states: The first is a dilute gas of about 0.1 atoms per cubic centimeter with a high temperature and a high degree of ionization; the other state is a much denser, cooler gas cloud with large amounts of dust particles.

When a gas cloud becomes dense enough collisions can provide an important cooling mechanism. This will overcome the heating by ultraviolet radiation, allowing the gas to contract and cool further. This in turn increases the dust concentration and the opacity, and with the shrinking size of the cloud less and less heating radiation is absorbed. The dense cloud of gas and dust apparently reaches a low temperature stable state with densities near 10^4 to 10^6 atoms per cubic centimeter, and temperatures of ten to a few hundred degrees K.

These dense dust clouds have only recently received attention, partly because their darkness makes most optical observing techniques useless. Microwave and infrared radiation can easily penetrate these clouds because of the small size of the dust particles and recent advances in microwave and infrared techniques have revealed some startling characteristics in dense clouds. They represent a significant fraction of the mass of our galaxy and are important in many galactic phenomena including

the spiral structure and star formation. Most startlingly, it is in these dark clouds that many complex molecules have been discovered.

Molecules were first found in interstellar space in the 1940's when they were identified in optical spectra taken by well established techniques. Three molecular free radicals were found: CH, CH^+, and CN. The development of radio astronomy led to the discovery of the next molecule in 1963, the OH radical (Weinneb et al. 1963). These sparse discoveries and the concept that the interstellar gas is of low density and high ionization led to the expectation that molecules in interstellar space would be both rare and simple. It seemed reasonable however that dark clouds would be the most likely place for molecules because of their higher density and lower temperatures. Furthermore, the dust should provide a shield against the ionizing radiation of background stars and in 1968 a search of such clouds revealed the first polyatomic molecules, NH_3 and H_2O (Cheung et al. 1968). Both of these have convenient microwave spectra with wavelengths long enough to penetrate dense clouds easily. The organic molecule H_2CO was discovered soon afterwards, and since then the number of molecules found in interstellar space has increased rapidly. The total number of molecules and isotopes discovered has reached nearly thirty, and it seems that many others will be found as further searches are made with increasing sensitivity in microwave and infrared spectral regions.

The microwave lines of the OH radical have been observed in the absorption and emission spectra of several hundred galactic regions. The OH seen in absorption appears to be associated with regions of neutral hydrogen as suggested by line widths and radial velocities which agree closely with the observations of 21-cm hydrogen lines. In a very few

cases the four ground state OH lines are observed with intensities characteristic of local thermodynamic equilibrium, and comparison with the hydrogen observations indicates an abundance ratio of OH/H between 10^{-4} and 10^{-7}, the larger value being associated with the galactic center region.

For most of the sources neither the OH or the related H_2O have energy levels populated according to the Boltzmann distribution. This was indicated for OH shortly after its discovery in absorption by line strength ratios which differed significantly from the LTE predictions. The degree of anomalous excitation indicated by the observations of OH in emission was even more unexpected. The OH emission is now believed to result from maser amplification, but in the eight years since its discovery the most notable properties of the OH emission remain unexplained; even the mechanism which populates the energy levels is not yet known with any certainty. Several mechanisms have been proposed for populating the energy levels and this paper considers the resulting infrared line emission for the most interesting of these as a potential observational test for the relevant mechanisms.

A. Observations of OH Emission

Anomalous OH emission was discovered close to HII regions in 1965 by Gundermann (1965) and by Weaver et al. (1965). This emission was strongest at 1665 MHz and was highly polarized, usually circularly. These properties along with very small angular sizes as established by interferometry applied to all seven sources found in the following year or so. These early searches were usually made only in the two main lines and were confined to the brightest HII regions. In 1966-67, Goss (1968)

extended survey work to weaker HII regions and to galactic non-thermal continuum sources, as well as searching in all four ground state lines. More sources of the main line type were found as well as several sources of a new type which emit only at 1720 MHz and which are not associated with HII regions. This latter type of emission was subsequently found to be unpolarized. The third major class of emission sources which radiate predominantly at 1612 MHz was discovered by Wilson et al. (1970) to be associated with stellar like objects whose continuum radiation is primarily infrared. Finally, the first apparently normal OH emission of very weak intensity was found in dust clouds by Heiles (1968). By 1969, thirty anomalous OH emission sources had been discovered from the northern hemisphere and nine more from the southern hemisphere, all of which have been well studied. More recently a large number of new OH emission sources have been found associated with continuum sources (Downes 1970; Turner 1970a). Turner (1970b) proposed the following classification scheme.

B. Classification of OH Emission

Class I. These sources emit very strongly in one or both of the main lines, with the 1665 MHz line nearly always the stronger, and weakly or not at all in the satellite lines. All four lines in this class of emission sources are highly circularly polarized, with the degree of circular polarization usually being stronger for the most intense sources. Some of these sources have features that are linearly polarized to a degree higher than can be explained by resonant scattering, with no circular component. The emission profiles show little similarity among the four OH lines. They consist typically of many narrow components of widths less than 2 kHz. The line ratios in these sources vary strongly with velocity and time and

do not resemble LTE predictions; the time scales are between nine days and two months. If due to thermal broadening the linewidths correspond to temperatures below 50°K with the narrowest giving a temperature of 8°K. Very long Baseline Interferometry indicates that Class I sources with several radial velocity features are close collections of separate sources, with linear sizes about 10 AU for individual features and separations of about 100 AU for features of a single source. Continuum maps of these regions indicate that the OH emission is near the continuum centers but does not coincide. There is general evidence to associate Class I emission with infrared sources (Eliasson and Bartlett 1969; Wilson et al. 1970), and a few are associated with compact HII regions (Mezger et al. 1967). The most heavily studied of the Class I sources are in W3, Orion A, W51 a and b, DR21, Sgr B2, W49, and NGC 6334.

Class IIa. These sources show anomalous emission only in the 1720 MHz satellite line, anomalously strong absorption in the 1612 MHz line at the same radial velocity, and normal absorption in the main lines. These sources are not highly polarized, with typical values of 10% circular or linear polarization in the emission line and none in the absorption lines. These sources are speculatively associated with the shells of supernova remnants, although the distances are not known. No high resolution continuum mapping has yet been done on these because of the weakness of the emission. Typical members of this class are W28N, W44, CasA and NGC 6857.

Class IIb. This group of objects emits most strongly in the 1612 MHz line with no emission and little if any absorption in the 1720 MHz line. The two main lines show emission much weaker than either the 1612 MHz line or the main lines of Class I sources. The intensities in the 1612 MHZ

line is much stronger than the Class IIa emission and occasionally stronger than the brightest Class I objects. The 1612 MHz linewidths are typically 15 kHz with 1665 MHz linewidths about 3 kHz in the same feature. The strong satellite line is nearly unpolarized in all objects of this class, and the weaker main lines are circularly polarized to as much as 65%. All of the sources in this class are associated with IR sources listed in the CIT catalog to the resolution of VLBI measurements, with several small spots of individual sizes around 0".1 in a region about the IR star of 2" extent. Objects in this class include VY Ca Maj, NML Cyg, NML Tau, CIT 3, and CIT 7.

Class III. Heiles (1968) discovered weak OH emission with LTE line ratios in a number of dark dust clouds. Both the clouds and the OH emission are extended, up to 2^{o} in one case. There is no continuum radio emission and little or no 21 cm hydrogen emission. The excitation temperatures are about 5^{o}K with densities greater than 10^{+6} molecules per cubic centimeter. There is no apparent polarization in any of the lines in these sources, typical of the thermal characteristics. Careful observations by Turner and Heiles (1970) indicate some anomalies in the 1612/1720 satellite line ratio similar to, but weaker than, the Class IIa objects. There is some speculation (Booth 1972) that this class is a weak case of Class IIa or b.

C. Characteristics of Two Strong OH Sources

The largest infrared telescopes available for observations beyond 100 microns are less than 1 meter in aperture, so that sensitivity is rather poor in comparison with radio detectors. The far infrared radiation detectable from the OH molecule will probably come from the strongest OH radio sources. Any reasonable pumping mechanism for the ground state maser emission will involve infrared transitions so that the infrared

brightness temperatures will be related to the microwave emission by the ratio of the wavelengths, hence about 10^8K. The limited sensitivity of the IR telescopes restricts detectability to the brightest of the OH sources. For this reason, we will consider modeling the two brightest class I sources, Orion A and W3, in later chapters.

The W3 source consists of several spots of emission about 8 AU in size in a circular arc about 3000 AU across. Microwave emission has been detected in the ground state and in four excited states, $^2\Pi_{3/2}j$ = 3/2, 5/2, 7/2, and $^2\Pi_{1/2}j$ = 1/2 and 5/2. The relative intensities in these lines are 1.00, 0.03, 0.06, and 0.01, 0.0005 respectively. The emission in the $^2\Pi_{1/2}j$ = 5/2 lines may be a false detection (Turner 1972). W3 is associated with a compact HII region as well as a point infrared source. The brightness temperature of the 1665 MHz line is about 10^{13} ^oK and the linewidth about 0.8 kHz. There is also an anomalous H_2O emission source nearby. Time variations are seen of the order of a few weeks in the 1665 and 1667 MHz lines, but with no correlation between them. The polarization remains constant with time during these intensity variations. The total intensity in the lines assuming spherical emission is about 10^{28} ergs per second.

The Orion A source is apparently a single small spot about 3×10^{13} centimeters across with a nearby IR point source and a large background IR nebula. The brightness temperature is about 10^{12} ^oK and the linewidth 10 kHz. There is an H_2O emission source correlated with the OH source which has a brightness temperature greater than 10^{14} ^oK.

D. Summary

In the following chapters we will discuss in detail the energy structure of the OH molecule, specifically the $^{16}O^{1}H$ isotope, and calculate the transition rates. This information will be applied to the pumping mechanisms to predict the population distributions for varying parameters of the OH regions. The equation of transfer for a simplified spherical region will be solved for various degrees of saturation and analyzed for relevant emission characteristics. Finally, the two results will be combined to predict the expected detectable infrared emission for some typical OH sources and to describe the relevant physical conditions in the OH regions.

CHAPTER II

THE MATHEMATICAL FORMULATION FOR OH MASERS

A. Notation of the Energy States

The energy structure of the OH molecule is as complicated as any diatomic molecule, with contributions from the electronic excitation, the internuclear vibration, the molecular rotation, the electron spin, the nuclear spin, and the interaction of each of these with the others. There are no less than nineteen quantum numbers appropriate to the description of the energy levels of the two electronic states of interest in the pumping mechanisms of OH masers. The following description of these quantum numbers is a useful adjunct to the understanding of the energy structure and the emission which accompanies an OH maser.

The coupling between the two nuclei of the molecule can be described as a nonlinear spring, or quantum mechanically as a particular potential function of the separation. Vibration of the molecule in this potential is quantized, and described by the vibration number V. This is the only energy in the molecule which has no atomic equivalent.

The motion of the electrons in an atom takes place in a spherically symmetric field, hence the electronic orbital angular momentum $\underline{L}$ is a constant of the motion. In a diatomic molecule the symmetry of the field is only axial and as a consequence only this component of the orbital angular momentum is a constant of the motion. A precession of $\underline{L}$ occurs about the internuclear axis with a component along the axis of M_L, which takes the allowed values of L, L-1, L-2, ..., -L. In the absence of perturbations the states with M_L values of opposite sign have the same energy, thus the component of the electronic orbital angular momentum is:

$$\Lambda = |M_L| \ .$$

Note that except for $\Lambda = 0$ the states are twofold degenerate. In a manner similar to atomic states, these molecular states are designated as Σ, Π, Δ, Φ, ... according to $\Lambda = 0, 1, 2, 3, \ldots$ respectively.

The wavefunction of the molecule in these axially degenerate states may be written in a manner which expresses the symmetry characteristics of the molecule:

$$\psi_e^{+} = \chi_e e^{i\Lambda\varphi} + \bar{\chi}_e e^{-i\Lambda\varphi}$$
$$\psi_e^{-} = \chi_e e^{i\Lambda\varphi} + \bar{\chi}_e e^{-i\Lambda\varphi} \qquad \text{(II-A-1)}$$

hence the degenerate states may be written as Σ^+, Σ^-, Π^+, Π^-, ... The separation of the symmetry states by Λ-doubling perturbations will be discussed later.

A closer investigation of the structure of electronic states shows a multiplet structure due to electron spin just as in atomic states. The spins of the individual electrons form a resultant $\underline{S}$ with the quantum number S being half-integral for molecules with an odd number of electrons such as OH. For $\Lambda = 0$ the resultant $\underline{S}$ is fixed in space as long as the molecule is not rotating. In $\Lambda \neq 0$ states the orbital motion of the electrons gives rise to an internal magnetic field which causes a precession of $\underline{S}$ about the internuclear axis with a component Σ along the axis with the values $S, S-1, S-2, \ldots, -S$. Σ is not a well defined quantum number for $\Lambda = 0$.

The total electronic angular momentum about the internuclear axis is the combination of orbital motion and spin. The quantized component of that total along the axis is $\Omega = |\Lambda + \Sigma|$. For $\Lambda \neq 0$ the electronic state splits into $2S + 1$ levels. Additional angular momentum in the

molecule is contained in gross rotation of the molecule and in nuclear spin. The nuclear spin quantizes just as the electron spin, with resultant $\underline{I}$ and component Ω_I. The nuclear spin splits the states into $2I + 1$ further substates. The rotation of the molecule occurs perpendicular to the axis, with a resultant $\underline{O}$. Table 1 summarizes the quantum numbers in diatomic molecules.

The several forms of angular momenta in the molecule can interact in different ways. Hund first studied the various coupling schemes in detail, and his cases (a) and (b) are of interest (Herzberg 1950). In the OH molecule, the ground state ($\Lambda = 1$, a Π state) is intermediate between case (a) and case (b), and the first excited state ($\Lambda = 0$, a Σ state) is a pure case (b).

In Hund's case (a) the interaction of the molecular rotation with the electronic motion is weak, and the electronic motion is coupled strongly to the internuclear axis. The vector diagram for this is:

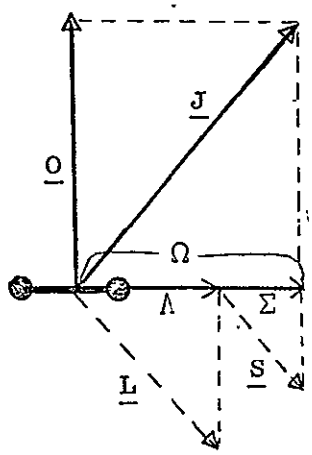

The quantum number for the rotation can take the values Ω, $\Omega+1$, $\Omega+2$, ...

TABLE 1. THE QUANTUM NUMBERS FOR DIATOMIC MOLECULES

Nuclear spin	I
projection on molecular axis	Ω_I
projection on space axis	M_I
Electron spin	S
projection on molecular axis	Σ
projection on space axis	M_S
Electron orbital angular momentum	L
projection on molecular axis	Λ
projection on space axis	M_L
Molecular rotation	O
Total orbital angular momentum	N
projection on molecular axis	K
Total angular momentum without nuclear spin	J
projection on molecular axis (absolute value)	Ω
projection on space axis	M_J
Total angular momentum	F
projection on molecular axis	Ω_F
projection on space axis	M_F
Vibration	V

In Hund's case (b) the spin is only weakly coupled to the internuclear axis, hence the electronic orbital angular momentum and the rotation form a resultant $\underline{N}$ and its quantum number can take the values Λ, $\Lambda+1$, $\Lambda+2$, ... The angular momentum $\underline{N}$ and the spin $\underline{S}$ then couple to form the total angular momentum $\underline{J}$ with quantized values $N+S$, $N+S-1$, ..., $N-S$. The vector diagram for this case is:

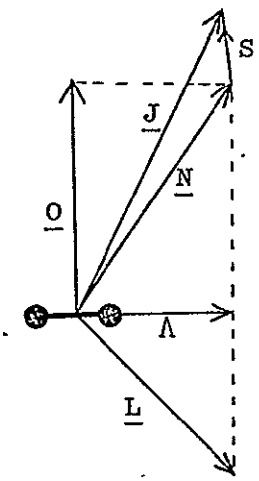

B. Calculation of the Energy Levels

As mentioned above the energy of an OH molecule is in several forms. Since it is known that the energies associated with the interactions of the various motions of the molecule are much smaller than the energies of those motions, those interactions can be considered as perturbations in deriving the expressions for the energy structure of the OH molecule.

In all cases the energy expressions in this paper will be given in term values of cm^{-1} so that the energy differences will be directly in units of inverse wavelength. To determine the energy in more common units the expressions should be multiplied by Planck's constant and by the speed of light ($h \times c$).

The energy states of interest in the pumping mechanisms are the rotation levels of the ground vibration state in the first excited electronic state, that is the J levels of the $V = 0$ state of $\Lambda = 0$ (the Σ electronic state); and the vibration and rotation levels of the ground electronic state, that is the J and V levels of $\Lambda = 1$ (the Π state). The Σ doublets of opposite symmetry will be considered, as will the Π levels split by symmetry, electron spin, and nuclear spin. Figure 1 diagrams the labeling and order of the states for $\Lambda = 0$, and Figure 2 shows the typical pattern of the $\Lambda = 1$ ground state for each vibration level. The levels in the Π scheme are further split by the action of the unpaired nuclear spin which is shown in Figure 3 for a typical J doublet.

The vibration energy of a diatomic molecule is easily separated from the other forms of energy. With the vibration quantized by $V = 0, 1, 2, \ldots$ the vibration term value is:

$$G(V) = \omega_e\left(V + \frac{1}{2}\right) - \omega_e\chi_e\left(V + \frac{1}{2}\right)^2 + \omega_e y_e\left(V + \frac{1}{2}\right)^3 \qquad \text{(II-B-1)}$$

where the constants ω_e, χ_e, y_e are determined experimentally for each electronic state, and higher order terms are ignored. The vibration may interact with the electronic motion of the molecule by altering the average moment of inertia of the molecule. This is taken into account by writing the rotational constants of the molecule as functions of the vibration number:

$$B_e^{(1)} = B_e + \alpha_e\left(V + \frac{1}{2}\right) + \beta_e\left(V + \frac{1}{2}\right)^2$$

$$D_e^{(1)} = D_e + \beta_e\left(V + \frac{1}{2}\right); \quad D_e = \frac{4B_e^3}{\omega_e^2} \qquad \text{(II-B-2)}$$

Figure 1. The Σ energy levels

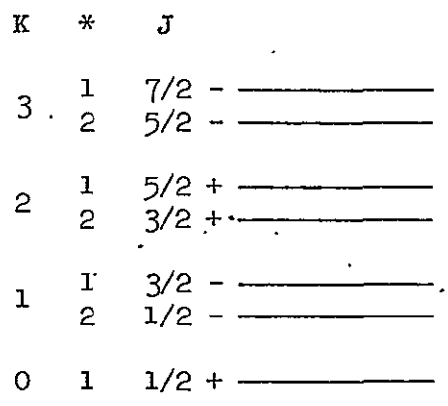

Figure 2. The Π energy levels for each vibration state

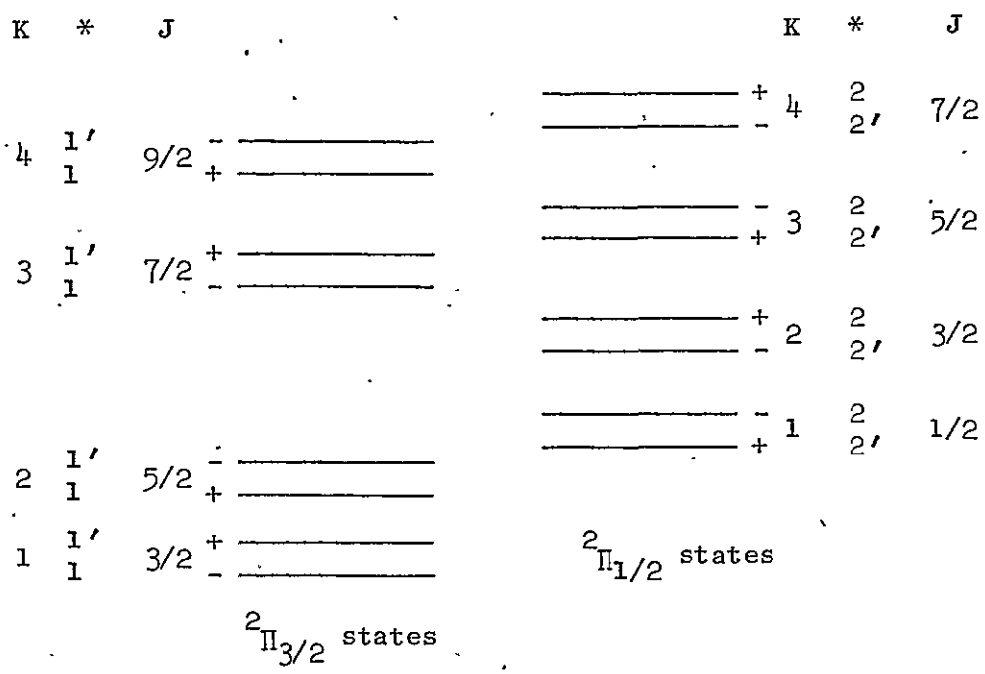

Figure 3. The hyperfine structure

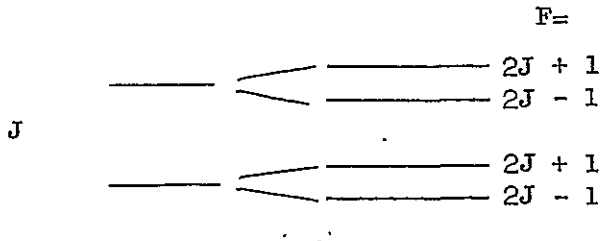

*This is the label of the spin splitting. The prime refers to the Λ-doublets.

where higher order terms are again ignored. The subscripts used in (II-B-1) and (II-B-2) refer to the electronic state being considered. The letter p will be used for the Π states and s for the Σ states throughout this paper.

The rotational and electronic energies of the molecule take a more complicated form. After Van Vleck (1929) the hamiltonian of the molecule including the electronic and rotational terms and the $\underline{L} \cdot \underline{S}$ interaction may be written:

$$H = B[J(J+1)-\Lambda^2] + BS(S+1) + AL_zS_z - 2B\underline{J} \cdot \underline{S} + B(L_x^2+L_y^2)$$

$$+ (2B+A)(L_xS_x+L_yS_y) - 2B(J_xL_x+J_yL_y) \quad . \qquad \text{(II-B-3)}$$

Here the $\underline{z}$ direction is along the internuclear axis, A and B are the fine structure interaction and rotation constants, and the quantum numbers have been described. The term $B(L_x^2+L_y^2)$ is nearly constant and will be ignored since it only shifts the energy by a constant amount (see also Fontana 1962; Hill and Van Vleck 1928).

The eigenvalues of the wave equation with the above hamiltonian are needed. There are six states to be considered: $\Pi_{3/2}$, $\Pi_{-3/2}$, $\Pi_{1/2}$, $\Pi_{-1/2}$, $\Sigma_{1/2}$, $\Sigma_{-1/2}$. The interactions between all pairs of states form a six-by-six determinent that factors into two three-by-three determinents by using the symmetric-antisymmetric wavefunctions mentioned previously. Using the matrix elements of Van Vleck one determinent is:

$$\begin{vmatrix} k-\lambda & \mu & \eta \\ \mu^* & \beta-\lambda & \varepsilon \\ \eta^* & \varepsilon^* & \gamma-\lambda \end{vmatrix} \qquad \text{(II-B-4)}$$

with:

$$k = \alpha + \delta \,, \quad \mu = \theta + \xi \tag{II-B-5}$$

and the matrix elements are listed in Table 2. The other cubic determinent is identical except:

$$k = \alpha - \delta \,, \quad \mu = \theta - \xi \,. \tag{II-B-6}$$

The eigenvalues may be found by diagnolizing the above to successively higher order (Dousmanis et al. 1955).

The zero order terms are the energies of the Π state with no interactions ($\mu = \eta = 0$):

$$\begin{aligned} \lambda_1^{(0)} &= k \\ \lambda_{2,3}^{(0)} &= \pm \frac{1}{2} \left[(\beta-\gamma)^2 + 4\varepsilon^2 \right]^{1/2} + \frac{1}{2} (\beta+\gamma) \,. \end{aligned} \tag{II-B-7}$$

The zero order energies then are:

$$\begin{aligned} E^{(0)}_{\Sigma^{\pm}} &= E + B_s[J + 1/2][J + 1/2 \pm 1] \\ E^{(0)}_{\Pi_{1/2,3/2}} &= B_p(J + 3/2)(J - 1/2) \pm \frac{1}{2} B_p \sqrt{4(J + 1/2)^2 + \lambda(\lambda-4)} \,. \end{aligned} \tag{II-B-8}$$

Note that to this order, not even the symmetry differences in the Π state are split. The interaction between the Σ and π states in first and second order is needed to describe this splitting.

We proceed by expanding the determinent (5) and writing the eigenvalues as perturbations of the zero order terms above:

TABLE 2. THE MATRIX ELEMENTS OF THE HAMILTONIAN (Van Vleck 1929)

$$\alpha = B_s[J(J+1) + 1/4] + E$$

$$\beta = B_p[J(J-1) + 1/4] - \frac{1}{2} A$$

$$\gamma = B_p[J(J+1) - 7/4] + \frac{1}{2} A$$

$$\delta = B_s(J + 1/2)$$

$$\varepsilon = B_p[(J - 1/2)(J + 3/2)]^{1/2}$$

$$\xi = 2(J + 1/2)\langle \Pi | BL_y | \Sigma \rangle$$

$$\eta = 2[(J - 1/2)(J + 3/2)]^{1/2}\langle \Pi | BL_y | \Sigma \rangle$$

$$\theta = \langle \Pi | AL_y + 2\, BL_y | \Sigma \rangle$$

$$E = E_\Sigma - E_\Pi$$

$$k\beta\gamma + \mu\varepsilon\eta^* + \eta\mu^*\varepsilon^* - \beta\eta\eta^* - \gamma\mu\mu^* - k\varepsilon\varepsilon^*$$

$$- (k\beta + k\gamma + \beta\gamma - \varepsilon\varepsilon^* - \mu\mu^* - \eta\eta^*)\lambda + (k + \beta + \gamma)\lambda^2 - \lambda^3$$

$$= (\lambda - \lambda_1)(\lambda - \lambda_2)(\lambda - \lambda_3) \qquad \text{(II-B-9)}$$

where:

$$\lambda_i = \lambda_i^{(0)} + \lambda_i^{(1)} , \quad i = 1,2,3 . \qquad \text{(II-B-10)}$$

If the λ from (II-B-10) are inserted in (II-B-9) and terms higher than first order in $\lambda_i^{(1)}$ are omitted, these first order corrections to (II-B-7) are found:

$$\lambda_1^{(1)} = (\mu\mu^* + \eta\eta^*)/E$$

$$\lambda_{2,3}^{(1)} = \frac{(\mu\mu^* + \eta\eta^*)}{2E} \mp \frac{1}{EB_pX}\left[\frac{(\beta-\gamma)(\mu\mu^* - \eta\eta^*)}{2} + \mu\varepsilon\eta^* + \mu^*\varepsilon^*\eta\right] \qquad \text{(II-B-11)}$$

where

$$X = +[4(J + 1/2)^2 + (y-4)y]^{1/2} \qquad y = A/B_p . \qquad \text{(II-B-12)}$$

This procedure is repeated, writing:

$$\lambda_i = \lambda_i^{(0)} + \lambda_i^{(1)} + \lambda_i^{(2)} \qquad \text{(II-B-13)}$$

for the second order corrections. Using this in equation (ii-B-9) gives the complex expressions for the perturbations:

$$\lambda_1^{(2)} = \frac{1}{E^2}\left[\mu\mu^*\beta + \pi\pi^*\gamma + \eta\mu^*\varepsilon^* - \left(\pi\eta^* + \mu\mu^*\right)\left(\alpha - E + \delta\right)\right]$$

$$\lambda_{2,3}^{(2)} = \frac{\pm 1}{E^2 B_p X}\left[\left(\mu\mu^* + \pi\eta^*\right)\left(\frac{(\beta+\gamma)^2 - B_p^2 X^2}{4}\right) - \left(\mu\mu^*\beta + \pi\eta^*\gamma + \mu\varepsilon\eta^* + \eta\mu^*\varepsilon^*\right)\right.$$

$$\times\left(\frac{\beta+\gamma \pm B_p X}{2}\right) - \left(\alpha - E + \delta\right)\left(\beta\eta\eta^* + \gamma\mu\mu^* - \mu\varepsilon\eta^* - \mu^*\varepsilon^*\eta\right)$$

$$+ \left(\alpha - E + \delta\right)\left(\pi\eta^* + \mu\mu^*\right)\left(\frac{\beta+\gamma \pm B_p X}{2}\right)$$

$$+ \frac{1}{B_p^2 X^2}\left[\left(\beta-\gamma\right)^2\mu\mu^*\pi\eta^* + \varepsilon\varepsilon^*\left(\mu^2\mu^{*2} + \eta^2\eta^{*2}\right)\right.$$

$$\left.\left. - 2\mu\mu^*\pi\eta^*\varepsilon\varepsilon^* - \left(\beta-\gamma\right)\left(\mu\mu^* - \pi\eta^*\right)\left(\mu\varepsilon\eta^* + \eta\mu^*\varepsilon^*\right)\right]\right] . \qquad \text{(II-B-14)}$$

The upper of the double signs in equation (II-B-14) corresponds to the $\Pi_{1/2}$ state and the lower to the $\Pi_{3/2}$ state of the OH molecule.

Evaluating the energy terms of equations (II-B-7), (II-B-11), and (II-B-14) with the matrix elements of Table 2 gives the energy levels of the molecule with λ_1 giving the energy of the Σ states and λ_2 and λ_3 giving the energy of the $\Pi_{1/2}$ and $\Pi_{3/2}$ states. For the Π states, the energy is written:

$$W = W_1 \pm \frac{1}{2} W_2 \qquad \text{(II-B-15)}$$

where W_2 explicitly is the Λ-doubling energy splitting. W_2 may be expressed as a sum of first and second order terms:

$$W_2 = W_\Lambda^{(1)} + W_\Lambda^{(2)} . \qquad \text{(II-B-16)}$$

The expressions for the energy of the Π states are:

$$W_1 = B_p'(J - 1/2)(J + 3/2) \pm \frac{B_p'' X}{2} + C_1$$

$$\mp \frac{\alpha_p}{X}\left[\left(J-1/2\right)\left(J+3/2\right)\left(1+\frac{B_p}{E}\left(J-1/2\right)\left(J+3/2\right)-\frac{B_s}{E}\left(J+1/2\right)^2-\left(\frac{2-\lambda}{2}\right)\frac{B_s}{E}\left(J+1/2\right)^2\right)\right]$$

$$\mp \frac{\beta_p}{2X}\left[\left(2-\lambda\right)\left(1+\frac{B_p}{E}\left(J-1/2\right)\left(J+3/2\right)-\frac{B_s}{E}\left(J+1/2\right)^2\right)+\frac{B_p X^2}{E}J\left(J+1\right)\right.$$

$$\left.-\frac{4B_s}{E}\left(J+1/2\right)^2\left(J-1/2\right)\left(J+3/2\right)\right]$$

$$\mp \frac{\alpha_p^2}{8\beta_p}\left(\frac{2-\lambda}{X}\right)\left[1+\frac{B_p}{E}\left(J-1/2\right)\left(J+3/2\right)-\frac{B_s}{E}\left(J-1/2\right)^2\right]$$

$$\mp \frac{(J-1/2)(J+3/2)}{B_p X^3}\left[\alpha_p^2\left\{\left(\frac{2-\lambda}{2}\right)^2+J(J+1)+3/4\right\}+\beta_p^2(J+1/2)^2\left[\left(2-\lambda\right)^2+1\right]\right.$$

$$\left.-2\alpha_p\beta_p(2-\lambda)[J(J+1)+3/4]+\frac{\alpha_p^4}{16\beta_p^2}-\frac{\alpha_p^3(2-\lambda)}{4\beta_p}\right]$$

$$-\frac{\beta_p(B_p-B_s)}{E}J^2(J+1)^2 \qquad \text{(II-B-17)}$$

where

$$B_p' = B_p-\beta_p\left(1-\frac{B_p}{E}\right)-\alpha_p\left(1+\frac{\alpha_p}{4\beta_p}\right)\left(\frac{B_p-B_s}{2E}\right)$$

$$B_p''' = B_p\left(1-\frac{\alpha_p^2-2B_p^2}{8\beta_p E}\right) \qquad \text{(II-B-18)}$$

$$C_1 = \frac{-\alpha_p^2}{8\beta_p}\left(1-\frac{\lambda B_p}{2E}+\frac{B_p-B_s}{E}\right)-\frac{1}{2}\beta_p\left(1+\frac{\lambda B_p}{2E}-\frac{B_p-B_s}{8E}\right)+\frac{\alpha_p B_s}{2E}$$

and

$$W'_\Lambda = -\alpha_p(J + 1/2)\left(\frac{\pm X+2-\lambda}{\pm X}\right) \mp \frac{4\beta_p}{X}(J-1/2)(J+1/2)(J+3/2) \qquad \text{(II-B-19)}$$

and

$$W^2_\Lambda \pm \frac{(J+1/2)\alpha_p}{EX}\left[\left(2\left(J-1/2\right)\left(J+3/2\right) \pm X\right)\left\{\left(B_s-B_p\right)\left(J+1/2\right)^2 + B_p\left(\frac{\lambda \mp X}{2} + \left(J-1/2\right)\left(J+3/2\right)\right)\right\}\right.$$

$$\left. - 2B_s\left(\left(J+1/2\right)^2\left(J\left(J+1\right)-7/4+\lambda/2\right) - \left(J-1/2\right)\left(J+3/2\right)\right)\right]$$

$$\pm \frac{(J+1/2)}{EX}\beta_p\left[\left(2\left(J-1/2\right)\left(J+3/2\right) \pm X\right)\left(2B_s\left(J\left(J+1\right)-1/4\right) - 2B_p\left(J-1/2\right)\left(J+3/2\right)\right)\right.$$

$$\left. + B_s\left(2\left(J+1/2\right)^2-\lambda\right)\right]$$

$$\mp \frac{(J+1/2)\alpha_p^{\,2}}{EX\ 4\beta_p} B_s(\lambda - 2 \mp X)$$

$$\mp \frac{C_2(J-1/2)(J+1/2)(J+3/2)}{B_p X^3} \qquad \text{(II-B-20)}$$

where

$$C_2 = -2\alpha_p\beta_p(\lambda^2-4\lambda+6) + (3\alpha_p^{\,2} + 4\beta_p^{\,2})(2-\lambda) - \alpha_p^{\,3}/\beta_p \ . \qquad \text{(II-B-21)}$$

In equations (II-B-17) to (II-B-21) the upper sign corresponds to the $\Pi_{1/2}$ states of the OH molecule and the lower sign to the $\Pi_{3/2}$ states (Dousmanis 1955).

Equations (II-B-7), (II-B-12), and (II-B-14) may be evaluated for the energies of the Σ state. For each rotational level with rotational quantum number N there are two states that correspond to the two orientations of $\underline{S}$ with respect to $\underline{N}$ in the OH molecule. For these paired levels the energy is given by:

$$W_{\Sigma^{\pm}} = C_3 + B_s'N(N+1)$$

$$\pm \left[\alpha_s\left(1 - \frac{\lambda B_p}{2E}\right) - 2\beta_s\left(1 - \frac{B_p}{2E}\right) - \frac{\alpha_s^2 B_p}{4\beta_s E}\right](N+1/2)$$

$$\pm (\alpha_s - 2\beta_s)\left(\frac{B_p - B_s}{E}\right) N(N+1)(N+1/2)$$

$$+ 2\beta_s\left(\frac{B_p - B_s}{E}\right) N^2(N+1)^2 \qquad \text{(II-B-22)}$$

where:

$$C_3 = E - \frac{\alpha_s}{2}\left[1 + \left(\frac{4-\lambda}{2}\right)\frac{B_p}{E}\right] + \frac{\beta_s B_p}{2E}(3-\lambda) + \frac{\alpha_s^2}{4\beta_s}\left[1 + \left(\frac{1-\lambda}{2}\right)\frac{B_p}{E}\right]$$

and

$$B_s' = B_s + 2\beta_s\left(1 - \frac{B_p}{E}\right) - \alpha_s\left(\frac{B_p - B_s}{2E}\right) + \frac{\alpha_s^2}{4\beta_s}\left(\frac{B_p + B_s}{E}\right).$$

There is only one other effect that must be accounted for to model the energy of the OH molecule to the accuracy of the second order terms given above. The rotation of the molecule alters the effective equilibrium position of the mass-spring-mass model. This increases the moment of inertia with increasing rotation and can be expressed by modifying the rotation constant in addition to the expression (II-B-2) which corrects for the average moment of inertia due to vibration. We write:

$$B_e^{(2)} = B_e^{(1)}\left[1 - \frac{D_e}{B_e} f_e\right]. \qquad \text{(II-B-23)}$$

The higher order terms in (II-B-3) may also be similarly corrected:

$$\alpha_e = \alpha_e\left(1 - C_e \frac{D_e}{B_e} f_e\right)$$
$$\beta_e = \beta_e\left(1 - F_e \frac{D_e}{B_e} f_e\right) \qquad \text{(II-B-24)}$$

For Π states:

$$f_p = J^2 + \left(\frac{\mp X + 2(J+1/2) - \frac{\lambda}{J+1/2}}{\mp X}\right)(J+1/2) \quad . \qquad \text{(II-B-25)}$$

For Σ states:

$$f_s = N(N+1) \quad . \qquad \text{(II-B-26)}$$

The upper signs in (II-B-24) are for the $\Pi_{1/2}$ states and the lower ones for the $\Pi_{3/2}$ states.

The expressions (II-B-22) give the energies of the Σ states to sufficient accuracy for our purpose. Expressions (II-B-17) to (II-B-20) give the energy of the Π states to the resolution of the Λ-doubling. The states are further split as mentioned by the action of the nuclear spin. To the accuracy of the above expressions, this hyperfine splitting is given by $W^* = W + W_{hf}$ where

$$W_{hf} = \frac{1}{\pm 4X}\left\{2a(\pm 2X + 2-\lambda) + b\left[4(J-1/2)(J+3/2) \pm X + 4-2\lambda\right]\right.$$
$$\left. + C(\pm X + 4-2\lambda) \pm \frac{d}{2}\left(\frac{\pm X-2+\lambda}{\pm 2X}\right)(J+1/2)\right\} \frac{\underline{I}\cdot\underline{J}}{J(J+1)} \qquad \text{(II-B-27)}$$

where

$$\underline{I} \cdot \underline{J} = \frac{F(F+1) - J(J+1) - I(I+1)}{2} . \qquad \text{(II-B-28)}$$

The upper sign in front of X in (II-B-27) applies to the $^2\Pi_{3/2}$ state while the lower one applies to the $^2\Pi_{1/2}$ state. Only the d term above will give rise to any splitting of the energy levels, since the upper sign here corresponds to the hyperfine level with $F = J + 1/2$ while the lower sign is for the $F = J - 1/2$ level. The other terms only make the splitting asymmetrical about the Λ-doublet level. For transitions between the rotational levels the b term will shift the hyperfine lines slightly from the unsplit frequency.

No further splitting of the $^2\Pi$ levels will occur without the application of an external field. A magnetic field will split each hyperfine level into $2F + 1$ magnetic sublevels which can give rise to polarization in the emission, but these splittings and the hyperfine splittings are smaller than the typical width of the far infrared lines, and certainly smaller than the resolving ability of current infrared spectroscopes.

C. The Molecular Constants and the Energy Levels

The spectrum of the OH molecule and its isotopes has been observed by several groups. A reasonably accurate fit of their data to the previous formulae for the energy levels gives the following set of molecular constants (Herzberg 1950; Dousmanis et al. 1955; Dicke and Croswhite 1962):

$^{16}O^{1}H$	Π	Σ
ω_e	3735.21 cm^{-1}	3184.28 cm^{-1}
$\omega_e\chi_e$	82.81 "	97.87 "
$\omega_e y_e$	--	--
B_e	18.871 "	(17.355) "
α_e	-0.7703 "	-0.807 "
β_e	0.0192 "	-0.0083 "
E_e	0	35.875 "
Y_e	-7.444*	--
C_e	0.60	--
F_e	1.20	--

The hyperfine constants that have been measured are:

$$a = 0.002 \text{ cm}^{-1} ,$$

$$d = 0.00190 \text{ cm}^{-1} .$$

The energy levels in cm^{-1} resulting from this set of values and the previous formulae are listed in Table 3, where f_1 and f_1' are the Λ-doublet levels in the $\Pi_{3/2}$ state and f_2 and f_2' are the doublet levels in the $\Pi_{1/2}$ state. K is given by $K = J - 1/2$ for the $\Pi_{3/2}$ state and by $K = J + 1/2$ for the $\Pi_{1/2}$ state. Table 4 gives the

*The value of the intermediate coupling strength is not constant for all vibration levels. Rather it has been shown to vary, and the most commonly reported values are (Benedict et al. 1953):

v =	0	1	2	3	4
λ =	-7.444	-7.876	-8.214	-8.568	-8.96

TABLE 3. ROTATIONAL AND VIBRATIONAL LEVELS OF THE Π STATE OF OH (IN cm^{-1})

K	f_1	f_1'	f_2	f_2'
		V = 0		
1	00.00	00.05	126.43	126.12
2	83.70	83.90	187.71	187.47
3	201.90	202.37	289.01	288.83
4	355.09	355.87	429.45	429.23
5	543.54	544.82	608.15	608.16
		V = 1		
1	3568.31	3568.49	3695.34	3695.03
2	3649.10	3649.28	3754.15	3753.95
3	3763.03	3763.40	3851.38	3851.10
4	3910.55	3911.26	3986.14	3985.99
5	4091.95	4093.10	4157.80	4157.75
		V = 2		
1	6971.02	6971.18	7097.38	7097.30
2	7048.85	7049.16	7155.11	7155.20
3	7158.60	7159.00	7248.20	7248.02
4	7300.50	7301.24	7377.48	7377.32
5	7474.98	7476.04	7542.10	7542.10
		V = 3		
1	10210.31	10210.77	10335.27	10337.60
2	10284.31	10284.40	10390.21	10392.22
3	10390.59	10390.94	10480.59	10481.33
4	10526.99	10527.54	10605.22	10605.07
5	10694.61	10695.47	10763.00	10763.07

TABLE 4. ROTATIONAL LEVELS OF THE Σ STATE OF OH (IN cm^{-1})

K	F_1	F_2
0	32440.61	
1	32474.62	32474.30
2	32542.56	32541.98
3	32644.22	32643.45
4	32779.49	32778.49
5	32948.31	32947.05

energies for the Σ state. In this case F_1 and F_2 are the + and - symmetry states of a given N. They are labeled in J according to $J = N + 1/2$ for F_1 and $J = N - 1/2$ for F_2. The symmetry is labeled + for N = even and - for N = odd in the Σ state. The f_i levels are + symmetry for K = even and - for K = odd, while the f_i' levels are - for K = even and + for K = odd. Figures 1, 2, and 3 show the correct labeling of the energy levels.

D. The Determination of the Transition Probabilities

A molecule may make a transition from a given energy state to a lower one and hence emit a quantum of radiation spontaneously, under the influence of another photon, or because of a disturbing collision with another particle. If we set aside the third of these for the moment the contribution to the intensity of a spectral line from a slab of molecules of thickness ds is:

$$\frac{dI_{nm}}{ds} = N_n hc\,\bar{\nu}(A_{nm} + B_{nm}I_{nm}) - N_m hc\,\bar{\nu}\,B_{mn}I_{nm} \qquad \text{(II-D-1)}$$

where the three Einstein coefficients are related by:

$$\frac{B_{mn}}{B_{nm}} = \frac{g_n}{g_m}\,, \qquad \frac{B_{nm}}{A_{nm}} = \frac{1}{8\pi hc\,\bar{\nu}^3} \qquad \text{(II-D-2)}$$

As before the frequency is given in units of inverse wavelength. Clearly only the spontaneous coefficient is needed to fully describe the emission.

This coefficient is related to the dipole moment matrix element of the transition by:

$$A^{n'v'J'}_{n''v''J''} = \frac{64\pi^4 \bar{\nu}^3}{3h} \quad \frac{\Sigma \left| R^{n'v'J'}_{n''v''J''} \right|^2}{g_{J'}} \qquad \text{(II-D-3)}$$

where the $'$ denotes the initial state and $''$ the final state, and g_J is the degeneracy of the J^{th} level. The summation here is over all sub-levels which are not distinguished from one another in the spectral line. The n refers to the collection of quantum numbers of the state excluding the vibration v and the rotation J.

In the approximation that the wavefunction of the molecular state is separable, there is no interaction between the electronic motion, the vibration, and the rotation of the molecule, and the matrix element is:

$$R^{n'v'J'}_{n''v''J''} = \left\langle a' \left| \underline{M} \right| a'' \right\rangle = \left\langle n', v', J'\Omega'M' \left| M_e \right| n'', v'', J''\Omega''M'' \right\rangle + \left\langle n' \left| n'' \right\rangle \left\langle v', J'\Omega'M' \left| M_n \right| v'', J''\Omega''M'' \right\rangle \right. \qquad \text{(II-D-4)}$$

where Dirac's notation has been used, and M_e is that part of the dipole moment operator independent of the internuclear distance while M_n is the rest. For $n' \neq n''$ the electronic eigenfunctions are orthogonal and the second term above drops out. Thus:

$$R^{n'v'J'}_{n''v''J''} = \left\langle n', v', J'\Omega'M' \left| M_e \right| n'', v'', J''\Omega''M'' \right\rangle \quad . \qquad \text{(II-D-5)}$$

Landau has shown that:

$$\sum_{M'M''} \left| R^{n'v'J'}_{n''v''J''} \right|^2 = \sum_{M'M''} \left\{ |R_x|^2 + |R_y|^2 + |R_z|^2 \right\} = 3 \sum_{M'M''} |R_z|^2 \qquad \text{(II-D-6)}$$

so that if the dipole operator in molecule fixed coordinates is expressed as $M_z = M_\eta \sin\theta + M_\zeta \cos\theta$ then:

$$R_z = \langle n'|M_\eta|n''\rangle \langle J'\Omega'M'|\sin^2\theta|J''\Omega''M''\rangle$$

$$+ \langle n'|M_\zeta|n''\rangle \langle J'\Omega'M'|\sin\theta\cos\theta|J''\Omega''M''\rangle \langle v'|r^2|v''\rangle \quad . \qquad \text{(II-D-7)}$$

This contains ω only in the form $\exp(iM\omega)$ so that the second expression in each term above will vanish unless $M' = M''$. Similarly, the expression of $R_x \pm iR_y$ will lead to the selection rule $\Delta M = \pm 1$. If the wave-function varies only slowly with the internuclear distance, averaging over r allows the Franck-Condon overlap integral to be separated:

$$R_{vib}^{v'v''} = \langle v'|r^2|v''\rangle_{av} \qquad \text{(II-D-8)}$$

and the electric dipole moment:

$$R_e^{n'n''} = \langle n'|M|n''\rangle_{av} \quad . \qquad \text{(II-D-9)}$$

The remaining integral is written as:

$$L_{J''\Omega''M''}^{J'\Omega'M'} = \langle J'\Omega'M'|\sin\theta\cos\theta|J''\Omega''M''\rangle + \langle J'\Omega'M'|\sin^2\theta|J''\Omega''M''\rangle \quad . \qquad \text{(II-D-10)}$$

The remaining selection rules along with the ones deduced above are:

$$\Delta M = 0, \pm 1 \quad , \quad \Delta\Sigma = 0$$

$$\Delta J = 0, \pm 1 \quad , \quad \Delta S = 0 \qquad \text{(II-D-11)}$$

$$\Delta\Omega = 0, \pm 1 \quad .$$

Finally combining all this gives the matrix element:

$$\sum_{M'M''} \left| R^{n'v'J'}_{n''v''J''} \right|^2 = \left| R^{n'n''}_{e} \right|^2 \left| R^{v'v''}_{vib} \right|^2 S_{J'J''} \qquad \text{(II-D-12)}$$

where $S_{J'J''}$ is the line strength and obeys the summation rules:

$$\sum_{J''} S_{J'J''} = 2J'+1 \ , \quad \sum_{J'} S_{J'J''} = 2J''+1 \ . \qquad \text{(II-D-13)}$$

The transitions allowed by the selection rules between states of the OH molecule are labeled O, P, Q, and R according to the scheme listed in Table 6. These labels do not consider the effects of symmetry or hyperfine structure. Table 7 gives the line strengths of the various transitions of interest calculated from the general formulae of Kovacs, and Table 8 gives the resulting spontaneous transition probability matrix. In Table 8 the energy levels are numbered in order of increasing energy refering to Figures 1, 2, and 3: levels 1-16 are the Π states with $V = 0$, 17-32 the $V = 1$ levels, 33-48 the $V = 2$ states and levels 49-54 are the Σ states.

The above calculations can be easily extended to include hyperfine structure if desired by writing:

$$[(2J'+1)(2F''+1)W^2(J'J''F'F'';1I)]S_{J'J''} \qquad \text{(II-D-14)}$$

in place of $S_{J'J''}$; $W^2(\ldots)$ is the square of the Racah coefficient listed in Table 5.

TABLE 5

The Racah Coefficients

	$F' = J'-1/2$	$F' = J'+1/2$
$F'' = J''+1/2$	$\frac{(F'+F''+3)(F'+F'')}{(2F'+1)(2F'+2)(2F''+1)(2F''+2)}$	$\frac{(2-F'+F'')(1+F'-F'')}{2F'(2F'+1)(2F''+1)(2F''+2)}$
$F'' = J''-1/2$	$\frac{(F'-F''+2)(F''-F'+1)}{(2F'+1)(2F'+2)(2F'')(2F''+1)}$	$\frac{(F'+F''+2)(F'+F''-1)}{2F'(2F'+1)(2F'')(2F''+1)}$

TABLE 6

The 12 transitions allowed are (Dicke and Croswhite 1962):*

Name	Transition
O_{12}	$(K-2, J-1) \rightarrow (K,J)$; $1 \rightarrow 2$
P_1	$(K-1, J-1) \rightarrow (K,J)$; $1 \rightarrow 1$
P_2	$(K-1, J-1) \rightarrow (K,J)$; $2 \rightarrow 2$
P_{12}	$(K-1, J) \rightarrow (K,J)$; $1 \rightarrow 2$
Q_1	$(K,J) \rightarrow (K,J)$; $1 \rightarrow 1$
Q_{21}	$(K, J-1) \rightarrow (K,J)$; $2 \rightarrow 1$
Q_2	$(K,J) \rightarrow (K,J)$; $2 \rightarrow 2$
Q_{12}	$(K, J+1) \rightarrow (K,J)$; $1 \rightarrow 2$
R_1	$(K+1, J+1) \rightarrow (K,J)$; $1 \rightarrow 1$
R_{21}	$(K+1, J) \rightarrow (K,J)$; $2 \rightarrow 1$
R_2	$(K+1, J+1) \rightarrow (K,J)$; $2 \rightarrow 2$
S_{21}	$(K+2, J+1) \rightarrow (K,J)$; $2 \rightarrow 1$

*Refer to Figures 1, 2, and 3.

TABLE 7

The line strengths for the $^2\Pi$-$^2\Pi$ transitions in OH (dimensionless)

K″	$P_1(K)$ $R_1(K-1)$	$P_2(K)$ $R_2(K-1)$	$Q_1(K)$	$Q_2(K)$	$R_{21}(K)$ $P_{12}(K+1)$	$Q_{21}(K)$ $Q_{12}(K+1)$	$S_{21}(K)$ $O_{12}(K+2)$
1	0.	0.	2.30	0.667	0.031	0.040	0.005
2	1.62	1.29	1.40	0.300	0.045	0.037	0.006
3	2.90	2.34	0.98	0.223	0.049	0.033	0.008
4	4.04	3.37	0.73	0.188	0.052	0.027	0.007
5	5.14	4.37	0.57	0.17	0.05	0.02	0.006
6	6.21	5.38	0.46	0.16	0.05	0.02	0.005

The line strengths for the $^2\Sigma$-$^2\Pi$ transitions in OH

K″	P_1	P_2	Q_1	Q_2	R_1	R_2
1	.587		.563	.331	.162	.169
2	.795	.275	1.063	.688	.381	.356
3	1.031	.538	1.584	1.140		.556
4	1.280	.807				
	O_{12}	P_{12}	Q_{21}	Q_{12}	R_{21}	S_{21}
1		.331	.400	.175	.244	.050
2	.081	.375	.319	.238	.319	.075
3	.106	.400	.331	.262	.338	
4	.113	.394	.306			

The line strengths for the $^2\Sigma$-$^2\Sigma$ transitions in OH

K″	R_1	R_{21}	R_2
0	2.66	2.66	2.66
1	1.60	1.60	1.60
2		1.37	

TABLE 8

THE NEW SPONTANEOUS TRANSITION MATRIX FOR CASE 300

CASE NUMBER 300 54 ROWS 54 COLUMNS STORAGE MODE 0 PAGE 1

COLUMN	1	2	3	4	5	6	7	8	9	10
ROW 1	0.0	0.0	0.0	0.0	0.0	0.0	0.0	0.0	0.0	0.0
ROW 2	8.545E-11	0.0	0.0	0.0	0.0	0.0	0.0	0.0	0.0	0.0
ROW 3	1.370E-01	0.0	0.0	0.0	0.0	0.0	0.0	0.0	0.0	0.0
ROW 4	0.0	1.378E-01	1.615E-09	0.0	0.0	0.0	0.0	0.0	0.0	0.0
ROW 5	3.468E-02	0.0	0.0	0.0	0.0	0.0	0.0	0.0	0.0	0.0
ROW 6	0.0	3.476E-02	0.0	0.0	1.159E-09	0.0	0.0	0.0	0.0	0.0
ROW 7	0.0	4.410E-02	8.944E-03	0.0	6.435E-03	0.0	0.0	0.0	0.0	0.0
ROW 8	4.433E-02	0.0	0.0	8.959E-03	0.0	6.467E-03	1.139E-09	0.0	0.0	0.0
ROW 9	0.0	0.0	5.179E-01	0.0	0.0	0.0	0.0	0.0	0.0	0.0
ROW 10	0.0	0.0	0.0	5.211E-01	0.0	0.0	0.0	0.0	9.513E-09	0.0
ROW 11	1.737E-02	0.0	0.0	5.579E-02	0.0	0.0	3.510E-02	0.0	3.123E-03	0.0
ROW 12	0.0	1.741E-02	5.618E-02	0.0	0.0	0.0	0.0	3.512E-02	0.0	3.105E-03
ROW 13	0.0	0.0	0.0	0.0	0.0	0.0	0.0	0.0	1.255E 00	0.0
ROW 14	0.0	0.0	0.0	0.0	0.0	0.0	0.0	0.0	0.0	1.259E 00
ROW 15	0.0	0.0	2.674E-02	0.0	0.0	0.0	0.0	0.0	0.0	6.178E-02
ROW 16	0.0	0.0	0.0	2.675E-02	0.0	0.0	0.0	0.0	6.233E-02	0.0
ROW 17	0.0	2.306E 03	1.569E 03	0.0	3.737E 01	0.0	0.0	2.745E 01	0.0	0.0
ROW 18	2.396E 03	0.0	0.0	1.569E 03	0.0	3.736E 01	2.746E 01	0.0	0.0	0.0
ROW 19	1.202E 03	0.0	0.0	9.777E 02	0.0	0.0	2.348E 01	0.0	1.816E 03	0.0
ROW 20	0.0	1.202E 03	9.780E 02	0.0	0.0	0.0	0.0	2.348E 01	0.0	1.816E 03
ROW 21	9.244E 01	0.0	0.0	0.0	0.0	1.394E 03	2.551E 03	0.0	0.0	0.0
ROW 22	0.0	9.244E 01	0.0	0.0	1.395E 03	0.0	0.0	2.551E 03	0.0	0.0
ROW 23	0.0	3.754E 01	4.145E 01	0.0	1.411E 03	0.0	0.0	3.117E 02	0.0	0.0
ROW 24	3.754E 01	0.0	0.0	4.145E 01	0.0	1.411E 03	3.118E 02	0.0	0.0	0.0
ROW 25	0.0	0.0	1.657E 03	0.0	0.0	0.0	0.0	0.0	0.0	5.077E 02
ROW 26	0.0	0.0	0.0	1.658E 03	0.0	0.0	0.0	0.0	5.080E 02	0.0
ROW 27	4.364E 00	0.0	0.0	3.674E 01	0.0	0.0	1.755E 03	0.0	2.453E 01	0.0
ROW 28	0.0	4.365E 00	3.675E 01	0.0	0.0	0.0	0.0	1.755E 03	0.0	2.453E 01
ROW 29	0.0	0.0	0.0	0.0	0.0	0.0	0.0	0.0	1.887E 03	0.0
ROW 30	0.0	0.0	0.0	0.0	0.0	0.0	0.0	0.0	0.0	1.887E 03
ROW 31	0.0	0.0	4.083E 00	0.0	0.0	0.0	0.0	0.0	0.0	3.043E 01
ROW 32	0.0	0.0	0.0	4.083E 00	0.0	0.0	0.0	0.0	3.045E 01	0.0
ROW 33	0.0	1.470E 03	9.996E 02	0.0	2.417E 01	0.0	0.0	1.824E 01	0.0	0.0
ROW 34	1.470E 03	0.0	0.0	9.996E 02	0.0	2.417E 01	1.824E 01	0.0	0.0	0.0
ROW 35	7.144E 02	0.0	0.0	5.957E 02	0.0	0.0	1.508E 01	0.0	1.174E 03	0.0
ROW 36	0.0	7.145E 02	5.959E 02	0.0	0.0	0.0	0.0	1.508E 01	0.0	1.174E 03
ROW 37	5.395E 01	0.0	0.0	0.0	0.0	8.521E 02	1.603E 03	0.0	0.0	0.0
ROW 38	0.0	5.395E 01	0.0	0.0	8.522E 02	0.0	0.0	1.602E 03	0.0	0.0
ROW 39	0.0	2.105E 01	2.428E 01	0.0	8.316E 02	0.0	0.0	1.882E 02	0.0	0.0
ROW 40	2.105E 01	0.0	0.0	2.428E 01	0.0	8.316E 02	1.882E 02	0.0	0.0	0.0
ROW 41	0.0	0.0	9.685E 02	0.0	0.0	0.0	0.0	0.0	0.0	3.113E 02
ROW 42	0.0	0.0	0.0	9.685E 02	0.0	0.0	0.0	0.0	3.126E 02	0.0
ROW 43	2.399E 00	0.0	0.0	2.085E 01	0.0	0.0	1.037E 03	0.0	1.454E 01	0.0
ROW 44	0.0	2.399E 00	2.085E 01	0.0	0.0	0.0	0.0	1.037E 03	0.0	1.454E 01
ROW 45	0.0	0.0	0.0	0.0	0.0	0.0	0.0	0.0	1.091E 03	0.0
ROW 46	0.0	0.0	0.0	0.0	0.0	0.0	0.0	0.0	0.0	1.092E 03
ROW 47	0.0	0.0	2.191E 00	0.0	0.0	0.0	0.0	0.0	0.0	1.704E 01
ROW 48	0.0	0.0	0.0	2.197E 00	0.0	0.0	0.0	0.0	1.709E 01	0.0
ROW 49	7.261E 06	0.0	0.0	0.0	0.0	4.383E 06	1.068E 06	0.0	0.0	0.0
ROW 50	0.0	5.295E 06	0.0	0.0	4.403E 06	0.0	3.636E 06	0.0	0.0	0.0
ROW 51	0.0	7.993E 06	5.290E 06	0.0	1.107E 07	0.0	0.0	2.482E 07	0.0	0.0
ROW 52	1.650E 06	0.0	0.0	2.140E 06	0.0	1.130E 07	4.567E 06	0.0	0.0	0.0
ROW 53	7.328E 05	0.0	0.0	5.232E 06	0.0	0.0	1.054E 06	0.0	4.561E 06	0.0
ROW 54	0.0	2.276E 05	1.438E 06	0.0	0.0	0.0	0.0	1.593E 06	0.0	1.481E 06

TABLE 8 (cont.)

CASE NUMBER 300 54 ROWS 54 COLUMNS STORAGE MODE 0 PAGE 2

COLUMN	11	12	13	14	15	16	17	18	19	20
ROW 1	0.0	0.0	0.0	0.0	0.0	0.0	0.0	0.0	0.0	0.0
ROW 2	0.0	0.0	0.0	0.0	0.0	0.0	0.0	0.0	0.0	0.0
ROW 3	0.0	0.0	0.0	0.0	0.0	0.0	0.0	0.0	0.0	0.0
ROW 4	0.0	0.0	0.0	0.0	0.0	0.0	0.0	0.0	0.0	0.0
ROW 5	0.0	0.0	0.0	0.0	0.0	0.0	0.0	0.0	0.0	0.0
ROW 6	0.0	0.0	0.0	0.0	0.0	0.0	0.0	0.0	0.0	0.0
ROW 7	0.0	0.0	0.0	0.0	0.0	0.0	0.0	0.0	0.0	0.0
ROW 8	0.0	0.0	0.0	0.0	0.0	0.0	0.0	0.0	0.0	0.0
ROW 9	0.0	0.0	0.0	0.0	0.0	0.0	0.0	0.0	0.0	0.0
ROW 10	0.0	0.0	0.0	0.0	0.0	0.0	0.0	0.0	0.0	0.0
ROW 11	0.0	0.0	0.0	0.0	0.0	0.0	0.0	0.0	0.0	0.0
ROW 12	7.213E-10	0.0	0.0	0.0	0.0	0.0	0.0	0.0	0.0	0.0
ROW 13	0.0	0.0	0.0	0.0	0.0	0.0	0.0	0.0	0.0	0.0
ROW 14	0.0	0.0	1.335E-08	0.0	0.0	0.0	0.0	0.0	0.0	0.0
ROW 15	1.007E 00	0.0	1.189E-03	0.0	0.0	0.0	0.0	0.0	0.0	0.0
ROW 16	0.0	1.006E 00	0.0	1.171E-03	2.162E-10	0.0	0.0	0.0	0.0	0.0
ROW 17	4.036E 00	0.0	0.0	0.0	0.0	0.0	0.0	0.0	0.0	0.0
ROW 18	0.0	4.035E 00	0.0	0.0	0.0	0.0	5.902E-11	0.0	0.0	0.0
ROW 19	0.0	2.610E 01	0.0	0.0	3.061E 00	0.0	1.103E-01	0.0	0.0	0.0
ROW 20	2.611E 01	0.0	0.0	0.0	0.0	3.061E 00	0.0	1.108E-01	1.052E-09	0.0
ROW 21	0.0	0.0	0.0	0.0	0.0	0.0	3.148E-02	0.0	0.0	0.0
ROW 22	0.0	0.0	0.0	0.0	0.0	0.0	0.0	3.168E-02	0.0	0.0
ROW 23	2.230E 03	0.0	0.0	0.0	0.0	0.0	0.0	3.835E-02	8.259E-03	0.0
ROW 24	0.0	2.229E 03	0.0	0.0	0.0	0.0	3.850E-02	0.0	0.0	8.244E-03
ROW 25	1.588E 01	0.0	1.834E 03	0.0	0.0	2.085E 01	0.0	0.0	4.152E-01	0.0
ROW 26	0.0	1.588E 01	0.0	1.833E 03	2.086E 01	0.0	0.0	0.0	0.0	4.172E-01
ROW 27	0.0	1.539E 02	0.0	0.0	2.064E 03	0.0	1.456E-02	0.0	0.0	4.768E-02
ROW 28	1.540E 02	0.0	0.0	0.0	0.0	2.064E 03	0.0	1.460E-02	4.800E-02	0.0
ROW 29	0.0	0.0	0.0	3.005E 02	1.043E 01	0.0	0.0	0.0	0.0	0.0
ROW 30	0.0	0.0	3.009E 02	0.0	0.0	1.043E 01	0.0	0.0	0.0	0.0
ROW 31	2.084E 03	0.0	1.481E 01	0.0	0.0	9.693E 01	0.0	0.0	2.218E-02	0.0
ROW 32	0.0	1.952E 03	0.0	1.481E 01	9.697E 01	0.0	0.0	0.0	0.0	2.217E-02
ROW 33	2.811E 00	0.0	0.0	0.0	0.0	0.0	0.0	4.808E 03	3.156E 03	0.0
ROW 34	0.0	2.811E 00	0.0	0.0	0.0	0.0	4.809E 03	0.0	0.0	3.156E 03
ROW 35	0.0	1.751E 01	0.0	0.0	2.191E 00	0.0	2.420E 03	0.0	0.0	1.949E 03
ROW 36	1.752E 01	0.0	0.0	0.0	0.0	2.191E 00	0.0	2.420E 03	1.950E 03	0.0
ROW 37	0.0	0.0	0.0	0.0	0.0	0.0	1.869E 02	0.0	0.0	0.0
ROW 38	0.0	0.0	0.0	0.0	0.0	0.0	0.0	1.869E 02	0.0	0.0
ROW 39	1.345E 03	0.0	0.0	0.0	0.0	0.0	0.0	7.366E 01	8.548E 01	0.0
ROW 40	0.0	1.344E 03	0.0	0.0	0.0	0.0	7.367E 01	0.0	0.0	8.548E 01
ROW 41	1.009E 01	0.0	1.200E 03	0.0	0.0	1.409E 01	0.0	0.0	3.336E 03	0.0
ROW 42	0.0	1.009E 01	0.0	1.200E 03	1.409E 01	0.0	0.0	0.0	0.0	3.337E 03
ROW 43	0.0	9.467E 00	0.0	0.0	1.348E 03	0.0	8.828E 00	0.0	0.0	7.420E 01
ROW 44	9.469E 00	0.0	0.0	0.0	0.0	1.348E 03	0.0	8.829E 00	7.423E 01	0.0
ROW 45	0.0	0.0	0.0	1.844E 02	6.618E 00	0.0	0.0	0.0	0.0	0.0
ROW 46	0.0	0.0	1.845E 02	0.0	0.0	6.619E 00	0.0	0.0	0.0	0.0
ROW 47	1.130E 03	0.0	8.807E 00	0.0	0.0	5.936E 01	0.0	0.0	8.237E 00	0.0
ROW 48	0.0	1.133E 03	0.0	8.828E 00	5.953E 01	0.0	0.0	0.0	0.0	8.277E 00
ROW 49	0.0	0.0	0.0	0.0	0.0	0.0	5.369E 05	0.0	0.0	0.0
ROW 50	0.0	0.0	0.0	0.0	0.0	0.0	0.0	3.620E 05	0.0	0.0
ROW 51	6.954E 06	0.0	0.0	0.0	0.0	0.0	0.0	5.457E 05	3.613E 05	0.0
ROW 52	0.0	3.541E 06	0.0	0.0	0.0	0.0	1.129E 05	0.0	0.0	1.461E 05
ROW 53	0.0	1.728E 06	0.0	0.0	4.875E 05	0.0	5.010E 05	0.0	0.0	3.246E 05
ROW 54	5.533E 05	0.0	0.0	0.0	0.0	3.528E 06	0.0	1.555E 05	9.839E 04	0.0

TABLE 8 (cont.)

CASE NUMBER 370 54 ROWS 54 COLUMNS STORAGE MODE 0 PAGE 3

COLUMN	21	22	23	24	25	26	27	28	29	30
ROW 1	0.0	0.0	0.0	0.0	0.0	0.0	0.0	0.0	0.0	0.0
ROW 2	0.0	0.0	0.0	0.0	0.0	0.0	0.0	0.0	0.0	0.0
ROW 3	0.0	0.0	0.0	0.0	0.0	0.0	0.0	0.0	0.0	0.0
ROW 4	0.0	0.0	0.0	0.0	0.0	0.0	0.0	0.0	0.0	0.0
ROW 5	0.0	0.0	0.0	0.0	0.0	0.0	0.0	0.0	0.0	0.0
ROW 6	0.0	0.0	0.0	0.0	0.0	0.0	0.0	0.0	0.0	0.0
ROW 7	0.0	0.0	0.0	0.0	0.0	0.0	0.0	0.0	0.0	0.0
ROW 8	0.0	0.0	0.0	0.0	0.0	0.0	0.0	0.0	0.0	0.0
ROW 9	0.0	0.0	0.0	0.0	0.0	0.0	0.0	0.0	0.0	0.0
ROW 10	0.0	0.0	0.0	0.0	0.0	0.0	0.0	0.0	0.0	0.0
ROW 11	0.0	0.0	0.0	0.0	0.0	0.0	0.0	0.0	0.0	0.0
ROW 12	0.0	0.0	0.0	0.0	0.0	0.0	0.0	0.0	0.0	0.0
ROW 13	0.0	0.0	0.0	0.0	0.0	0.0	0.0	0.0	0.0	0.0
ROW 14	0.0	0.0	0.0	0.0	0.0	0.0	0.0	0.0	0.0	0.0
ROW 15	0.0	0.0	0.0	0.0	0.0	0.0	0.0	0.0	0.0	0.0
ROW 16	0.0	0.0	0.0	0.0	0.0	0.0	0.0	0.0	0.0	0.0
ROW 17	0.0	0.0	0.0	0.0	0.0	0.0	0.0	0.0	0.0	0.0
ROW 18	0.0	0.0	0.0	0.0	0.0	0.0	0.0	0.0	0.0	0.0
ROW 19	0.0	0.0	0.0	0.0	0.0	0.0	0.0	0.0	0.0	0.0
ROW 20	0.0	0.0	0.0	0.0	0.0	0.0	0.0	0.0	0.0	0.0
ROW 21	0.0	0.0	0.0	0.0	0.0	0.0	0.0	0.0	0.0	0.0
ROW 22	5.382E-09	0.0	0.0	0.0	0.0	0.0	0.0	0.0	0.0	0.0
ROW 23	5.106E-03	0.0	0.0	0.0	0.0	0.0	0.0	0.0	0.0	0.0
ROW 24	0.0	5.077E-03	4.636E-10	0.0	0.0	0.0	0.0	0.0	0.0	0.0
ROW 25	0.0	0.0	0.0	0.0	0.0	0.0	0.0	0.0	0.0	0.0
ROW 26	0.0	0.0	0.0	0.0	4.793E-09	0.0	0.0	0.0	0.0	0.0
ROW 27	0.0	0.0	2.766E-02	0.0	2.905E-03	0.0	0.0	0.0	0.0	0.0
ROW 28	0.0	0.0	0.0	2.773E-02	0.0	2.896E-03	6.304E-10	0.0	0.0	0.0
ROW 29	0.0	0.0	0.0	0.0	1.004E 00	0.0	0.0	0.0	0.0	0.0
ROW 30	0.0	0.0	0.0	0.0	0.0	1.011E 00	0.0	0.0	2.023E-08	0.0
ROW 31	0.0	0.0	0.0	0.0	0.0	5.214E-02	7.994F-01	0.0	1.121F-03	0.0
ROW 32	0.0	0.0	0.0	0.0	5.251E-02	0.0	0.0	7.970F-01	0.0	1.096F-03
ROW 33	7.476E 01	0.0	0.0	5.490E 01	0.0	0.0	8.069F 00	0.0	0.0	0.0
ROW 34	0.0	7.474E 01	5.492E 01	0.0	0.0	0.0	0.0	8.058F 01	0.0	0.0
ROW 35	0.0	0.0	4.693E 01	0.0	3.646F 03	0.0	0.0	5.213E 01	0.0	0.0
ROW 36	0.0	0.0	0.0	4.694E 01	0.0	3.646F 03	5.216E 01	0.0	0.0	0.0
ROW 37	0.0	2.791E 03	4.904E 03	0.0	0.0	0.0	0.0	0.0	0.0	0.0
ROW 38	2.791E 03	0.0	0.0	5.122E 03	0.0	0.0	0.0	0.0	0.0	0.0
ROW 39	2.746E 03	0.0	0.0	6.051E 02	0.0	0.0	4.379E 03	0.0	0.0	0.0
ROW 40	0.0	2.745E 03	6.054E 02	0.0	0.0	0.0	0.0	4.328E 03	0.0	0.0
ROW 41	0.0	0.0	0.0	0.0	0.0	1.022E 03	3.177F 01	0.0	3.682E 03	0.0
ROW 42	0.0	0.0	0.0	0.0	1.022E 03	0.0	0.0	3.178E 01	0.0	3.680E 03
ROW 43	0.0	0.0	3.532E 03	0.0	4.943F 01	0.0	0.0	3.096F 02	0.0	0.0
ROW 44	0.0	0.0	0.0	3.532F 03	0.0	4.942E 01	3.097E 02	0.0	0.0	0.0
ROW 45	0.0	0.0	0.0	0.0	3.803F 03	0.0	0.0	0.0	0.0	6.049E 02
ROW 46	0.0	0.0	0.0	0.0	0.0	3.804E 03	0.0	0.0	6.048F 02	0.0
ROW 47	0.0	0.0	0.0	0.0	0.0	6.121E 01	3.914F 03	0.0	2.977E 01	0.0
ROW 48	0.0	0.0	0.0	0.0	6.155E 01	0.0	0.0	3.933E 03	0.0	2.991E 01
ROW 49	0.0	2.989E 0?	7.285E 04	0.0	0.0	0.0	0.0	0.0	0.0	0.0
ROW 50	3.009F 05	0.0	2.478E 05	0.0	0.0	0.0	0.0	0.0	0.0	0.0
ROW 51	7.562E 04	0.0	0.0	1.689E 05	0.0	0.0	4.741E 04	0.0	0.0	0.0
ROW 52	0.0	7.719E 04	3.211E 05	0.0	0.0	0.0	0.0	2.415E 05	0.0	0.0
ROW 53	0.0	0.0	7.181E 04	0.0	3.111E 05	0.0	0.0	1.176E 05	0.0	0.0
ROW 54	0.0	0.0	1.099E 05	0.0	0.0	1.014E 05	3.775E 05	0.0	0.0	0.0

TABLE 8 (cont.)

CASE NUMBER 300 54 ROWS 54 COLUMNS STORAGE MODE 0 PAGE 4

COLUMN	31	32	33	34	35	36	37	38	39	40
ROW 1	0.0	0.0	0.0	0.0	0.0	0.0	0.0	0.0	0.0	0.0
ROW 2	0.0	0.0	0.0	0.0	0.0	0.0	0.0	0.0	0.0	0.0
ROW 3	0.0	0.0	0.0	0.0	0.0	0.0	0.0	0.0	0.0	0.0
ROW 4	0.0	0.0	0.0	0.0	0.0	0.0	0.0	0.0	0.0	0.0
ROW 5	0.0	0.0	0.0	0.0	0.0	0.0	0.0	0.0	0.0	0.0
ROW 6	0.0	0.0	0.0	0.0	0.0	0.0	0.0	0.0	0.0	0.0
ROW 7	0.0	0.0	0.0	0.0	0.0	0.0	0.0	0.0	0.0	0.0
ROW 8	0.0	0.0	0.0	0.0	0.0	0.0	0.0	0.0	0.0	0.0
ROW 9	0.0	0.0	0.0	0.0	0.0	0.0	0.0	0.0	0.0	0.0
ROW 10	0.0	0.0	0.0	0.0	0.0	0.0	0.0	0.0	0.0	0.0
ROW 11	0.0	0.0	0.0	0.0	0.0	0.0	0.0	0.0	0.0	0.0
ROW 12	0.0	0.0	0.0	0.0	0.0	0.0	0.0	0.0	0.0	0.0
ROW 13	0.0	0.0	0.0	0.0	0.0	0.0	0.0	0.0	0.0	0.0
ROW 14	0.0	0.0	0.0	0.0	0.0	0.0	0.0	0.0	0.0	0.0
ROW 15	0.0	0.0	0.0	0.0	0.0	0.0	0.0	0.0	0.0	0.0
ROW 16	0.0	0.0	0.0	0.0	0.0	0.0	0.0	0.0	0.0	0.0
ROW 17	0.0	0.0	0.0	0.0	0.0	0.0	0.0	0.0	0.0	0.0
ROW 18	0.0	0.0	0.0	0.0	0.0	0.0	0.0	0.0	0.0	0.0
ROW 19	0.0	0.0	0.0	0.0	0.0	0.0	0.0	0.0	0.0	0.0
ROW 20	0.0	0.0	0.0	0.0	0.0	0.0	0.0	0.0	0.0	0.0
ROW 21	0.0	0.0	0.0	0.0	0.0	0.0	0.0	0.0	0.0	0.0
ROW 22	0.0	0.0	0.0	0.0	0.0	0.0	0.0	0.0	0.0	0.0
ROW 23	0.0	0.0	0.0	0.0	0.0	0.0	0.0	0.0	0.0	0.0
ROW 24	0.0	0.0	0.0	0.0	0.0	0.0	0.0	0.0	0.0	0.0
ROW 25	0.0	0.0	0.0	0.0	0.0	0.0	0.0	0.0	0.0	0.0
ROW 26	0.0	0.0	0.0	0.0	0.0	0.0	0.0	0.0	0.0	0.0
ROW 27	0.0	0.0	0.0	0.0	0.0	0.0	0.0	0.0	0.0	0.0
ROW 28	0.0	0.0	0.0	0.0	0.0	0.0	0.0	0.0	0.0	0.0
ROW 29	0.0	0.0	0.0	0.0	0.0	0.0	0.0	0.0	0.0	0.0
ROW 30	0.0	0.0	0.0	0.0	0.0	0.0	0.0	0.0	0.0	0.0
ROW 31	0.0	0.0	0.0	0.0	0.0	0.0	0.0	0.0	0.0	0.0
ROW 32	6.123E-11	0.0	0.0	0.0	0.0	0.0	0.0	0.0	0.0	0.0
ROW 33	0.0	0.0	0.0	0.0	0.0	0.0	0.0	0.0	0.0	0.0
ROW 34	0.0	0.0	1.522E-09	0.0	0.0	0.0	0.0	0.0	0.0	0.0
ROW 35	6.110E 00	0.0	8.232E-02	0.0	0.0	0.0	0.0	0.0	0.0	0.0
ROW 36	0.0	6.110E 00	0.0	8.279E-02	4.425E-09	0.0	0.0	0.0	0.0	0.0
ROW 37	0.0	0.0	2.597E-02	0.0	0.0	0.0	0.0	0.0	0.0	0.0
ROW 38	0.0	0.0	0.0	2.592E-02	0.0	0.0	1.026E-10	0.0	0.0	0.0
ROW 39	0.0	0.0	0.0	1.492E-02	1.747E-03	0.0	1.193E-04	0.0	0.0	0.0
ROW 40	0.0	0.0	1.502E-02	0.0	0.0	1.734E-03	0.0	1.206E-04	1.346E-10	0.0
ROW 41	0.0	4.162E 01	0.0	0.0	3.095E-01	0.0	0.0	0.0	0.0	0.0
ROW 42	4.164E 01	0.0	0.0	0.0	0.0	3.103E-01	0.0	0.0	0.0	0.0
ROW 43	4.110E 03	0.0	1.143E-02	0.0	0.0	3.836E-02	0.0	0.0	5.893E-02	0.0
ROW 44	0.0	4.111E 03	0.0	1.143E-02	3.835E-02	0.0	0.0	0.0	0.0	5.899E-02
ROW 45	2.090E 01	0.0	0.0	0.0	0.0	0.0	0.0	0.0	0.0	0.0
ROW 46	0.0	2.091E 01	0.0	0.0	0.0	0.0	0.0	0.0	0.0	0.0
ROW 47	0.0	1.941E 02	0.0	0.0	1.623E-02	0.0	0.0	0.0	0.0	0.0
ROW 48	1.952E 02	0.0	0.0	0.0	0.0	1.713E-02	0.0	0.0	0.0	0.0
ROW 49	0.0	0.0	1.682E 04	0.0	0.0	0.0	0.0	9.314E 04	0.0	0.0
ROW 50	0.0	0.0	0.0	1.130E 04	0.0	0.0	9.379E 03	0.0	0.0	0.0
ROW 51	0.0	0.0	0.0	1.703E 04	1.127E 04	0.0	2.356E 03	0.0	0.0	0.0
ROW 52	0.0	0.0	3.526E 03	0.0	0.0	4.568E 03	0.0	2.406E 03	0.0	0.0
ROW 53	3.321E 04	0.0	1.571E 03	0.0	0.0	1.014E 04	0.0	0.0	2.251E 03	0.0
ROW 54	0.0	2.404E 05	0.0	4.873E 03	3.077E 03	0.0	0.0	0.0	0.0	3.414E 03

TABLE 8 (cont.)

CASE NUMBER 300 54 ROWS 54 COLUMNS STORAGE MODE 0 PAGE 5

COLUMN	41	42	43	44	45	46	47	48	49	50
ROW 1	0.0	0.0	0.0	0.0	0.0	0.0	0.0	0.0	0.0	0.0
ROW 2	0.0	0.0	0.0	0.0	0.0	0.0	0.0	0.0	0.0	0.0
ROW 3	0.0	0.0	0.0	0.0	0.0	0.0	0.0	0.0	0.0	0.0
ROW 4	0.0	0.0	0.0	0.0	0.0	0.0	0.0	0.0	0.0	0.0
ROW 5	0.0	0.0	0.0	0.0	0.0	0.0	0.0	0.0	0.0	0.0
ROW 6	0.0	0.0	0.0	0.0	0.0	0.0	0.0	0.0	0.0	0.0
ROW 7	0.0	0.0	0.0	0.0	0.0	0.0	0.0	0.0	0.0	0.0
ROW 8	0.0	0.0	0.0	0.0	0.0	0.0	0.0	0.0	0.0	0.0
ROW 9	0.0	0.0	0.0	0.0	0.0	0.0	0.0	0.0	0.0	0.0
ROW 10	0.0	0.0	0.0	0.0	0.0	0.0	0.0	0.0	0.0	0.0
ROW 11	0.0	0.0	0.0	0.0	0.0	0.0	0.0	0.0	0.0	0.0
ROW 12	0.0	0.0	0.0	0.0	0.0	0.0	0.0	0.0	0.0	0.0
ROW 13	0.0	0.0	0.0	0.0	0.0	0.0	0.0	0.0	0.0	0.0
ROW 14	0.0	0.0	0.0	0.0	0.0	0.0	0.0	0.0	0.0	0.0
ROW 15	0.0	0.0	0.0	0.0	0.0	0.0	0.0	0.0	0.0	0.0
ROW 16	0.0	0.0	0.0	0.0	0.0	0.0	0.0	0.0	0.0	0.0
ROW 17	0.0	0.0	0.0	0.0	0.0	0.0	0.0	0.0	0.0	0.0
ROW 18	0.0	0.0	0.0	0.0	0.0	0.0	0.0	0.0	0.0	0.0
ROW 19	0.0	0.0	0.0	0.0	0.0	0.0	0.0	0.0	0.0	0.0
ROW 20	0.0	0.0	0.0	0.0	0.0	0.0	0.0	0.0	0.0	0.0
ROW 21	0.0	0.0	0.0	0.0	0.0	0.0	0.0	0.0	0.0	0.0
ROW 22	0.0	0.0	0.0	0.0	0.0	0.0	0.0	0.0	0.0	0.0
ROW 23	0.0	0.0	0.0	0.0	0.0	0.0	0.0	0.0	0.0	0.0
ROW 24	0.0	0.0	0.0	0.0	0.0	0.0	0.0	0.0	0.0	0.0
ROW 25	0.0	0.0	0.0	0.0	0.0	0.0	0.0	0.0	0.0	0.0
ROW 26	0.0	0.0	0.0	0.0	0.0	0.0	0.0	0.0	0.0	0.0
ROW 27	0.0	0.0	0.0	0.0	0.0	0.0	0.0	0.0	0.0	0.0
ROW 28	0.0	0.0	0.0	0.0	0.0	0.0	0.0	0.0	0.0	0.0
ROW 29	0.0	0.0	0.0	0.0	0.0	0.0	0.0	0.0	0.0	0.0
ROW 30	0.0	0.0	0.0	0.0	0.0	0.0	0.0	0.0	0.0	0.0
ROW 31	0.0	0.0	0.0	0.0	0.0	0.0	0.0	0.0	0.0	0.0
ROW 32	0.0	0.0	0.0	0.0	0.0	0.0	0.0	0.0	0.0	0.0
ROW 33	0.0	0.0	0.0	0.0	0.0	0.0	0.0	0.0	0.0	0.0
ROW 34	0.0	0.0	0.0	0.0	0.0	0.0	0.0	0.0	0.0	0.0
ROW 35	0.0	0.0	0.0	0.0	0.0	0.0	0.0	0.0	0.0	0.0
ROW 36	0.0	0.0	0.0	0.0	0.0	0.0	0.0	0.0	0.0	0.0
ROW 37	0.0	0.0	0.0	0.0	0.0	0.0	0.0	0.0	0.0	0.0
ROW 38	0.0	0.0	0.0	0.0	0.0	0.0	0.0	0.0	0.0	0.0
ROW 39	0.0	0.0	0.0	0.0	0.0	0.0	0.0	0.0	0.0	0.0
ROW 40	0.0	0.0	0.0	0.0	0.0	0.0	0.0	0.0	0.0	0.0
ROW 41	0.0	0.0	0.0	0.0	0.0	0.0	0.0	0.0	0.0	0.0
ROW 42	4.597E-02	0.0	0.0	0.0	0.0	0.0	0.0	0.0	0.0	0.0
ROW 43	2.537E-03	0.0	0.0	0.0	0.0	0.0	0.0	0.0	0.0	0.0
ROW 44	0.0	2.518E-03	1.394E-10	0.0	0.0	0.0	0.0	0.0	0.0	0.0
ROW 45	7.453E-01	0.0	0.0	0.0	0.0	0.0	0.0	0.0	0.0	0.0
ROW 46	0.0	7.507E-01	0.0	0.0	1.896E-05	0.0	0.0	0.0	0.0	0.0
ROW 47	0.0	3.772E-02	5.089E-01	0.0	7.737E-04	0.0	0.0	0.0	0.0	0.0
ROW 48	4.133E-02	0.0	0.0	5.866E-01	0.0	9.653E-04	3.544E-06	0.0	0.0	0.0
ROW 49	2.267E 03	0.0	0.0	0.0	0.0	0.0	0.0	0.0	0.0	0.0
ROW 50	0.0	7.726E 03	0.0	0.0	0.0	0.0	0.0	0.0	2.198E-02	0.0
ROW 51	0.0	5.259E 03	0.0	0.0	1.464E 03	0.0	0.0	0.0	1.131E-02	0.0
ROW 52	9.697E 03	0.0	0.0	0.0	0.0	7.617E 03	0.0	0.0	0.0	8.910E-02
ROW 53	9.698E 03	0.0	0.0	0.0	0.0	3.647E 03	1.034E 03	0.0	0.0	0.0
ROW 54	0.0	3.164E 03	1.176E 04	0.0	0.0	0.0	0.0	7.486E 03	0.0	0.0

TABLE 8 (cont.)

CASE NUMBER 300 54 ROWS 54 COLUMNS

COLUMN	51	52	53	54
ROW 1	0.0	0.0	0.0	0.0
ROW 2	0.0	0.0	0.0	0.0
ROW 3	0.0	0.0	0.0	0.0
ROW 4	0.0	0.0	0.0	0.0
ROW 5	0.0	0.0	0.0	0.0
ROW 6	0.0	0.0	0.0	0.0
ROW 7	0.0	0.0	0.0	0.0
ROW 8	0.0	0.0	0.0	0.0
ROW 9	0.0	0.0	0.0	0.0
ROW 10	0.0	0.0	0.0	0.0
ROW 11	0.0	0.0	0.0	0.0
ROW 12	0.0	0.0	0.0	0.0
ROW 13	0.0	0.0	0.0	0.0
ROW 14	0.0	0.0	0.0	0.0
ROW 15	0.0	0.0	0.0	0.0
ROW 16	0.0	0.0	0.0	0.0
ROW 17	0.0	0.0	0.0	0.0
ROW 18	0.0	0.0	0.0	0.0
ROW 19	0.0	0.0	0.0	0.0
ROW 20	0.0	0.0	0.0	0.0
ROW 21	0.0	0.0	0.0	0.0
ROW 22	0.0	0.0	0.0	0.0
ROW 23	0.0	0.0	0.0	0.0
ROW 24	0.0	0.0	0.0	0.0
ROW 25	0.0	0.0	0.0	0.0
ROW 26	0.0	0.0	0.0	0.0
ROW 27	0.0	0.0	0.0	0.0
ROW 28	0.0	0.0	0.0	0.0
ROW 29	0.0	0.0	0.0	0.0
ROW 30	0.0	0.0	0.0	0.0
ROW 31	0.0	0.0	0.0	0.0
ROW 32	0.0	0.0	0.0	0.0
ROW 33	0.0	0.0	0.0	0.0
ROW 34	0.0	0.0	0.0	0.0
ROW 35	0.0	0.0	0.0	0.0
ROW 36	0.0	0.0	0.0	0.0
ROW 37	0.0	0.0	0.0	0.0
ROW 38	0.0	0.0	0.0	0.0
ROW 39	0.0	0.0	0.0	0.0
ROW 40	0.0	0.0	0.0	0.0
ROW 41	0.0	0.0	0.0	0.0
ROW 42	0.0	0.0	0.0	0.0
ROW 43	0.0	0.0	0.0	0.0
ROW 44	0.0	0.0	0.0	0.0
ROW 45	0.0	0.0	0.0	0.0
ROW 46	0.0	0.0	0.0	0.0
ROW 47	0.0	0.0	0.0	0.0
ROW 48	0.0	0.0	0.0	0.0
ROW 49	0.0	0.0	0.0	0.0
ROW 50	0.0	0.0	0.0	0.0
ROW 51	0.0	0.0	0.0	0.0
ROW 52	1.601E-01	0.0	0.0	0.0
ROW 53	1.094E-01	0.0	0.0	0.0
ROW 54	0.0	3.612E-01	5.077E-01	0.0

E. The Population and Transfer Equations

The energy state of an OH molecule can change by one of four possible mechanisms. First the molecule may spontaneously emit a photon and change to a state lower by the energy of the photon. Second it may encounter a photon and be induced to emit or absorb a photon of the same energy and change to a different state. Third it may encounter a particle of finite mass and be induced to change its energy state without emitting or absorbing a photon. Finally, it may change states under the influence of a particle and emit a photon. The rate of change of the population of the i^{th} level then is:

$$\frac{dN_i}{dt} = \sum_j W_{ji} N_j - N_i \sum_j W_{ij} \qquad \text{(II-E-1)}$$

where

$$W_{lk} \equiv (A_{lk} + B_{lk} I_{\nu_{lk}} + C_{lk} + D_{lk}) \phi_{\nu_{lk}} \text{ and } W_{ii} \equiv 0 \qquad \text{(II-E-2)}$$

and A_{lk}, B_{lk}, C_{lk}, and D_{lk} are the rate coefficients for the four mechanisms above in order. $\phi_{\nu_{lk}}$ is the line shape factor, which will be discussed later. For our purposes the A and D factors may be combined as $A'_{lk} = A_{lk} + D_{lk}$. Degeneracy may also be included by writing:

$$B^*_{ij} = g_i B_{ij} = g_j B_{ji} \,, \quad A^*_{ij} = g_i A'_{ij} \,, \quad N^*_i = \frac{N_i}{g_i} \,. \qquad \text{(II-E-3)}$$

This results in an equation similar to (II-E-1) with the N's and W's replaced by the corresponding N^*'s and W^*'s, and the left hand side multiplied by the degeneracy factor g_i.

Since only two specific levels of a complicated energy structure are of interest in a line transition, the rate equations can be written

specifically separating those two levels; the subscript u for the upper and ℓ for the lower of them the two rate equations are:

$$\frac{dN_u}{dt} = N_\ell B_{\ell u} I_\nu \phi_a - N_u B_{u\ell} I_\nu \phi_e - N_u A_{u\ell} \phi_e + R_u (N - N_{\ell u}) \phi_R - \Gamma_u N_u \phi_\Gamma ,$$

$$\frac{dN_\ell}{dt} = -N_\ell B_{\ell u} I_\nu \phi_a + N_u B_{u\ell} I_\nu \phi_e + N_u A_{u\ell} \phi_e + R_\ell (N - N_{\ell u}) \phi_R - \Gamma_\ell N_\ell \phi_\Gamma , \qquad \text{(II-E-4)}$$

where

$$R_\ell = \sum_j W_{j\ell} \left(\frac{N_j}{N - N_{\ell u}} \right) - W_{u\ell} \left(\frac{N_u}{N - N_{\ell u}} \right) ,$$

$$R_u = \sum_j W_{ju} \left(\frac{N_j}{N - N_{\ell u}} \right) - W_{\ell u} \left(\frac{N_\ell}{N - N_{\ell u}} \right) ,$$

$$\Gamma_u = \sum_j W_{uj} - W_{u\ell} ,$$

$$\Gamma_\ell = \sum_j W_{\ell j} - W_{\ell u} , \qquad \text{(II-E-5)}$$

$$N_{\ell u} = N_\ell + N_u ,$$

$$N = \sum_j N_j .$$

The subscript of ϕ distinguishes the evaluation of $\phi_{\nu_{ij}}$ for emission e, or absorption a, or one of the relaxation processes R or Γ.

Integrating the rate equations (II-E-4) over frequency, averaging over direction, and applying the transformation (II-E-3) the two rate equations of interest become:

$$g_u \frac{dN_u^*}{dt} = (N_\ell^* - N_u^*)B^*J - N_u^*A^* + R_u^*(N^* - N_{u\ell}^*) - \Gamma_u^* N_u^* ,$$

$$g_e \frac{dN_e^*}{dt} = -(N_\ell^* - N_u^*)B^*J - N_u^*A^* + R_\ell^*(N^* - N_{u\ell}^*) - \Gamma_\ell^* N_\ell^* , \qquad \text{(II-E-6)}$$

where I, J, and ϕ are related by:

$$\int_0^\infty \phi_\nu d\nu = 1 , \quad \int_0^\infty \phi_\nu I_\nu d\nu = I , \quad \int_0^\infty I_\nu d\nu = I\Delta\nu , \quad \frac{1}{4\pi}\int_{4\pi} I d\Omega = J . \qquad \text{(II-E-7)}$$

The above equations cannot be used to determine the actual populations of the levels considered because the relaxation term R_i depends upon the populations of the other levels of the molecules energy structure. A more workable approach to be used here is to solve the simultaneous equations (II-E-1) along with a normality condition such as $\sum_j N_j = 1$ for the populations and hence determine the values of the R's by:

$$R_u = \frac{N_u C_u - N_\ell R_{\ell u}}{N - N_{\ell u}} , \qquad \text{(II-E-8)}$$

$$R_\ell = \frac{N_\ell C_\ell - N_u R_{u\ell}}{N - N_{\ell u}} ,$$

with

$$C_k = \sum_m W_{km} , \quad k = u, \ell$$

which can then be used in the transfer equation solution.

The equation of transfer for the radiation from the two states has the form:

$$\frac{dI\nu}{dz} = \frac{h\nu_{ij}}{4\pi}\left[(N_u B_{u\ell} I_\nu + N_u A_{u\ell})\phi_\ell - N_\ell B_{\ell u} I_\nu \phi_a\right] . \qquad \text{(II-E-9)}$$

In the following we will assume that ϕ has the same form for emission and absorption. Differences between the two functions have not been mentioned in the literature, but could arise from the line narrowing characteristic of unsaturated maser amplification or other processes. By integrating over frequency and combining with the steady state solution of the population equations (II-E-6), the transfer equation may be written in dimensionless form, after Goldreich and Keeley (1972):

$$\frac{d\mathcal{J}}{ds} = \frac{\beta(\mathcal{J} + 1/2)}{\beta+\mathcal{J}} + S \qquad \text{(II-E-10)}$$

where

$$\mathcal{J} = \frac{BI}{A^*} , \quad \mathcal{J} = \frac{BJ}{A^*} , \quad R = R_u^* + R_\ell^* , \quad \Gamma_a = \frac{\Gamma_\ell R_u + \Gamma_u R_\ell}{R_u + R_\ell} ,$$

$$\alpha = \frac{RA^*}{\Gamma_\ell R_u - \Gamma_u R_\ell} , \quad \beta = \frac{1}{2}\left(1 + \frac{\Gamma_a}{A^*}\right), \quad S = \frac{\alpha\beta}{1-\alpha} , \qquad \text{(II-E-11)}$$

$$ds = \frac{dz}{L} , \quad L = \frac{4\pi\Delta\nu}{B^* h\nu} \frac{1}{\Delta N_o} , \quad \Delta N_o = \frac{N_u^* + N_\ell^*}{2S} .$$

In the above relations, $\mathcal{I}$ and $\mathcal{J}$ are just the dimensionless intensity and average intensity, R the total rate of input to the two levels, Γ_a the average relaxation rate, and α and β are the pumping and decay rates of the pair of levels. L is the unsaturated growth length and ΔN_o is the unsaturated population difference. S is a term including the spontaneous emission, and is related to the excitation temperature of the levels in the following way. Anticipating a population inversion, the excitation temperature may be written as:

$$\frac{N_u}{N_\ell} \equiv \exp\left(\frac{h\nu_{u\ell}}{kT_{ex}}\right) . \qquad \text{(II-E-12)}$$

For $\frac{h\nu}{kT} \ll 1$ and $\frac{\Delta N_o}{N_1} \ll 1$ the population difference gives:

$$\frac{\Delta N_o}{N_\ell + N_u} = \frac{1}{2S} \quad \text{and} \quad S \simeq \frac{kT_{ex}}{h\nu_{u\ell}} \gg 1 . \qquad \text{(II-E-13)}$$

The equation of transfer (II-E-10) can be solved exactly only in one dimensional geometries. Analytical solutions for higher dimensioned situations can be found only for unsaturated conditions, where $\mathcal{J} \ll \beta$. The following chapter will discuss the solution of (II-E-10) for spherical geometries.

CHAPTER III

THE SOLUTION TO THE TRANSFER EQUATION

To analyze the population inversion in the states of any molecule, the rate equations expressing the total rates of entry to and exit from each energy level must be solved. These equations must include both collisional and radiative processes and depend upon the properties of the emission region. Since the radiation intensities will change through the region, so will the populations of the energy levels. A study of population ratios of close pairs of levels must consider simultaneously the solution of the equations of statistical equilibrium and of radiative transfer even for the simple case of time independent emission. For the case of the OH molecule there are over one hundred energy levels relevant to the study of the maser emission; this presents a formidable computational problem to solve the emission equations by this brute force method.

A more usable approach is to consider only the needed pairs of levels for the spectral lines of interest. Separate analyses for different lines can then be combined in various ways to provide a qualitative understanding of the interactions of the multiple rate and transfer equations. Quantitative calculations of the stimulated emission are of doubtful value with this approach because of the complexities of the interactions. Chapter V describes the efforts of other authors in solving the transfer equations along these lines. Our approach will be to solve the complete rate equations coupled with the transfer equation for one maser line.

If stimulated emission is not very important in the other energy

levels, and if the induced transitions in the pair of levels considered does not affect the populations of the other levels, this simplification can be completely satisfactory. Our solution will be useful if the transition considered is the dominant transfer path out of an energy level, and can be applied quantitatively to more complex situations by iterating the rate equations with the changing intensities. The effects of the interactions are explored in Chapters IV and V. In this chapter we will explore the coupled solution of the rate and transfer equations for the two levels of an inverted population ratio using equations II-E-8,-10, and -11 for a simple model gas cloud. The treatment of Goldreich and Keeley (1972) will be extended to generalized degenerate energy levels and to all degrees of saturation, correcting some significant omissions in their derivations, and removing some simplifications. Their results for partially saturated masers omit several terms and use an incorrect approximation of the transfer solution for small core sizes, which leads them to the false conclusion of a constant minimum core size. They also ignore the effects of the background radiation, which we will show to be important for microwave masers in determining the saturation state. The same omissions mislead them to find a core of constant intensity in fully saturated masers. Further, their expressions over simplify the effects of the population inversion ratio on the maser characteristics. In the following sections we will derive the relations among the maser characteristics avoiding the errors and simplifications, and in Chapter IV show that the solutions presented give an understandable and interpretable picture of the nature of the maser process.

A. Introduction

One of the simplest models for a cosmic maser is a homogeneous spherical cloud of molecules in which inverted population is created at a uniform rate. Even in such a simple model it is not necessary that the size of the cloud be the observed size of the masing region. Rather, for moderate degrees of saturation, the observed source could be substantially smaller than the actual size of the region. Additionally, even if the inversion is created uniformly, it will not be uniform in the cloud. If 10° K isotropic external radiation is incident on a sphere with a gain of 10^{12} through a diameter, the radiation density will be 10^{7} at the center and roughly 10^{13} times the fractional solid angle of the outward radiation at the edges of the cloud. If the angular distribution of the radiation is more than a few milliradians wide the radiation density and hence the saturation will be largest at the surface. This phenomenon has been observed in other one dimensional geometries in laboratory lasers, and has been suggested by many authors to occur in astrophysical masers as well. The apparent reduction in source diameter and the increase of saturation toward the outer edges of a spherical region are shown to be related in the following sections.

In the following three sections we will solve the transfer equation for the limiting cases of almost no saturation, partial saturation with a central core of unsaturated amplification, and total saturation. The results are presented graphically in Chapter IV.

The derivations here are restricted in several ways. Since the transfer equation explicitly contains the solution of the two-level population equations given in the previous chapter, the solutions pre-

sented here entrain all the earlier restrictions. One significant restriction is that the line shapes for emission and absorption be the same; if the line of interest is an incomplete overlap of several lines, this may not be true. Polarization, scattering, and Zeeman effects will be neglected and with them, any cross relaxation effects. Inclusion of the hyperfine structure and the Zeeman structure in the rate equations would lift some of these conditions, but the anticipated width for the infrared lines exceed the energy gaps even with line narrowing by maser amplification.

The equation of transfer from Chapter II is:

$$\frac{d\mathcal{J}}{ds} = \left(\frac{\beta}{\beta+\mathcal{J}}\right)\mathcal{J} + S + \frac{1}{2}\left(\frac{\beta}{\beta+\mathcal{J}}\right) \quad . \qquad \text{(III-A-1)}$$

The most general solution to this equation, assuming that the $\mathcal{J}$ term is only a function of the linear dimension and not of the intensity, is:

$$\mathcal{J}(s) = \mathcal{J}(s_o)\left\{\exp\int_{s_o}^{s}\frac{\beta}{\beta+\mathcal{J}}\,ds'\right\} + \left\{\exp\int_{s_o}^{s}\frac{\beta}{\beta+\mathcal{J}}\,ds'\right\}\left\{S\int_{s_o}^{s}\left[\exp\int_{y}^{s_o}\frac{\beta}{\beta+\mathcal{J}}\,ds'\right]dy + \frac{1}{2}\int_{s_o}^{s}\frac{\beta}{\beta+\mathcal{J}}\left[\exp\int_{y}^{s_o}\frac{\beta ds'}{\beta+\mathcal{J}}\right]dy\right\} \qquad \text{(III-A-2)}$$

If $\mathcal{J}$ is a function of intensity then this is just an integral form of (III-A-1).

B. Solution of the Transfer Equation for No Saturation

In solving the transfer equation in regions of no saturation the $\mathcal{J}$ term from the population equations is set to zero, so that the stimulated emission has no effect on the populations of the maser levels. This will

occur only if the pumping rate is high enough. If $\mathcal{J}$ is set to zero in the above equation the terms may be integrated to find:

$$\mathcal{J}(s) = \mathcal{J}(s_o)\exp[s-s_o] + (S + 1/2)\{\exp[s-s_o]-1\} \quad , \qquad \text{(III-B-1)}$$

where s is the path length in the medium (refer to Eq. II-E-11).

For a spherical geometry a ray path through the region along the line of sight will make an angle θ with a radius vector. If $\mu = \cos\theta$, the ray path length is $s_o = -R\mu$ to $s = +R\mu$ with R the total radius of the region.

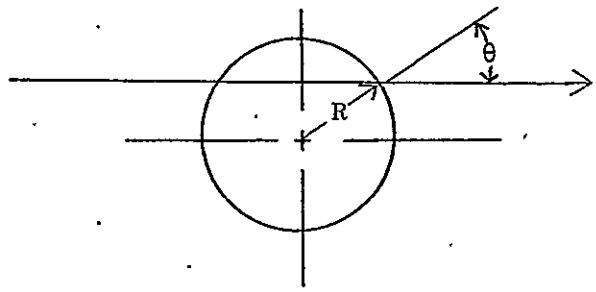

Using these limits, the intensity in the positive direction from (III-B-1) is a function of the total radius R and the offset from the region's center and is given by:

$$\mathcal{J}(R,\mu) = \mathcal{J}(R,-1)\exp[R(\mu+|\mu|)] + (S+1/2)\{\exp[R(\mu+|\mu|)]-1\} \qquad \text{(III-B-2)}$$

where $\mathcal{J}(R,-1)$ is the isotropic background radiation intensity of the appropriate frequency.

The average intensity at a point r in the spherical cloud is given by II-E-7, with $d\Omega = \sin\theta d\theta d\phi = d\mu d\phi$, or:

$$J = \langle I \rangle = \frac{1}{4\pi}\int_{-1}^{+1}\int_{0}^{2\pi} I(r,\mu)d\mu d\phi = \frac{1}{2}\int_{-1}^{+1} I(r,\mu)d\mu \qquad \text{(III-B-3)}$$

The resulting average intensity for totally unsaturated regions is:

$$\mathcal{J}(R)=\frac{\mathcal{J}_o}{2}\left\{\frac{e^{2R}-1}{2R}+1\right\}+\frac{1}{2}\left(S+\frac{1}{2}\right)\left\{\frac{e^{2R}-1}{2R}-1\right\} \qquad \text{(III-B-4)}$$

where $\mathcal{J}_o$ is the background flux $\mathcal{J}(R,-1)$ incident in the rear of the cloud.

Equations (III-B-2) and (III-B-4) will be valid as long as the condition $\mathcal{J} \ll \beta$ remains valid. The maximum size of such a region may be established by replacing the inequality with an equality, so that the stimulated rate of population transfer is equal to the average natural decay:

$$BJ = \frac{1}{2}(A+\Gamma_a) \qquad \text{(III-B-5)}$$

In the dimensionless forms of the preceding chapter this condition becomes:

$$\beta = \mathcal{J} . \qquad \text{(III-B-6)}$$

Setting the intensity given by (III-B-4) equal to β gives the radius R_1 which is the upper limit for the size of a totally unsaturated region from the relationship:

$$\frac{1}{\alpha}=\frac{1}{2}\left[\frac{e^{2R_1}-1}{2R_1}+1\right]+\frac{1}{4S}\left\{2\mathcal{J}_o\left(\frac{e^{2R_1}-1}{2R_1}+1\right)+\frac{e^{2R_1}-1}{2R_1}-1\right\} \qquad \text{(III-B-7)}$$

where $1/\alpha$ is given by the pumping mechanism.

The dimensionless parameters in the preceding equations may be related to the physical conditions of the maser region with the following

equations. The physical size is related to the parameters of the region by:

$$C^*D = D\left[\left(\frac{A}{1\ \text{sec}^{-1}}\right)\left(\frac{\lambda}{100\mu}\right)^3\left(\frac{10^{-6}}{\Delta\nu/\nu}\right)\left(\frac{N_{OH}}{1\ \text{cm}^{-3}}\right)\left(\frac{N_u}{N_{OH}}\right)\left(\frac{1}{1.51 \times 10^{12}\text{cm}}\right)\right]$$

where D is the physical diameter in cm, and

$$T_\nu = \frac{h\nu}{k} = \begin{cases} 143^\circ K & \text{for } \lambda = 100\mu \\ 0.08^\circ K & \text{for } \lambda = 18\ \text{cm} \end{cases}$$

$$r = \frac{N_\ell}{N_u} \quad , \quad S = \frac{1}{2}\left(\frac{1+r}{1-r}\right) \quad , \quad \mathcal{J} = \frac{T_B}{T_\nu} \quad , \quad R = C^*D(1-r) \quad ,$$

$$\left[\frac{1}{\alpha} - 1\right] = \left(1 + \frac{\Gamma_a}{A}\right)\left(\frac{1-r}{1+r}\right) \qquad \text{(III-B-8)}$$

The saturation boundary and the intensity then are dependent on three parameters: the scaled size of the region C^*D, the population ratio r, and the background intensity $\mathcal{J}_o = T_o/T_\nu$. The boundary relation becomes:

$$\left(1 + \frac{\Gamma_a}{A}\right) = \left[\frac{T_o}{T_\nu}\ \frac{e^{2R_1}-1}{2R_1}+1\right]+\left(\frac{1}{1-r}\right)\left[\frac{e^{2R_1}-1}{2R_1} - 1\right] \qquad \text{(III-B-9)}$$

and the intensity at the center of the observed disk is

$$\frac{T_B}{T_\nu} = \frac{T_o}{T_\nu}\, e^{2R} + \left(\frac{1}{1-r}\right)\left(e^{2R} - 1\right) \qquad \text{(III-B-10)}$$

The distribution of intensity across the disc given by equation (III-B-2) is essentially gaussian. The half width of this is related to the apparent source size, and is proportional to $R^{1/2}$. Using the scale length (C^*D), the ratio of real to apparent size is:

$$\frac{D_{real}}{D_{app}} = \frac{C^*D}{(C^*D)^{1/2}} \sim (C^*D)^{1/2} \qquad \text{(III-B-11)}$$

C. Partially Saturated Spherical Clouds

If the radiation density at the outer edges of the spherical cloud of OH exceeds β, or equivalently if the radius of the cloud exceeds R_1 as given in the preceding section, at least part of the cloud will be saturated. Saturation is characterized by a high radiation density and hence high stimulated transition rates, which depopulates the upper of the two states involved in the maser, and in the extreme forces the two populations to become equal. The transfer equation is characterized by small gain so that:

$$\lim_{x \to 0} [(S+1/2)(e^x-1)] = (S+1/2)x \qquad \text{(III-C-1)}$$

and the gain is proportional to the path length. Logically, higher pumping rates in the maser mechanism will reduce the degree of saturation if all other parameters are constant, and lower rates will increase saturation. If the pump rate is a constant, then larger values for the cloud radius will give higher radiation densities and greater saturation.

We can model this saturation behavior in a spherical cloud as a core of radius a which is unsaturated surrounded by a shell of saturated population. The intensity in the shell is directed mainly outward with a mean value of $\mathcal{J}(a) = \beta$ at the boundary between the core and the saturated shell. The gain outward of the boundary is proportional to the path length, so that the transfer equation may be solved using:

$$\mathcal{J}(r) = \frac{\beta r}{3} - \frac{\beta a}{3}\left(\frac{a^2}{r^2}\right) + \beta \frac{a^2}{r^2} \qquad \text{(III-C-2)}$$

from Goldreich and Keeley (1972), where the first term is the outward component of the boundary intensity times the linear gain, the second

term is the correction for measuring $\underline{r}$ from the center of the sphere, and the third term is the additional contribution of the core in the spherical geometry. Lang and Bender (1973) consider a similar approximation for the case of complete saturation as a first estimate and solve the transfer equation and coupled rate equations iteratively using numerical methods. Twenty iterations change the above expressions by less than twenty percent and we conclude that (III-C-2) is a reasonable approximation for the gain behavior in saturated regions.

The characteristic integral to be evaluated in the transfer equation solution (III-A-2) is:

$$\int \frac{\beta ds}{\beta+\mathcal{J}} = \int \frac{3r^2 dr}{r^3+3r^2+a^2(3-a)} \quad . \qquad \text{(III-C-3)}$$

The third order polynomial in the denominator of this integral makes exact evaluation very difficult, but the problem can be highly simplified by a few reasonable approximations. If the gain rate in the saturated region is large enough then $\beta \ll \mathcal{J}$ will hold and the integral becomes:

$$\int \frac{\beta ds}{\beta+\mathcal{J}} \rightarrow \int \frac{\beta ds}{\mathcal{J}} = \int \frac{3r^2 dr}{r^3+a^2(3-a)} \quad . \qquad \text{(III-C-4)}$$

This will be shown to become unworkable for small values of the core radius $\underline{a}$ (see page 53); for small values of $\underline{a}$ the last term in the denominator of (III-C-3) is negligible, and the integral becomes:

$$\int \frac{\beta}{\beta+\mathcal{J}} \, ds \rightarrow \int \frac{3}{3+r} \, dr \quad . \qquad \text{(III-C-5)}$$

These two integrals are easily evaluated; the first is:

$$\int_{s_o}^{s} \frac{3r^2 dr}{r^3+a^2(3-a)} = \ell n \left| \frac{s^3+a^2(3-a)}{s_o^3+a^2(3-a)} \right| \qquad \text{(III-C-6)}$$

and the second is:

$$\int_{s_o}^{s} \frac{3}{3+r}\, dr = \ell n \left| \frac{(s+3)^3}{(s_o+3)^3} \right| \qquad \text{(III-C-7)}$$

Goldreich and Keeley incorrectly apply (III-C-6) to the limit of small a, hence finding a discontinuity in the core size as complete saturation is approached.

Relationships for the core size and the total intensity may be found by integrating along a line of sight through the center of the cloud using equation (III-A-2). At the rear core boundary:

$$\mathcal{J}(a,-1) = \mathcal{J}(R,-1)\left[\frac{R^3+3a^2-a^3}{3a^2}\right] + \frac{S}{3a^2}\left[\frac{R^4}{4} + 3a^2R - a^3R - \frac{a^4}{4} - 3a^3 + a^4\right] + \frac{1}{6a^2}\left[R^3 - a^3\right] \qquad \text{(III-C-8)}$$

for the approximation (III-C-4). If the gain in the rear side of the cloud is not too large the relation $\mathcal{J}(a,-\mu) = \mathcal{J}(a,-1)$ holds, hence $\mathcal{J}(a,+\mu)$ is given by:

$$\mathcal{J}(a,+\mu) = \mathcal{J}(a,-1)e^{2a\mu} + (S+1/2)(e^{2a\mu}-1)$$

and

$$\mathcal{J}(a) = \frac{\mathcal{J}(a,-1)}{2}\left[\frac{e^{2a}-1}{2a}+1\right] + \frac{1}{2}\left(S+\frac{1}{2}\right)\left[\frac{e^{2a}-1}{2a} - 1\right] \qquad \text{(III-C-9)}$$

Combining (III-C-8) and (III-C-9) gives the relationship between the core size, the total size, and the pumping rate, with $\mathcal{J}(a) = \beta$:

$$\left(\overline{1 + \frac{\Gamma_a}{A}}\right) = \frac{T_o}{T_\nu}\left(\frac{e^{2a}-1}{2a}+1\right)\left(\frac{R^3+3a^2-a^3}{3a^2}\right)$$

$$-\left(\frac{e^{2a}-1}{2a}+1\right)\left(\frac{1}{6a^2}\right)\left(\frac{R^4}{4} + 3a^2R - a^3R - \frac{a^4}{4} - 3a^2 + a^4 - R^3 + a^3\right)$$

$$+\left(\frac{1}{1-r}\right)\left\{\frac{e^{2a}-1}{2a} - 1 + \left(\frac{e^{2a}-1}{2a}+1\right)\frac{1}{3a^2}\left(\frac{R^4}{4}+3a^2R - a^3R - \frac{a^4}{4} - 3a^2 + a^4\right)\right\}. \quad \text{(III-C-10)}$$

The integration path is completed by applying (III-C-8) to find the surface intensity on the line of sight:

$$\mathcal{J}(R,1) = \mathcal{J}(R,-1)\left[\frac{R^3+3a^2-a^3}{3a^2}\right]^2 e^{2a} + \left(\frac{R^3-a^3}{6a^2}\right)\left[1 + \left(\frac{R^3+3a^2-a^3}{3a^2}\right) e^{2a}\right]$$

$$+ \frac{S}{3a^2}\left\{(R^3+3a^2-a^3)(e^{2a}-1) + \left[\frac{R^4}{4} + 3a^2R - a^3R - \frac{a^4}{4} - 3a^3 + a^4\right]\right.$$

$$\left.\times\left[1 + \left(\frac{R^3+3a^2-a^3}{3a^2}\right) e^{2a}\right]\right\} + \left(\frac{e^{2a}-1}{2}\right)\left(\frac{R^3+3a^2-a^3}{3a^2}\right). \quad \text{(III-C-11)}$$

It can be seen that in the limit $R = a$ the equations (III-C-10) and (III-C-11) become equations (III-B-9) and (III-B-2) respectively. For small values of a (III-C-10) looses meaning as the only solution for $a = 0$ is the trivial $R = 0$ for all α and (III-C-11) becomes useless. Furthermore, equation (III-C-11) is cumbersome to use in finding the brightness temperature.

The second approximation (III-C-5) gives an indication of the behavior of the cloud as the saturation becomes complete. Again we integrate along the line of sight on a diameter of the cloud. For the back half of the saturated shell the intensity is:

$$\mathcal{J}(a,-1) = \mathcal{J}_o\left[\frac{3+R}{3+a}\right]^3 + \frac{S}{4}\left[\left(\frac{3+R}{3+a}\right)^4 - 1\right](3+a) + \frac{1}{2}\left[\left(\frac{3+R}{3+a}\right)^3 - 1\right] \quad . \qquad \text{(III-C-12)}$$

The intensity crossing the core is again given by equations (III-C-9) so that the intensity at the core boundary is:

$$\mathcal{J}(a) = \frac{1}{2}\left[\frac{e^{2a}-1}{2a} + 1\right]\left\{\mathcal{J}_o\left(\frac{3+R}{3+a}\right)^3 + \frac{S}{4}\left[\left(\frac{3+R}{3+a}\right)^4 - 1\right](3+a) + \frac{1}{2}\left[\left(\frac{3+R}{3+a}\right)^3 - 1\right]\right\}$$
$$+ \frac{1}{2}\left(S + \frac{1}{2}\right)\left[\frac{e^{2a}-1}{2a} - 1\right] \quad . \qquad \text{(III-C-13)}$$

Setting $\mathcal{J}(a) = \beta$ again gives the relationship between the core size, the total size, and the pumping rate as:

$$\left(1 + \frac{\Gamma_a}{A}\right) = \frac{T_o}{T_\nu}\left(\frac{e^{2a}-1}{2a} + 1\right)\left(\frac{3+R}{3+a}\right)^3 + \left(\frac{2}{1-r}\right)\left\{\frac{1}{2}\left(\frac{e^{2a}-1}{2a} + 1\right)\left[\left(\frac{3+R}{3+a}\right)^4\left(\frac{3+a}{4}\right) + \frac{1-a}{4}\right] - 1\right\}$$
$$+ \frac{1}{2}\left(\frac{e^{2a}-1}{2a} + 1\right)\left[\left(\frac{3+R}{3+a}\right)^3 - \left(\frac{3+R}{3+a}\right)^4\left(\frac{3+a}{4}\right) - \frac{1-a}{4}\right]\right\}. \qquad \text{(III-C-14)}$$

The peak intensity is given at $(R,+1)$ by:

$$\frac{T_B}{T_\nu} = \frac{T_o}{T_\nu}\, e^{2a}\left(\frac{3+R}{3+a}\right)^6 + \frac{1}{2}\left[e^{2a}\left(\frac{3+R}{3+a}\right)^6 - 1\right]$$
$$+ \frac{1}{2}\left(\frac{2}{1-r} - 1\right)\left\{e^{2a}\left(\frac{3+R}{3+a}\right)^3\left[\left(\frac{3+R}{3+a}\right)^4\left(\frac{3+a}{4}\right) + \frac{1-a}{4}\right] - \left(\frac{3+R}{3+a}\right)^3 + \left(\frac{3+R}{3+a}\right)^4\left(\frac{3+a}{4}\right) - \frac{3+a}{4}\right\}.$$
$$\text{(III-C-15)}$$

and once more these formulae reduce to the unsaturated case when $R = a$.

We can now determine the limit for the cloud to retain an unsaturated core by setting $R = R_2$ at $a = 0$ in equation (III-C-14) above. The

resulting relationship for R_2 is:

$$\left(1 + \frac{\Gamma_a}{A}\right) = 2\,\frac{T_o}{T_\nu}\left(\frac{3+R_2}{3}\right)^3 + \frac{3}{4}\left(\frac{2}{1-r}\right)\left[\left(\frac{3+R_2}{3}\right)^4 - 1\right] \quad . \qquad \text{(III-C-16)}$$

Again, equations (III-C-14) and (III-C-15) become equations (III-B-7) and (III-B-2) when $R = a$. Furthermore, the solution for the first approximation matches the solution for the second approximation at $R = a$, so that for small values of R the second approximation will best represent the maser emission. This will also apply for large values of R if the saturation is almost complete and equations (III-C-14) and (III-C-15) will describe the emission. Otherwise the first approximation is the appropriate choice and equations (III-C-10) and (III-C-11) should be used. The core size is given by (III-C-15) or (III-C-10) respectively.

The distribution of intensity is no longer gaussian if the cloud is partially saturated. In the region of the disk near the center the gain through the saturated shell is nearly constant whether or not the line of sight passes through the core. However, the core contributes an extra (exp(2a)-1) to the gain so that even for small core sizes the core dominates the apparent size of the cloud. Since the core's contribution is roughly a gaussian function, the apparent size is given by:

$$\frac{D_{real}}{D_{app}} = \frac{C^*D}{(2C^*L)^{1/2}} \qquad \text{(III-C-17)}$$

where L is the physical size of the unsaturated core. Thus, clouds that are appreciably saturated can appear much smaller than their physical size.

D. Completely Saturated Masers

If R is greater than the value R_2 given by equation (III-C-16) the region is over saturated. The intensity at the center of the cloud exceeds the boundary value of $\mathcal{J}(0) = \beta$ by a factor $K > 1$. The average intensity $\mathcal{J}(r)$ in the transfer equation may be written:

$$\mathcal{J}(r) = K \frac{\beta r}{3} \quad . \tag{III-D-1}$$

To find the solution of the transfer equation in this case we apply (III-D-1) to the integral (III-A-2), and follow the technique of Section C. The over-saturation parameter K is related to the other variables by setting $\mathcal{J}(0) = \beta K$, giving:

$$\left(1 + \frac{\Gamma_a}{A}\right) = 2\frac{T_o}{T_\nu}\left(\frac{1}{K}\frac{3+KR}{3}\right)^{3/K} + \frac{1}{K}\left(\frac{3+KR}{3}\right)^{3/K} - \frac{1}{K} + \left(\frac{3}{3+K}\right)\left(\frac{1}{K}\right)\left[1 - \left(\frac{3+KR}{3}\right)^{3/K+1}\right]$$

$$+ \left(\frac{3}{3+K}\right)\left(\frac{1}{K}\right)\left(\frac{2}{1-r}\right)\left[\left(\frac{3+KR}{3}\right)^{3/K+1} - 1\right] \quad . \tag{III-D-2}$$

The peak brightness temperature is given at the center of the disk by:

$$\frac{T_B}{T_\nu} = \frac{T_o}{T_\nu}\left(\frac{3+KR}{3}\right)^{6/K} + \frac{1}{2}\left(\frac{3}{3+K}\right)\left(\frac{2}{1-r} - 1\right)\left[\left(\frac{3+KR}{3}\right)^{3/K} + 1\right]\left[\left(\frac{3+KR}{3}\right)^{3/K+1} - 1\right]$$

$$+ \frac{1}{2}\left[\left(\frac{3+KR}{3}\right)^{6/K} - 1\right] \quad . \tag{III-D-3}$$

With the gain in the maser roughly proportional to the path length, the saturated maser has a Lorentzian intensity distribution and the half-intensity points are at about 0.7 R. Then the apparent size is related by:

$$\frac{D_{real}}{D_{app}} = 1.4 \quad . \tag{III-D-4}$$

Lang and Bender (1973) give a value of about 3.8 for the above ratio by considering in detail the intensity distribution across the disc.

E. Estimating the Emitted Intensity

Equations (III-B-10), (III-C-15), and (III-D-3) give the maximum brightness temperature of the maser emission, at the center of the observed disc. This could be converted into an intensity if the size of the disc were known in sterradians with the standard formula, but since the OH cloud will probably be unresolved in the receiving antenna, the effective brightness temperature of the entire disc is needed. The effective brightness is essentially the average brightness temperature over the physical disc, and for unsaturated masers is given by:

$$\langle T_B \rangle = T_B\Big|_{max} \times \frac{1}{2C^{*}D(1-r)} \qquad \text{(III-E-1)}$$

or for fully saturated masers by:

$$\langle T_B \rangle = T_B\Big|_{max} \times \frac{1}{C^{*}D(1-r)} \qquad \text{(III-E-2)}$$

Partially saturated masers with a core of size L have an average brightness temperature of approximately:

$$\langle T_B \rangle = T_B\Big|_{max} \times \left[\frac{1}{2C^{*}L(1-r)} + \frac{1}{C^{*}D(1-r)}\right] \qquad \text{(III-E-3)}$$

Using these the intensity of the maser emission can be estimated from equations (IV-D-1) and (IV-D-2).

CHAPTER IV

A GRAPHICAL SOLUTION OF THE TRANSFER EQUATION

A. Introduction.

The theoretical analysis of molecular line emission from interstellar sources involves the simultaneous solution of the equations for line transfer and population equilibrium. Most of the emission of astrophysical interest is very simple and any number of simplifying assumptions can be introduced in the solution of the coupled rate and transfer equations without loosing physical significance. The key to these simplifications is the assumption of local thermodynamic equilibrium; remarkable agreement between theory and observation has been achieved under this assumption for a wide variety of astrophysical sources. For a few radio emission sources involving fine structure emission from OH and other molecules, this assumption falls far short of adequate. Brightness temperatures exceeding 10^{13} ^{o}K make any LTE considerations untennable for these sources; the only currently acceptable explanation for the intense radiation is amplification by stimulated emission.

This maser action makes theoretical analysis very difficult because the population and transfer equations become interdependent and very nonlinear. Various attempts at the solutions have involved ignoring the rate equations while solving the transfer equations for stimulated emission, approximating a transfer equation in population solutions, and solving a coupled two level rate and transfer equation. Chapter III presented a solution of a two level maser of spherical geometry which couples to a multilevel set of rate equations; this chapter will

describe how those equations can be used graphically to understand the characteristics of the maser action and to predict the intensities of proposed maser emissions.

B. The Parameters of the Maser Emission

The formulae of Chapter III relates the pumping rate, the saturation state, and the intensity to the physical conditions of the maser region. The parameters are used in a dimensionless form and are scaled with the physical conditions in the following manner. The physical diameter is scaled to a dimensionless radius by:

$$R = C^{*} D(1-r)$$

where D is the physical size in centimeters, C^{*} is the scale length:

$$C^{*} = \left(\frac{A_{ij}}{1\ \text{sec}^{-1}}\right)\left(\frac{\lambda}{100\mu}\right)^{3}\left(\frac{10^{-6}}{\Delta\nu/\nu}\right)\left(\frac{N_{OH}}{1\ \text{cm}^{-3}}\right)\left(\frac{N_u}{N_{OH}}\right)\left(\frac{1}{1.51 \times 10^{12}\ \text{cm}}\right) \qquad \text{(IV-B-1)}$$

and r is the unsaturated population ratio n_l/n_u, so that $(1-r)$ is the population difference $\Delta n/n_u$. If there is an unsaturated core in the region, its size is similarly scaled by:

$$a = C^{*} L(1-r)$$

where L is the physical size of the core in centimeters. The pumping rate is given by $(1 + \Gamma/A)$ where A is the spontaneous emission coefficient. The background and emission intensities are given by:

$$\mathcal{J} = \frac{T_B}{T_\nu} \quad , \quad T_\nu = \frac{h\nu}{k} \quad , \quad T_B = \frac{Ic^2}{2k\nu^2} \quad ,$$

$$\mathcal{J}_o = \frac{T_o}{T_\nu} \quad , \quad T_o = \frac{I_o c^2}{2k\nu^2} \quad ; \qquad \text{(IV-B-2)}$$

where T_B is the emission brightness temperature and T_o the background brightness. The state of saturation of the region is given for partially saturated clouds by the size of the unsaturated core; the boundary between the core and the saturated shell is defined as the point where the spontaneous and the stimulated transition rates are equal. If there is no core and the stimulated transition rate exceeds the spontaneous rate throughout the cloud, the emission is characterized by the saturation ratio K of the stimulated transition rate divided by the spontaneous rate at the center of the cloud.

C. A Graphical Solution for the Emission

Equations III-B-10, III-C-15, and III-D-3 give the peak brightness temperature for a spherical cloud, but are hard to use except for the case of unsaturated emission because of the interdependence of the intensity and the saturation state. This section will present a two step graphical analysis of the emission which additionally provides a clear picutre of the character of the maser amplification and the sensitivity of various parameters. The state of saturation in the cloud will be considered first, followed by the intensity determination.

For a region with an unsaturated core the size of the core is related to the total size and the pumping rate by (III-C-14);

$$\left(1+\frac{\Gamma_a}{A}\right) = \frac{T_o}{T_\nu}\left(\frac{3+R}{3+a}\right)^3\left(\frac{e^{2a}-1}{2a}+1\right) + \left(\frac{2}{1-r}\right)\left\{\frac{1}{2}\left(\frac{e^{2a}-1}{2a}+1\right)\left[\left(\frac{3+R}{3+a}\right)^4\left(\frac{3+a}{3}\right) + \frac{1-a}{4}\right] - 1\right\}$$

$$+ \frac{1}{2}\left(\frac{e^{2a}-1}{2a} + 1\right)\left[\left(\frac{3+R}{3+a}\right)^3 - \left(\frac{3+R}{3+a}\right)^4\left(\frac{3+a}{4}\right) - \frac{1-a}{4}\right] . \qquad \text{(IV-C-1)}$$

The region is completely saturated when $a = R$ in the above equation, and has just reached complete saturation when $a = 0$. For regions with a higher saturation level the appropriate equation is (III-D-2);

$$\left(1 + \frac{\Gamma_a}{A}\right) = \frac{1}{K}\left(2\,\frac{T_o}{T_\nu} + 1\right)\left(\frac{3+KR}{3}\right)^{3/k} - \frac{1}{K} - \frac{1}{K}\left(\frac{1+r}{1-r}\right)\left(\frac{3}{3+K}\right)\left[1 - \left(\frac{3+KR}{3}\right)^{\frac{3}{K}} + 1\right]. \quad \text{(IV-C-2)}$$

If the scaled size C^*D is chosen as the independent variable, the pumping rate becomes the dependent function, and the population and saturation ratios become parameters of the relationship. Equations (IV-C-1) and (IV-C-2) then divide the size versus pumping rate field into regions of unsaturated, partially saturated, and over saturated amplification, with the boundaries dependent on the parameters. Figure 4 gives the boundary between unsaturated and partially saturated emission, and figure 5 the boundary between partial saturation and over saturation, with zero background intensity and population ratios between 1 and 10^{-5}. In figure 4 the unsaturated region is to the left of the function line, and in figure 5 the over saturation region is to the right. In the region between the two curves, for a fixed population ratio, the cloud has an unsaturated core. For a population fraction less than 0.01 the partially saturated region at small radius values is negligible, so that the emission can change rapidly from unsaturated to fully saturated with small changes in size or pumping rate.

If the pumping rate and the size of the cloud meet in a region of over saturation, the saturation ratio is an important factor in determining the emission intensity. Figures 6 and 6a show the lines of constant saturation for two values of the population ratio. In both figures, the unsaturated limit is also shown to indicate the limited conditions which

can produce partially saturated emission. For values of the saturation parameter greater than 10^3 the boundary moves very little because the saturation is depleting the upper state population so strongly that further increases in the intensity can have little effect. (Recall that the population ratio r is the value produced by the pumping process without stimulated emission, not the local value of the population which varies radially in the cloud.) In figures 6 and 6a the value of 0.01 for (1-r) corresponds to a one percent population inversion, and a value of 0.1 to a size percent inversion. This is the range of inversion needed to explain the microwave emission.

The effects of the background intensity on the saturation limits can be seen in figure 7 for a population inversion ratio of 0.01. The background radiation increases the degree of saturation for small pumping rates and dominates the saturation level until the size of the region is sufficient for the spontaneous and stimulated transitions in the region to affect the emission. For microwave emission the line temperature T_ν is 0.08°K so even the isotropic 2.7°K cosmological background controls the saturation state at small scaled sizes. For infrared lines around 100 microns the line temperature is 143°K; at this wavelength only a rather bright background would affect the saturation state. The appropriate background temperature to use is the brightness temperature of the background emission multiplied by the fraction of the hemisphere the background source fills as seen by the rear of the maser cloud.

Equation (IV-C-1) also gives a relationship between the overall size of the region and the size of the unsaturated core. For partially saturated regions the core size determines the degree of saturation of

the maser emission. Figures 8 and 9 show the relationship between the core size and the total size for zero background and population ratios of 0.01 and 0.10 respectively. The difference between the unsaturated and the saturated core sizes for a fixed pumping rate is less in figure 9 because the greater inversion allows the intensity to increase as a faster rate with increasing size, hence bringing on saturation at a lower value of C^*D. The most interesting characteristic of these two figures is the rapidity with which the core disappears after a critical size is reached. In figures 8 and 9 the critical size occurs at the elbow of the curves, with the core size going to zero with only a small change in the total size. The critical size of the core is seen to vary only slowly with increasing values of the pumping parameter. If the OH or the H_2O emission regions are only partially saturated with a core near this critical limit and the region is subject to turbulence or other variations which could change C^*D the saturation state and the intensity could vary greatly over short periods of time as the core emission of exponential growth flickers on and off. For a background intensity with T_o/T_ν less than 1000 the relationship between core size and total size is nearly unchanged; for higher values the curves of figures 8 and 9 move slightly to the left, with the critical value of C^*D about fifty percent lower for $T_o/T_\nu = 1000$.

Once the saturation state and the parameters of the maser region are known, the determination of the emission intensity is straightforward. Equation (III-B-10) gives the maximum possible brightness temperature, from an unsaturated region as:

$$\frac{T_B}{T_\nu} = \frac{T_o}{T_\nu} e^{2R} + \left(\frac{1}{1-r}\right)\left(e^{2R}-1\right) \quad . \qquad \text{(IV-C-3)}$$

For the partially saturated case the intensity is (III-C-15):

$$\frac{T_B}{T_\nu} = \frac{T_o}{T_\nu} e^{2a}\left(\frac{3+R}{3+a}\right)^6 + \left[\frac{1}{2} e^{2a}\left(\frac{3+R}{3+a}\right) - 1\right] .$$

$$+ \frac{1}{2}\left(\frac{1+r}{1-r}\right)\left\{e^{2a}\left(\frac{3+R}{3+a}\right)^3\left[\left(\frac{3+R}{3+a}\right)^4\left(\frac{3+a}{4}\right) - \frac{1-a}{4}\right] - \left(\frac{3+R}{3+a}\right)^3 + \left(\frac{3+R}{3+A}\right)^4\left(\frac{3+a}{4}\right) - \frac{3+a}{4}\right\} \quad . \qquad \text{(IV-C-4)}$$

If the region is over saturated, the saturation parameter k characterizes the emission and the intensity is given by (III-D-3):

$$\frac{T_B}{T_\nu} = \frac{T_o}{T_\nu}\left(\frac{3+KR}{3}\right)^{6/K} + \frac{1}{2}\left[\left(\frac{3+KR}{3}\right)^{6/K} - 1\right] + \frac{1}{2}\left(\frac{3}{3+K}\right)\left(\frac{1+r}{1-r}\right)\left[\left(\frac{3+KR}{3}\right)^{3/K} + 1\right]\left[\left(\frac{3+KR}{3}\right)^{\frac{3}{K}+1} - 1\right]. \qquad \text{(IV-C-5)}$$

The intensity of the spherical region and its dependence on the saturation state is presented in figures 10 and 10a for population inversions of one and six percent. The unsaturated limit is the upper limit for the emission from a maser region of the given parameters, and the inversion limit is the lowest emission which can occur with any population inversion. For scaled sizes over a few hundred the saturation state is the most critical parameter of the emission intensity, with more than 10 orders of magnitude between the unsaturated intensity and the inversion limit at $C^*D = 1000$. As the population ratio decreases the maximum intensity approaches the inversion limit. In figure 11 the unsaturated maximum intensity is shown for population inversions down to 10^{-3} percent. This can be used to set upper limits to the possible

emission intensity even if the saturation state is not known. The lower limit on the intensity for any population inversion can be seen in figures 10 or 10a and is independent of the population ratio.

D. Summary

Figures 4 through 11 give a straightforward method for determining the emission intensity from a spherical region of population inversion. The pumping model gives the population ratio and the pumping rate, and the physical conditions gives the scaled size. Figures 4 to 9 are used to determine the state of saturation of the region, and figures 10 and 11 then directly give the peak brightness temperature. The average brightness temperature can then be determined from (III-E-1,2 or 3) and the intensity is given in watts per square centimeter per hertz per sterradian by:

$$I_\nu = \frac{2k\langle T_B \rangle}{\lambda^2} \left\langle \text{watts cm}^{-2}\text{Hz}^{-1}\text{str}^{-1} \right\rangle \qquad \text{(IV-D-1)}$$

Finally the flux can be found from:

$$\mathcal{F}_\nu = \frac{8\pi k\langle T_B \rangle}{\lambda^2} \left(\frac{\Omega_{\text{source}}}{4\pi}\right) \left\langle \text{watts cm}^{-2}\text{Hz}^{-1} \right\rangle \qquad \text{(IV-D-2)}$$

Then the collecting area and the receiver bandwidth are all that is needed to determine the power received at the detector.

CAPTIONS FOR FIGURES 4 THROUGH 11

Figure 4. The boundary between the unsaturated state and the partially saturated state for spherical masers as a function of the pumping rate and the scaled size, for selected parameters of the population fraction. The size is scaled by equation (IV-B-1).

Figure 5. The boundary between the partially saturated state and the fully saturated state for spherical masers as a function of the pumping rate, the scaled size, and the population fraction.

Figure 6. The saturation limits of a spherical cloud with a population fraction of 0.01, showing the region of partial saturation between the unsaturated limit and the saturation limit, and indicating the degree of oversaturation with lines of constant K.

Figure 6a. The saturation limits for a population fraction of 0.10.

Figure 7. The effects of the background intensity on the partial saturation boundaries as a function of the ratio of background brightness temperature to the line temperature $h\nu/k$ for a population fraction of 0.01.

Figure 8. The relationship between the size of the unsaturated core and the total size for zero background intensity and a population fraction of 0.01, at various pumping rates, showing that the unsaturated core disappears with a limited variation in the total size.

Figure 9. The relationship of figure 8 for a population fraction of 0.10.

Figure 10. The maximum brightness temperature at the center of the observed disc for a spherical maser with a population fraction of 0.01, as determined by the state of saturation of the cloud. The unsaturated limit is the highest possible brightness for this population fraction, and the inversion limit is the minimum; the saturation limit is the intensity which just causes the unsaturated core to disappear.

Figure 10a. The central brightness of a spherical cloud with a population fraction of 0.10.

Figure 11. The maximum central brightness of spherical masers for a range of population values as a function of the scaled size of the region.

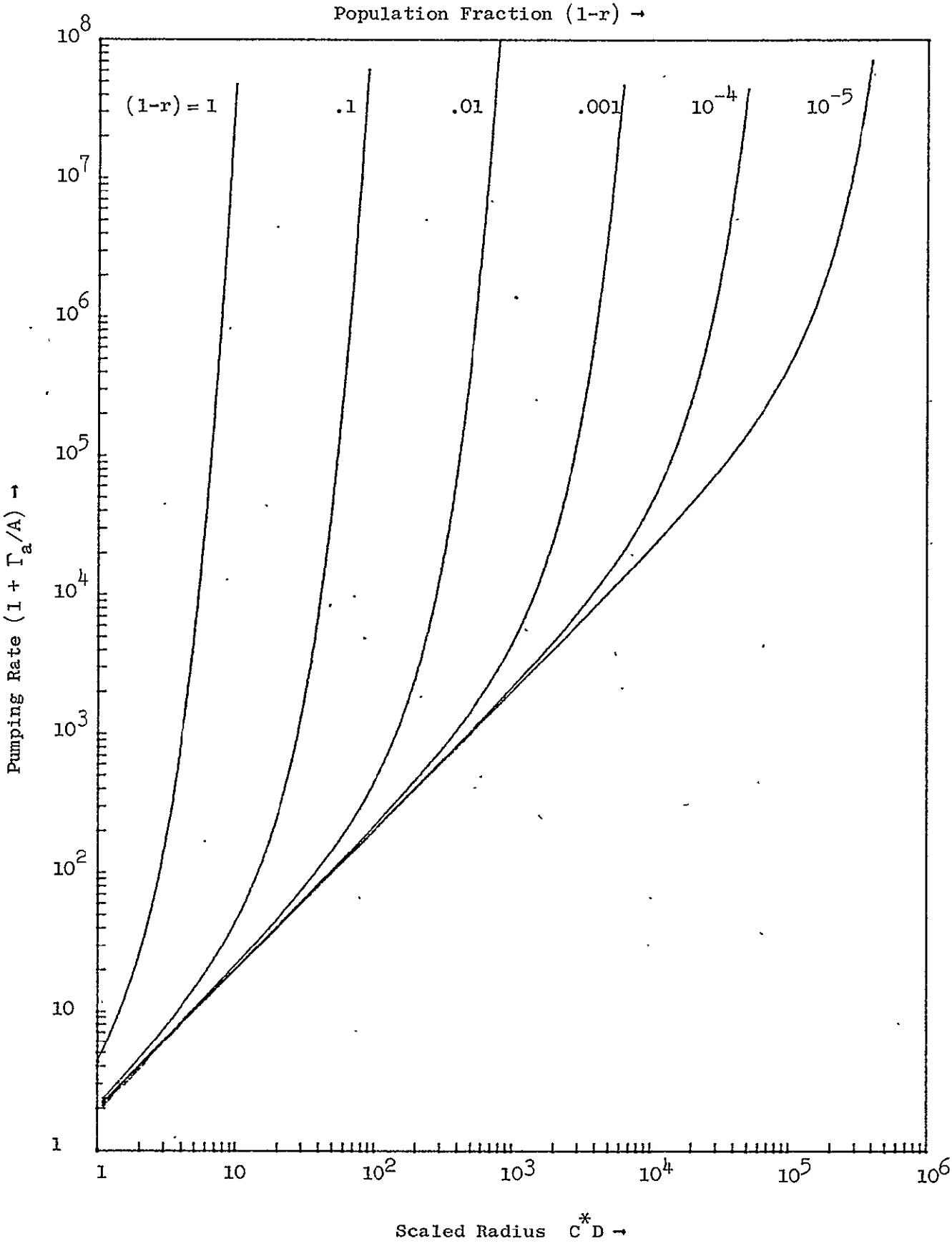

Figure 4. Unsaturated State Limit

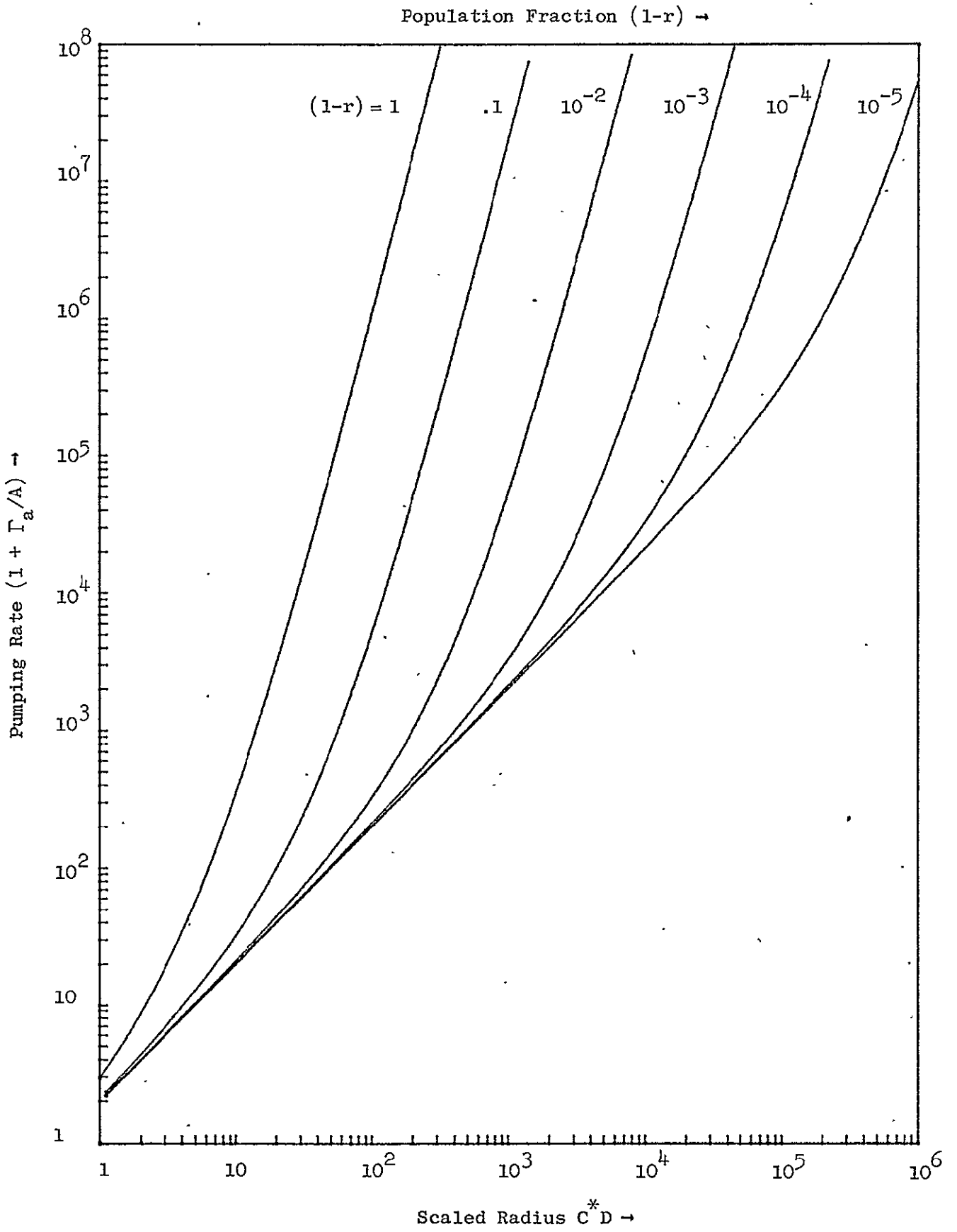

Figure 5. Complete Saturation State Limit

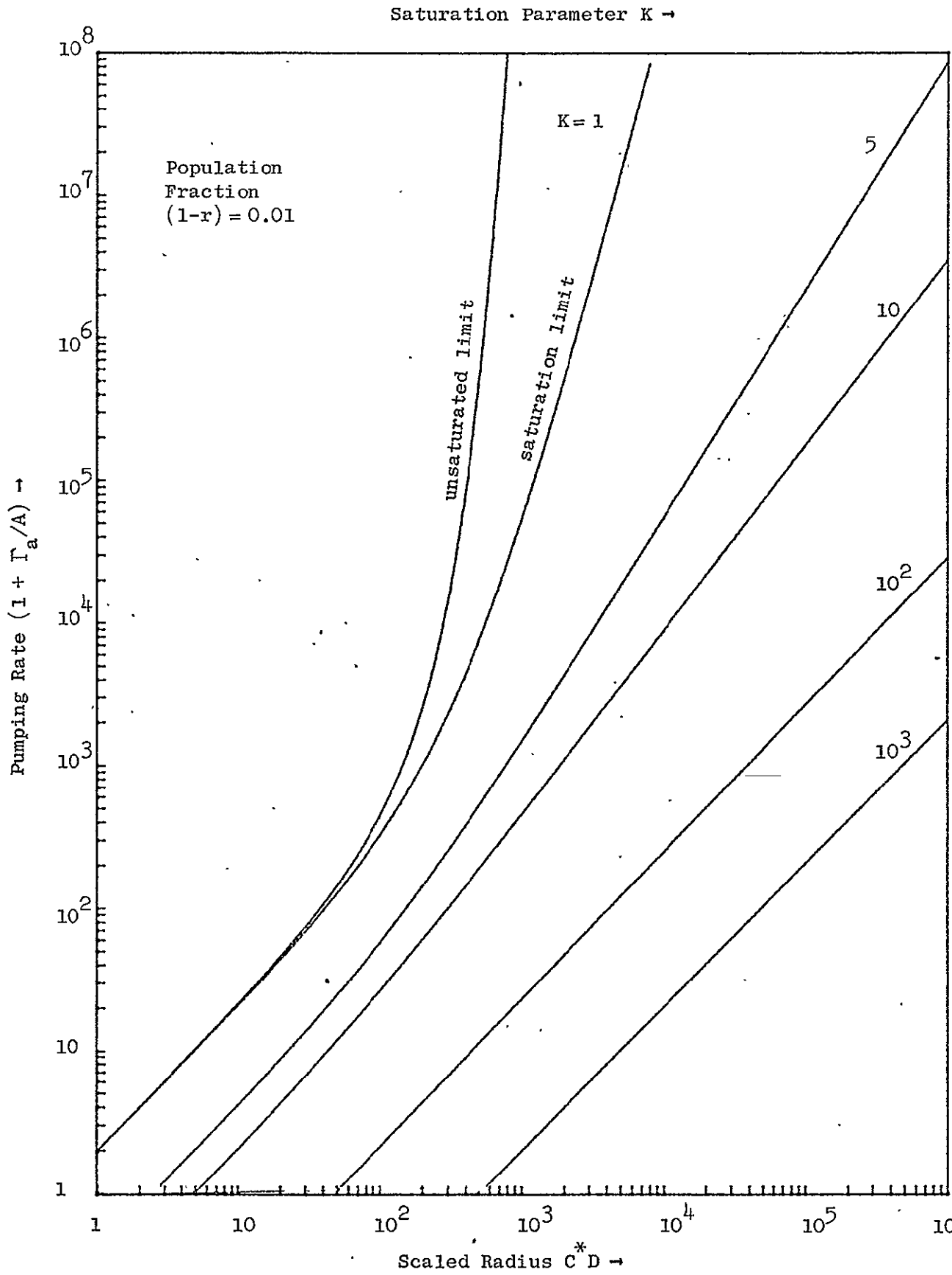

Figure 6. Oversatu ation State Limits

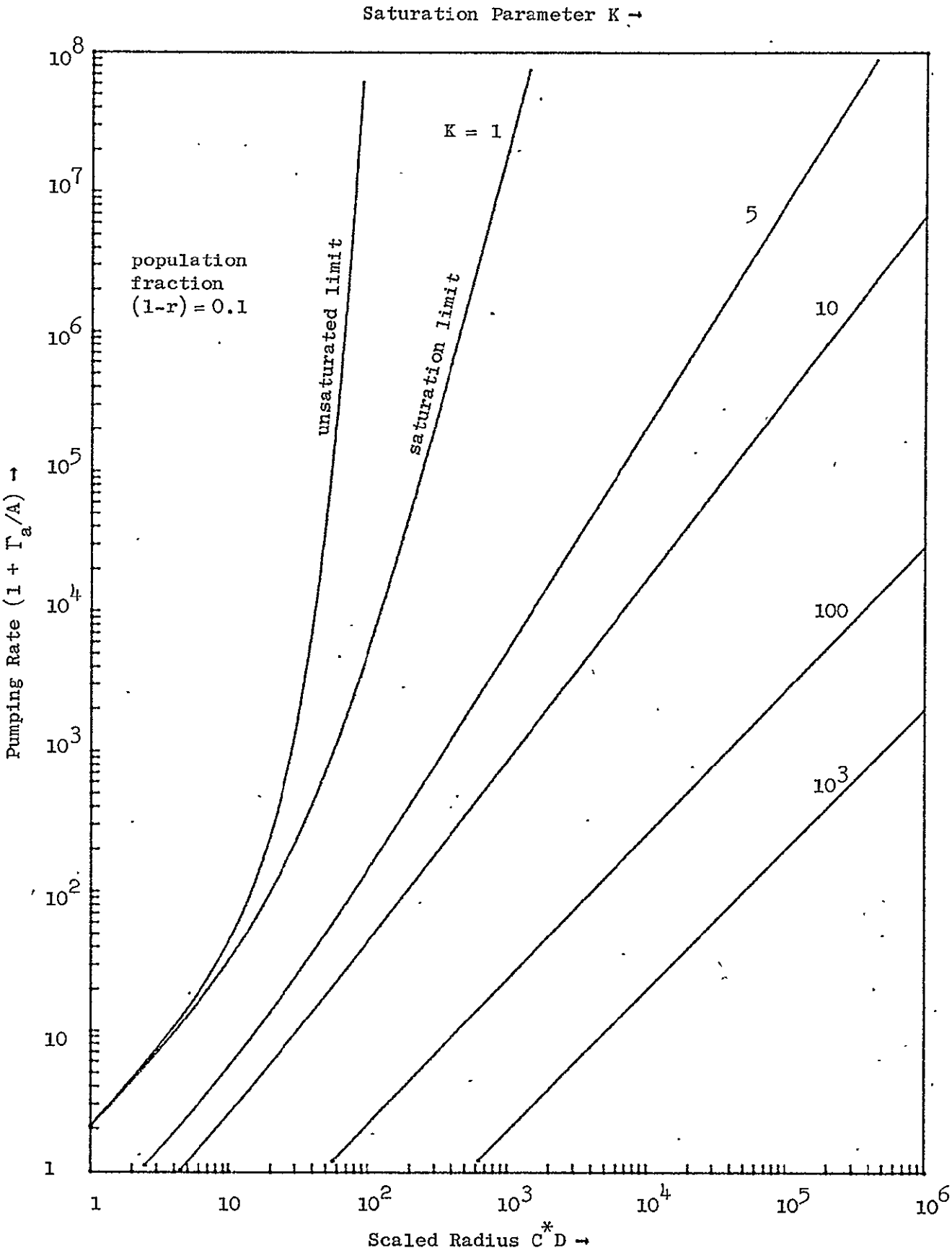

Figure 6a. Oversaturation State Limits

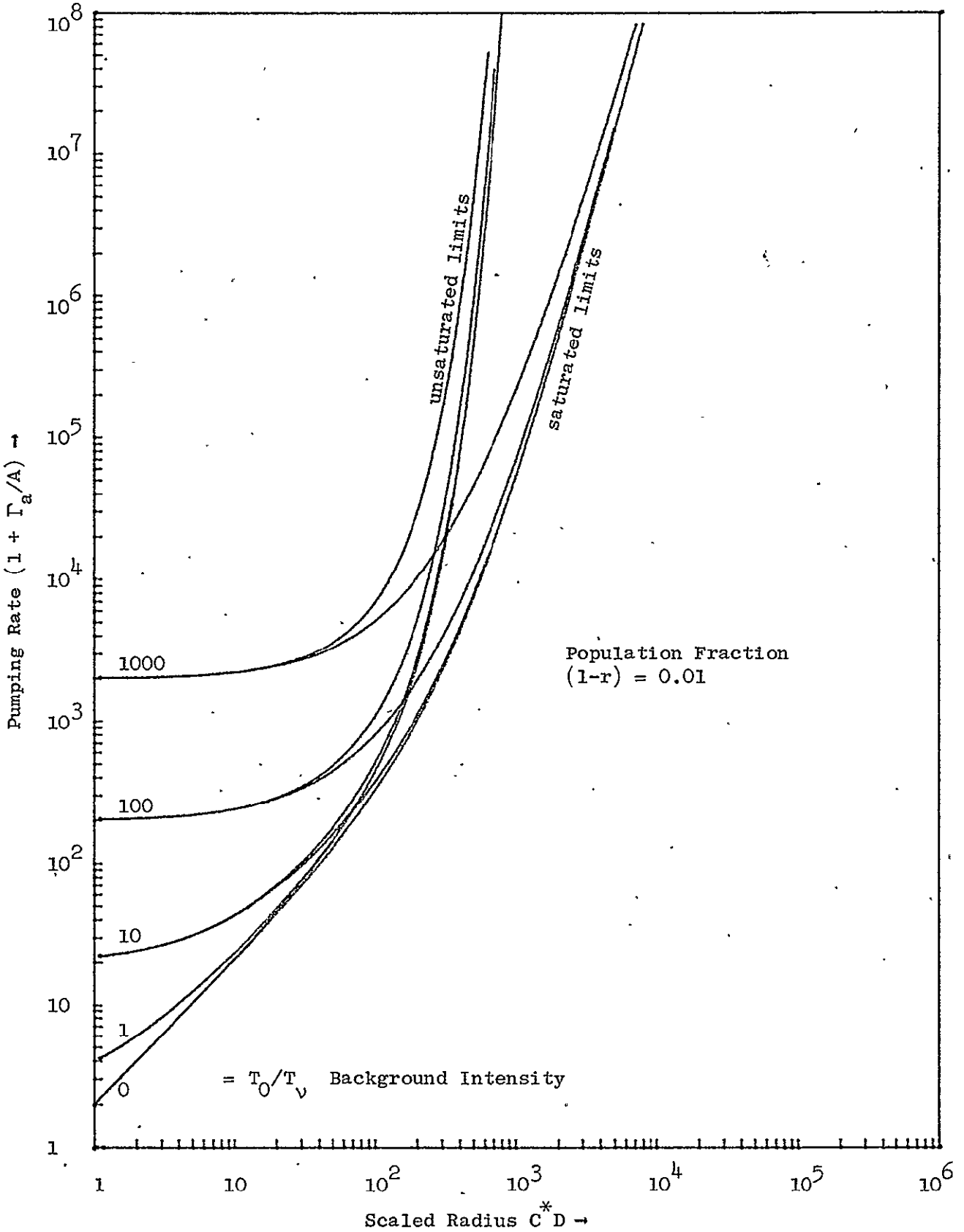

Figure 7. Effects of Background Intensity on Saturation State

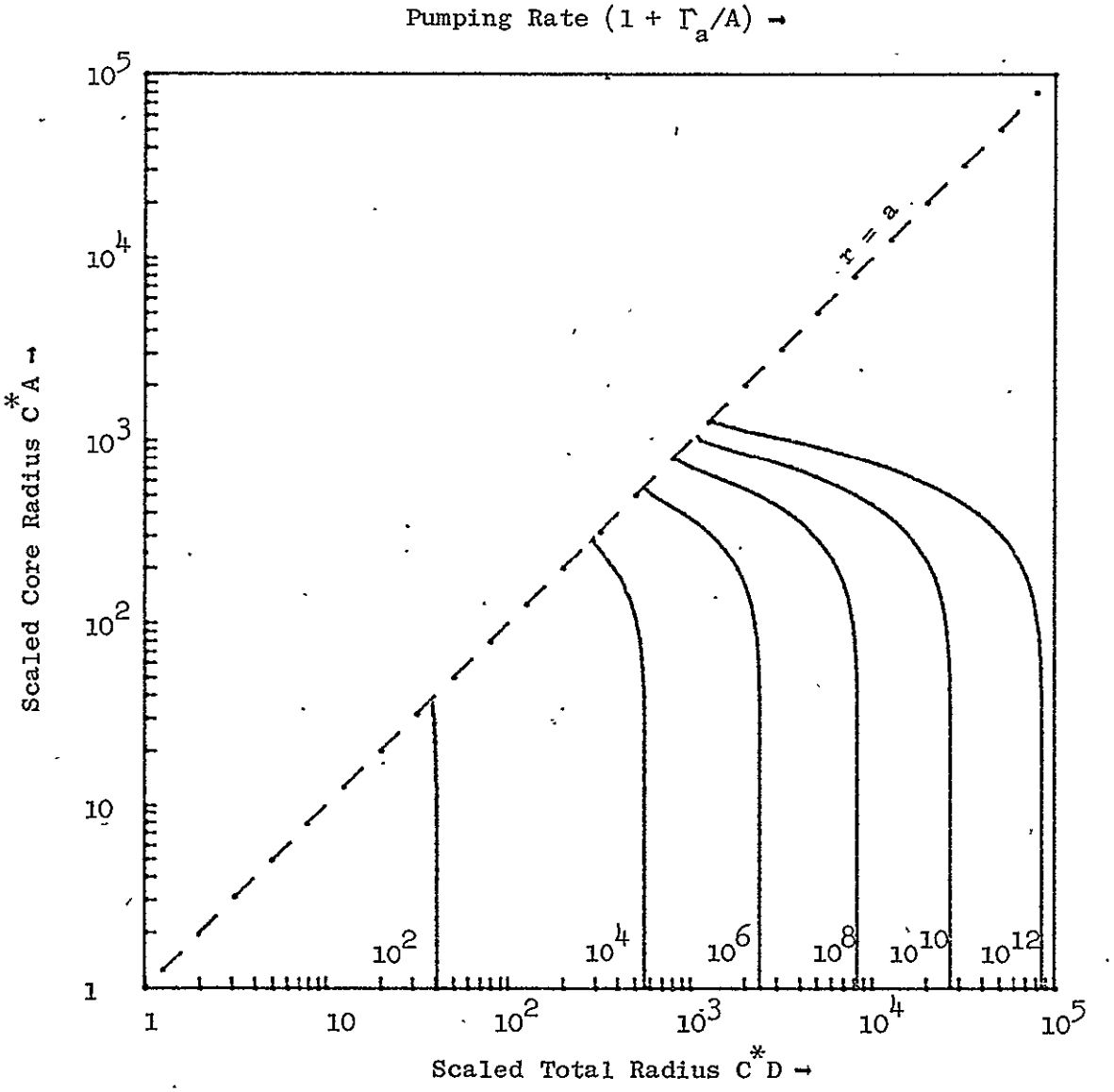

Figure 8. Core Size Function for Population Fraction (1-r) = 0.01

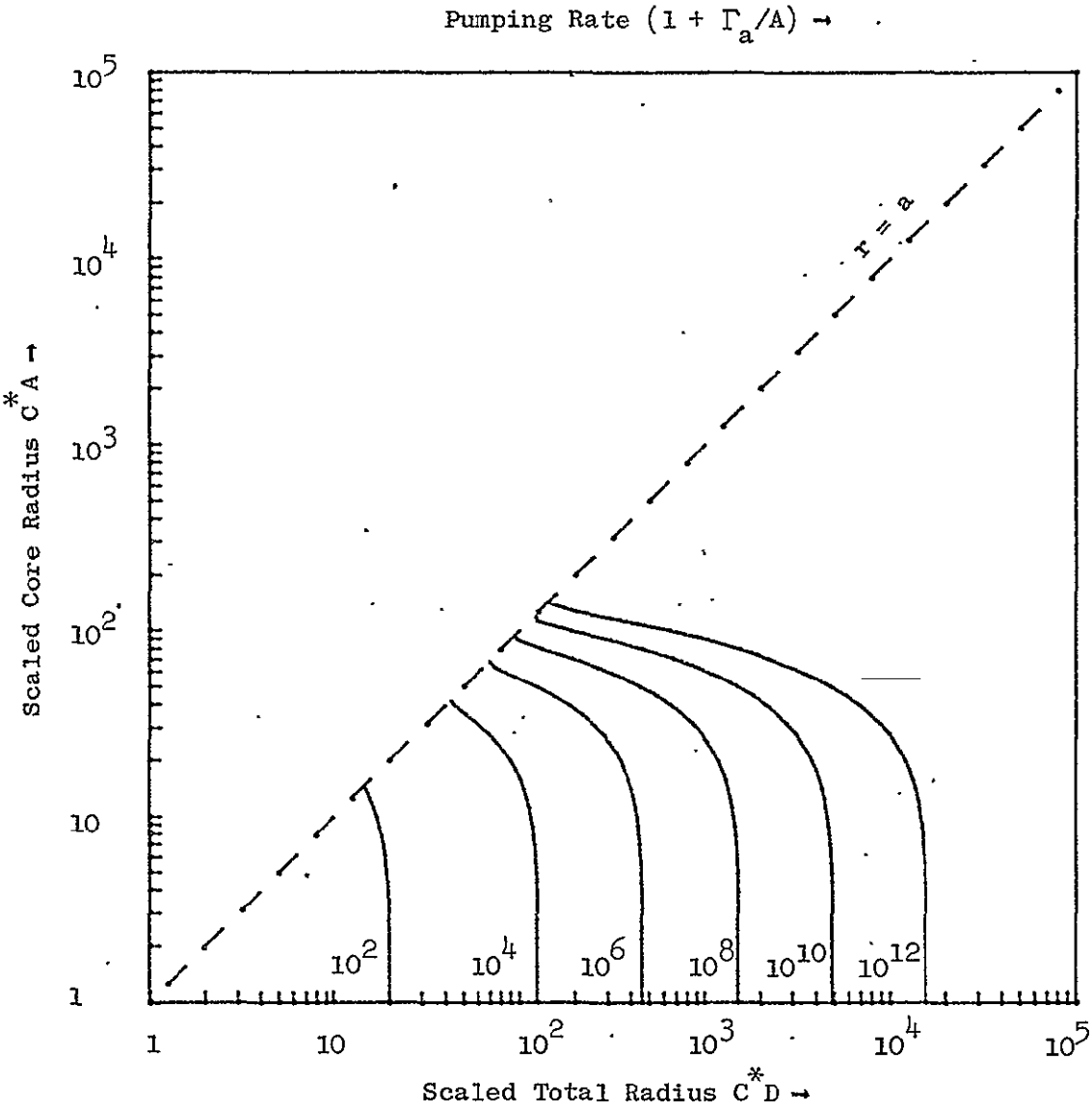

Figure 9. Core Size Function for Population Fraction (1-r) = 0.1 .

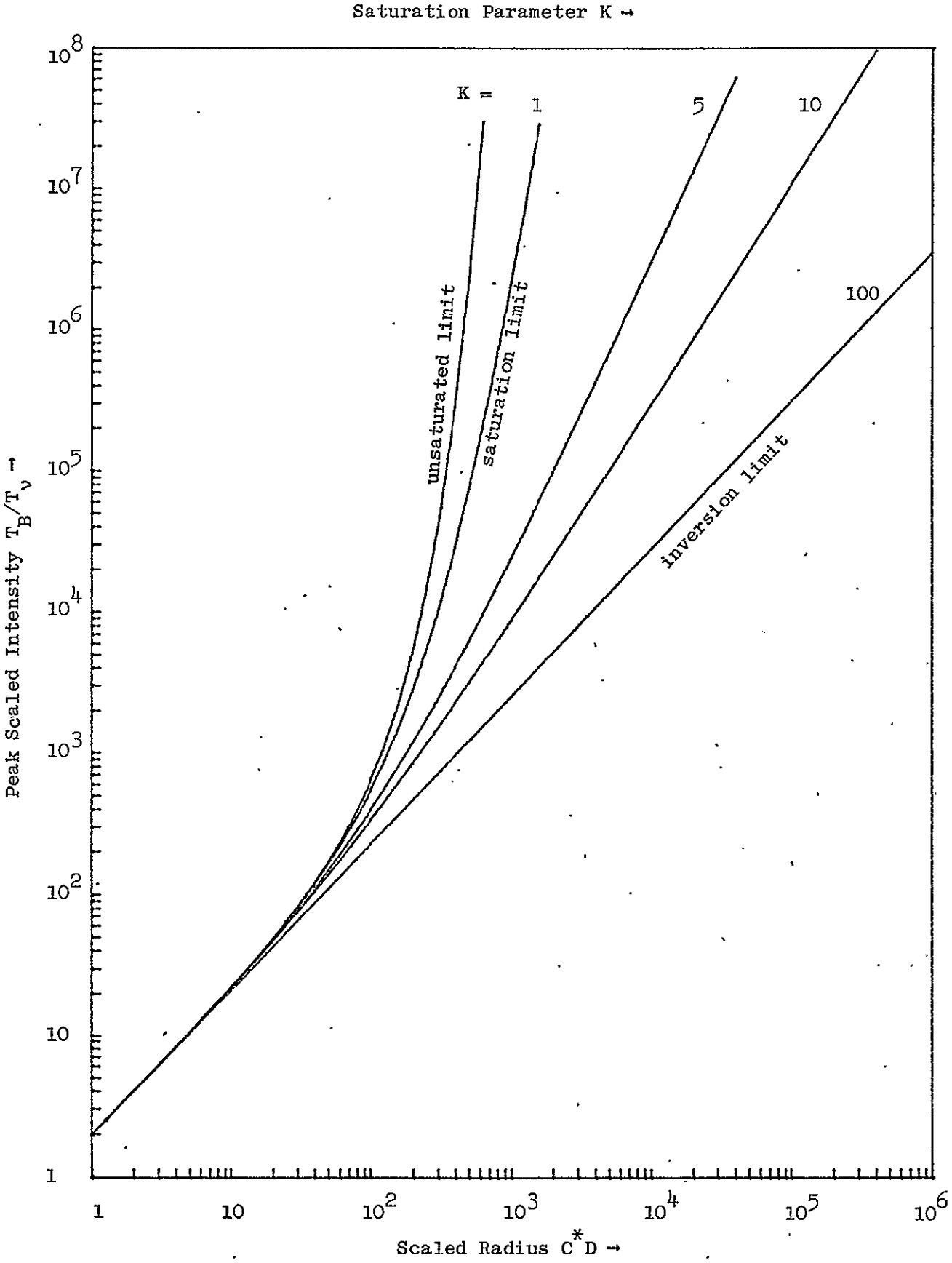

Figure 10. Peak Intensity for Population Fraction (1-r) = 0.01'

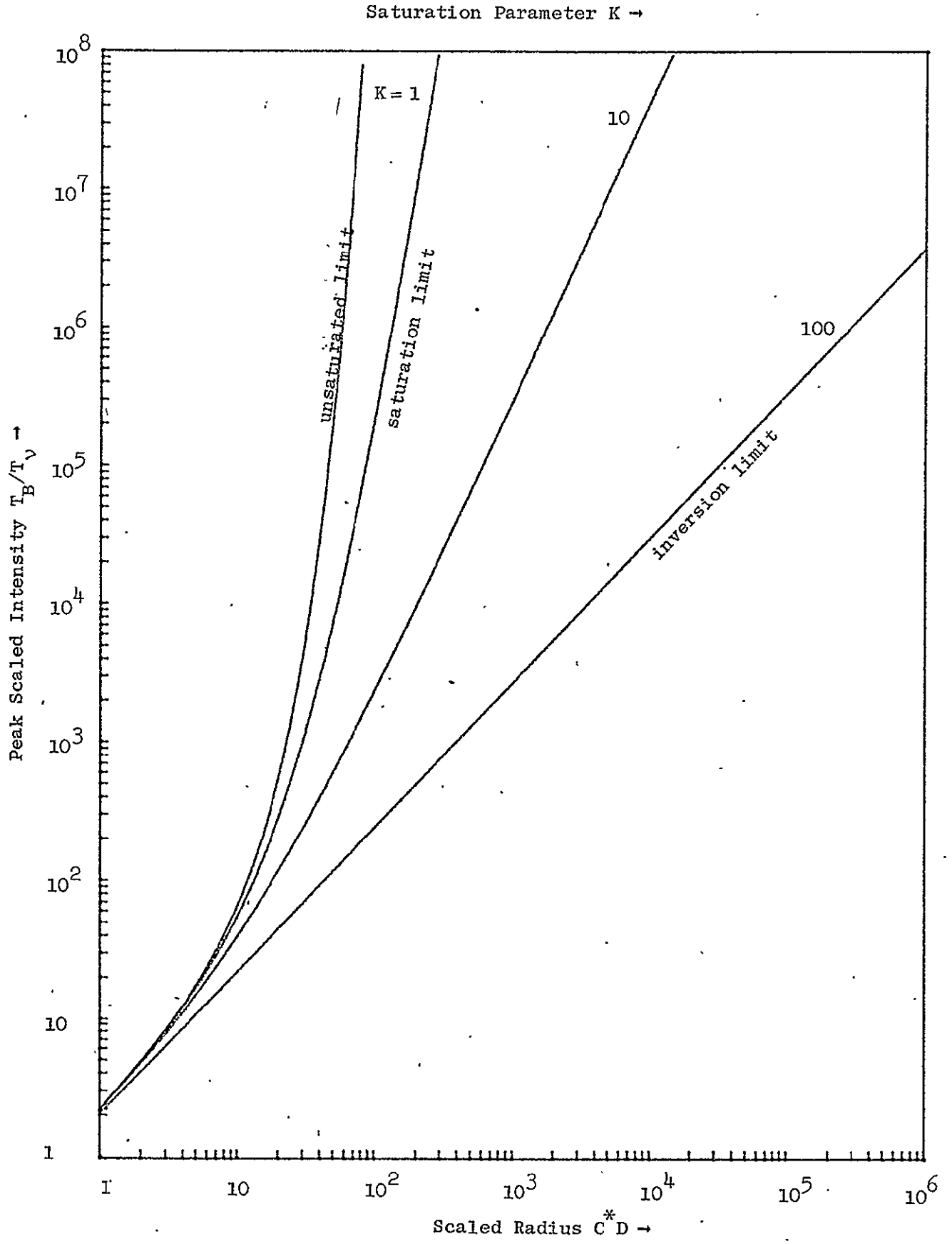

Figure 10a. Peak Intensity for Population Fraction (1-r) = 0.1

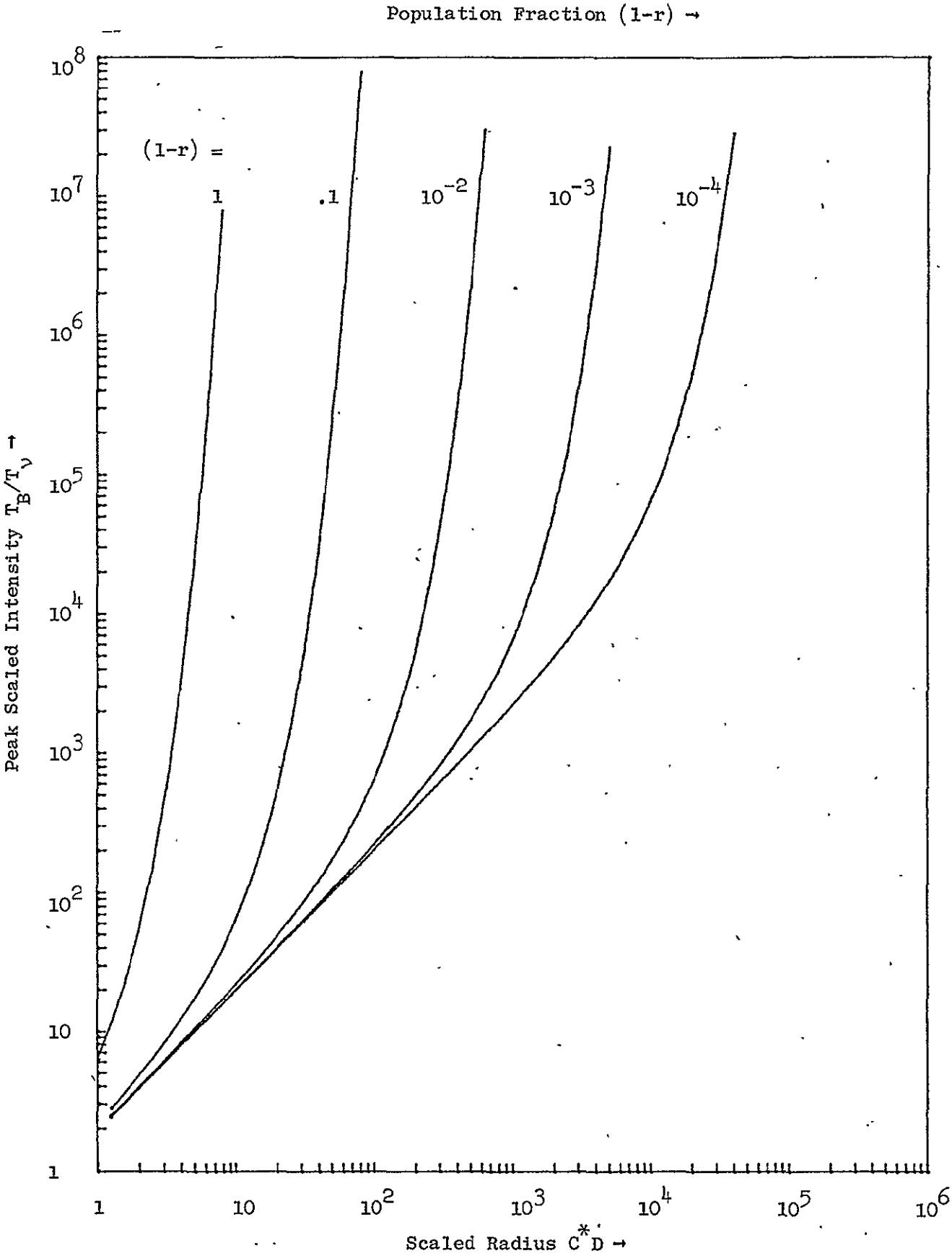

Figure 11. Unsaturated State Peak Intensity

CHAPTER V

POPULATION OF THE OH ENERGY LEVELS

A. Introduction

In the decade since the discovery of the OH emission a number of mechanisms have been put forward to explain the maser pumping. The four mechanisms that will be discussed here cover the major exciting pathways available in the OH molecule, though the actual pumping which occurs in astrophysical masers may be a complicated combination of any or all of these mechanisms. The first OH emission discovered was associated with the ionized gas near hot stars. This association suggested that ultraviolet radiation could be the exciting power for the masers through resonant lines near 3080 Å. Litvak et al. (1966) and Perkins et al. (1966) proposed a UV absorption mechanism which required selective absorption in the UV lines to provide the microwave inversion. Infrared astronomers have also associated some OH sources with infrared stars, which can pump the OH through the 2.8 and 1.4 micron vibrational bands, or for lower temperature infrared clouds the pumping could be through the 100 micron rotational levels. Studies of these pathways have been presented by Litvak (1968, Litvak et al. (1969), and again by Litvak (1973) and by Shklovsky (1967). Townes (1970) and others have also proposed that the OH emission could be pumped by the collisional action of atoms or molecules with the OH. Most of the other mechanisms proposed can be lumped under the title of chemical pumping where the OH is created in an excited state by the formation process. This later is so dependent on the assumptions of the formation mechanism that any desired population distribution could be produced with careful assumptions, and is

hence too vague to provide further insight. We have made numerical calculations of the populations produced by the other mechanisms and will present them here. Our desire is to examine the far infrared emission which would result from the pumping, and consider the microwave emission only as it can help determine the physical conditions of the maser region. This allows us to ignore the hyperfine structure of the OH molecule without significant loss. The energy structure of the ground vibrational state is shown in figure 20 for reference, with the dipole allowed transitions and their wavelengths in microns.

In the derivations of Chapters II and III the interactions between the transfer equation and the population equations have all been folded into a modified transfer equation, whose solution was then presented in Chapters III and IV.. The population solution of the emission problem then becomes an eigenvalue solution of the matrix of transfer coefficients and can be written as the system of equations:

$$g_i \times \frac{dn_i}{dt} = \sum_j W_{ji} n_j - n_i \sum_j W_{ij} = 0 \qquad \text{(V-A-1)}$$

where

$$W_{ij} = A_{ij} + B_{ij} I + C_{ij}$$

and the n_i are the normalized populations corrected for degeneracy. The solution of the above matrix will then give the population fraction as n_i/g_i since this is the value of the population which will be needed in the transfer equation.

B. Ultraviolet Pumping

The ultraviolet pumping mechanism proposed by Perkins et al. (1966) and refined by Litvak et al. (1966) involves the absorption of 3080 Å radiation through the transitions from the ground state lambda doublet of the OH molecule to the six lowest rotational levels of the first excited electronic state of OH, followed by spontaneous decay to the various rotational and vibrational levels of the V = 0,1, and 2 ground electronic state. The exciting source is assumed to be an O5 type star at a distance of 2 light years. The only radiation absorbed is through the six transitions leaving the lowest Lambda doublet although transitions involving the other rotational levels of the ground electronic state are nearly the same wavelength. This selective action could occur by resonance with some line structure in the O5 star, or through the filtering action of an intervening gas such as hydrogen.

Figure 12 shows the populations of the OH states which results from this mechanism for various distances of the exciting source. The ground state lambda doublet is not inverted, so this simple mechanism cannot provide the observed microwave emission. However, the lambda doublets of two excited $^2\Pi_{1/2}$ states are inverted and could lead to detectable maser emission if the exciting source were closer than two light years. If the exciting source were very close, the 12-10, 11-9, 8-4, and 7-3 inversions could lead to observable infrared emission at wavelengths near 100 microns. If the exciting source were farther away the OH cloud would have to be extremely large to give observable emission. Unless the exciting source were very restricted in its intensity outside the 3080 Å absorption band the OH would probably be disassociated by the star at distances closer than a few tenths of a light year.

As the ultraviolet radiation propagates through the OH cloud, absorption will alter the intensity distribution in the six UV lines. Litvak et al. (1966) showed that this selective absorption leads to a limited region of population inversion in the observed ground state lambda doublet. Figure 13 shows this effect for the UV mechanism with the O5 star at a distance of two light years, with the optical depth scaled to the strongest UV absorption line. At this distance the higher rotational levels have small population fractions, but the microwave inversion of the excited lambda doublets is maintained or increased over a greater distance than the ground state doublet. Despite the low populations it may be possible to detect this emission if the region is large enough. This microwave inversion would also not disappear if the exciting source were much closer, and in that case there could be detectable infrared emission.

C. Collisional Pumping

In equation (V-A-1) a term C_{ij} has been included for the collisional transfer rate. Dipole collisions between OH and the common charged particles of the interstellar gas have been studied by Barrett and Lilley (1957) and further by Rogers and Barrett (1968) and Goss and Field (1968). However, the regions of OH emission are replete with complicated molecules, and charged particles can be uncommon members of the OH medium.

Townes (1970) and Goldsmith (1972) suggested that molecular collisions occurring in the interstellar medium could lead to excitation of maser transitions in ammonia and carbon monoxide, and possibly in OH. Townes and Gwinn (see Townes 1970) suggested that if the colliding

particle is a diatomic hydrogen molecule the OH could be excited in a preferred rotational state which would lead to the microwave inversion. Goldsmith found that in the case of CO the collisions with charged particles, although more frequent than molecular collisions, would produce only a thermal population distribution because the collisionally induced transitions were restricted to dipole allowed changes. Even the quadropole transitions produced a nearly thermal population distribution. However, as Goss and Field (1968) and others have shown, there are no selection rules for molecule-molecule collisions because the interaction forces are very short range. Goldsmith then applied constant deexcitation cross sections with exciting cross sections given by:

$$g_i \sigma_{ij} = g_i \sigma_{ji} \exp \frac{-\Delta E}{RT} \quad , \quad j > i \qquad \text{(V-C-1)}$$

to find population inversions in the CO molecule. Figures 14 and 15 show the effects of this pumping scheme on the OH energy structure, using a constant de-exciting cross section of 10^{-15} cm^2, with the reverse exciting collisions using the above cross section. There are no selection rules in this scheme, and for densities below 10^8 H_2 molecules per cm^3 the spontaneous transition rates of the infrared lines exceeds the collisional rates. The action of this mechanism is then to excite the OH to all possible levels, the variation in rates among the levels being only the Boltzmann factor in (V-C-1), with the excited molecules returning to the lower states by spontaneous emission. Since the exciting and the de-exciting rates are not symmetrical the OH population distribution can take on anomalous inversions just as it would if the OH were formed in the excited states. For densities below a few H_2 particles

per cubic centimeter the collision rates are not sufficient to excite the OH molecule. As the kinetic temperature increases the exciting and de-exciting collision rates becomes more nearly equal, and the population distribution takes on a thermal character. For the kinetic temperature of 100°K only the 18 centimeter microwave line is inverted sufficiently to produce detcctable emission unless the H_2 density exceeds 10^6 particles per cc. In figures 14 and 15 the populations of the odd numbered states except 1 are identical to the populations of their even numbered doublet partner, so only the even numbers are given. Above 10^7 cm^{-3} densities the infrared lines from levels 12 to 10 and 8 to 4 are sufficiently inverted to produce maser radiation. At a kinetic temperature of 1200°K the collisional rate across the lambda doublet is nearly equal in both direction, and the microwave inversion is disappearing. Between 10^6 and 10^8 cm^{-3} the inversion of the 96.4 micron line between levels 8 and 4 disappears. The 12 to 10 inversion is significant at densities above 10^5 cm^{-3}. The higher vibrational and electronic states have been included in this model, but the energy differences are so large that the collisional pumping from the $v = 0$ levels is negligible, and the populations are near zero.

D. UV and Collisional Pumping Combined

Figure 16 shows the combined effects of the UV pumping scheme (without absorption) with the exciting star at two light years, with the molecular collision scheme. Because the UV pumping at this distance is so weak, the collision effects dominate the excited state populations. In fact, the collisions can still produce the microwave inversion if the density of H_2 particles exceeds 10^3 cm^{-3}. Because of the weakness

of the UV pumping the infrared emission is the same as in the collisional case.

E. Near Infrared Pumping

The vibrational bands of OH at 1.4 and 2.8 microns can be excited and produce maser pumping by resonance absorption of infrared radiation. A number of the other molecules in the interstellar medium have emission in the range of these transitions, and for temperatures of a few thousand degrees the black body peak occurs between the two wavelengths. If the OH is near a star or protostar of this temperature, it would be possible for the vibrational bands to be excited. If there is a significant amount of dust in the vicinity, the longer far infrared portion of the spectrum could be strongly absorbed, so that only the vibrational transitions are excited. If the radiation incident on the OH cloud is of equal intensity in the 1.4 and 2.8 micron bands and nearly zero at other wavelengths the population will have the distribution shown in figure 17. The temperature of a black body with equal intensities at 1.4 and 2.8 microns is 2650°K, so this is the listed exciting temperature, although the excitation is more correctly a pair of equal delta functions at 1.4 and 2.8 microns with a line width equal to the vibrational bandwidth. The intensity of the pumping radiation is the black body intensity at 2650°K multiplied by the fraction of the sky that the OH cloud sees filled with the pump source. This is the equivalent to the distance function of the UV pumping case, but here it is difficult to estimate the physical size of the infrared source. For vibrational excitation the parity selection is fixed for all the transitions, and there is no parity assymmetry which can produce a lambda

doublet inversion. Litvak and others have proposed that the trapping of the far infrared radiation by resonant scattering in the OH region as the mechanism for producing the microwave inversion. Selective amplification of the magnetic hyperfine structure caused by the presence of a magnetic field, or a plasma propagation effect such as parametric down conversion discussed by Litvak (1970) are needed to produce the microwave inversion with the correct polarization properties.

The near infrared pumping mechanism does produce some very interesting results for the far infrared emission pattern. Figure 17 shows the population solution, with only the odd numbered levels shown, as the even numbered levels have identical populations to their doublet counterparts; the dashed lines are the populations of the rotational levels in the first vibrational state. If the pump source is a large part of the sky at the OH region, the lowest $^2\Pi_{1/2}$ level has a larger population than the ground state, and a very strong infrared maser emission at 82 microns is expected. A sky fraction below 10^{-4} for the pump source does not produce any infrared inversion, and as the intensity increases the infrared inversions appear and grow more intense. When the pumping source fills half of the sky at the OH cloud all the infrared transitions connecting the $^2\Pi_{3/2}$ and $^2\Pi_{1/2}$ states have inverted populations. More intense pumping can lead to population inversions in some of the 2.8 micron transitions connecting rotational levels of the $v = 1$ and the $v = 0$ states.

F. Far Infrared Pumping

The assumption in case E that the far infrared radiation from the pumping source is negligible is not easily justified. Unless the exciting radiation is a resonant line from some other emission source, the radiation in the 100 micron region of low temperature black bodies can be important in the OH pumping. Litvak and others have proposed that the trapping of far infrared radiation in the OH cloud or from a nearby protostar is important in producing the microwave emission from some of the Class II OH sources. This section deals with a simple far infrared model to show that for some conditions the FIR radiation is indeed important, at least to the production of infrared masers.

The pumping proposed here involves the absorption of black body radiation from low temperature objects in the vicinity of the OH cloud as a function of the sky fraction they cover. All the infrared transitions of the three lowest vibrational states and the vibrational transitions among these three states. For temperatures of a few hundred degrees the black body peak, and hence the greatest transition rate is near the 100 micron wavelengths of the rotational transitions. The population distribution among the low rotational states should be nearly thermal with little infrared inversion possible. The only source of inversion pumping for these very low temperatures is the dilution of the pumping radiation by the background space. If the pump only occupies a small fraction of the sky however the intensity will be too weak to provide detectable emission lines. Since the absorption of black body radiation has no parity selection rules there will be no microwave inversions, with the populations of the doublet pairs identical. If the temperature

of the black body pump is in the range of a few thousand degrees, the vibrational transitions at 1.4 and 2.8 microns are strongly excited, as in the near infrared pumping model of Section E.

Figure 18 shows the population distribution which results from the absorption of 500°K black body radiation. In order to see the infrared emission the OH cloud must be nearly enclosed by the pumping source, and then only weak inversions are produced in the 5 to 1 and higher transitions. In order to be detectable the infrared emission resulting from this pump will have to come from a very large OH cloud. Figure 19 shows the population distribution produced by a 2000°K pumping source. Pumping to the vibrational levels and the ensuring decay to the excited rotational levels affects the ground state population even for small sky fractions allowing the 5 to 1 transition to become inverted at a sky fraction of 0.1. Sky fractions above one percent produce weak inversions in the 11-9 and 15-13 lines, and larger pumping rates produces infrared inversion in all the $\Delta J = +1$ transitions, and the 50 micron band of $\Delta J = 0$ transitions are nearly inverted when the sky in ninety percent filled with the pumping source. For high pumping rates the populations of the $v = 1$ states begins to become significant. The population distribution of figure 19 is not greatly different from the near infrared pumping model of figure 17 for sky fractions above 10^{-2} if the difference in temperature is considered.

G. Summary

The four pumping mechanisms discussed in this chapter cover the most likely exciting pathways available to the OH molecule which do not require the creation of OH in an excited state. Under two of them the

C-2

microwave main line inversion is easily created, and under all of them there are some infrared line inversions. A more detailed analysis of the energy and transfer structure of the OH molecule which includes the hyperfine structure is necessary to model the class II satellite line emission, though efforts have been made in this direction in the papers mentioned by Litvak and others. The ease with which the collisional pumping model produced the microwave inversion implies that collisions can indeed be important in the emission of the interstellar molecules, a view that has long been held by Townes and others. The common occurrence of infrared inversions means that infrared observations can make significant contributions to the study of the interstellar molecules. Current observing capabilities in the infrared region around 100 microns are limited in sensitivity, and the next chapter will consider the possibility of detecting the infrared maser emission of the various pumping models.

Captions for Figures 12 through 20

Figure 12. The population fraction resulting from the UV pumping model including vibrational levels as a function of the intensity or distance of an O5 exciting star.

Figure 13. The population distribution of the UV pumping model including the effects of attenuation of the UV radiation by the OH, as a function of the optical depth in the $P_1(1)$ transition at 3080 Å.

Figure 14. The population distribution of the collisional pumping model with the kinetic temperature of the H_2 colliding particles at 100°K. The cross section of the collisions is assumed to be 10^{-15} cm^2.

Figure 15. The population distribution of the collisional pumping model for a kinetic temperature of 1200°K, which corresponds to the thermal line width of the microwave emission.

Figure 16. The population of the OH molecule with the combined action of UV pumping by an O5 star at a distance of 2 light years and collisional pumping at a kinetic temperature of 100°K.

Figure 17. The population effects of near infrared pumping, where the exciting radiation is confined to the 1.4 and 2.8 micron bands, with the ratio between the two band strengths corresponding to a temperature of 2650°K. The dashed lines are the populations of the first vibrational state. The intensity of the pumping radiation is given by the black body intensity at 2650°K times the fraction of the sky that the pump fills as seen by the OH cloud.

Figure 18. The population distribution of the OH molecule with pumping by a 500°K black body filling a fraction of the sky. Only the odd numbered levels are shown, with their even numbered counterparts having the same population.

Figure 19.- The population distribution for black body pumping at $2000^{o}K$ as a function of the dilution factor.

Figure 20. The energy level structure of the lowest vibrational state of the OH molecule showing the allowed transitions and their wavelengths, and the numbering scheme used in figures 12 through 19.

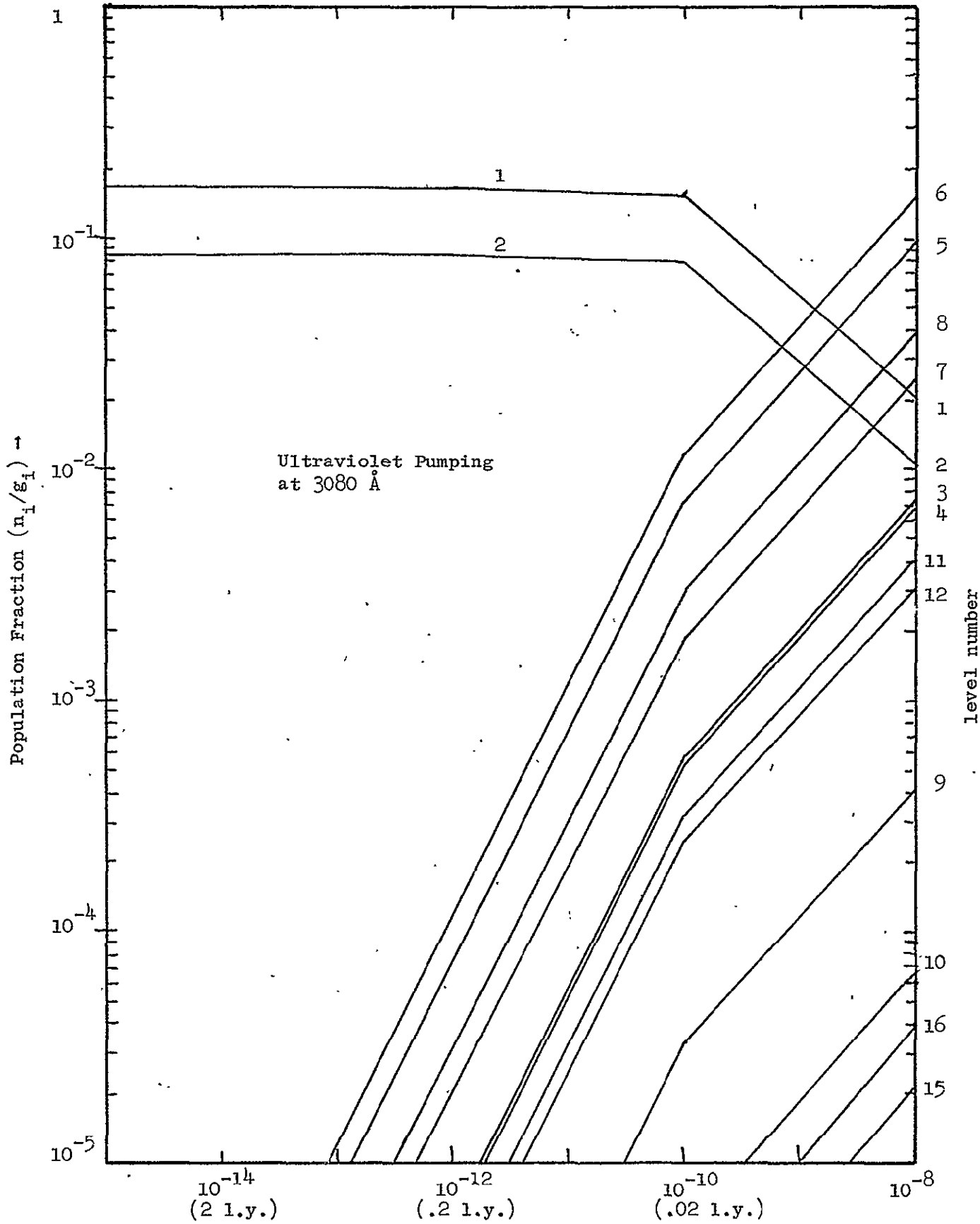
Ultraviolet Pumping
at 3080 Å
Population Fraction (n_i/g_i)
level number
1
10^{-1}
10^{-2}
10^{-3}
10^{-4}
10^{-5}
10^{-14} (2 l.y.)
10^{-12} (.2 l.y.)
10^{-10} (.02 l.y.)
10^{-8}
Ultraviolet Pumping Flux

Figure 12

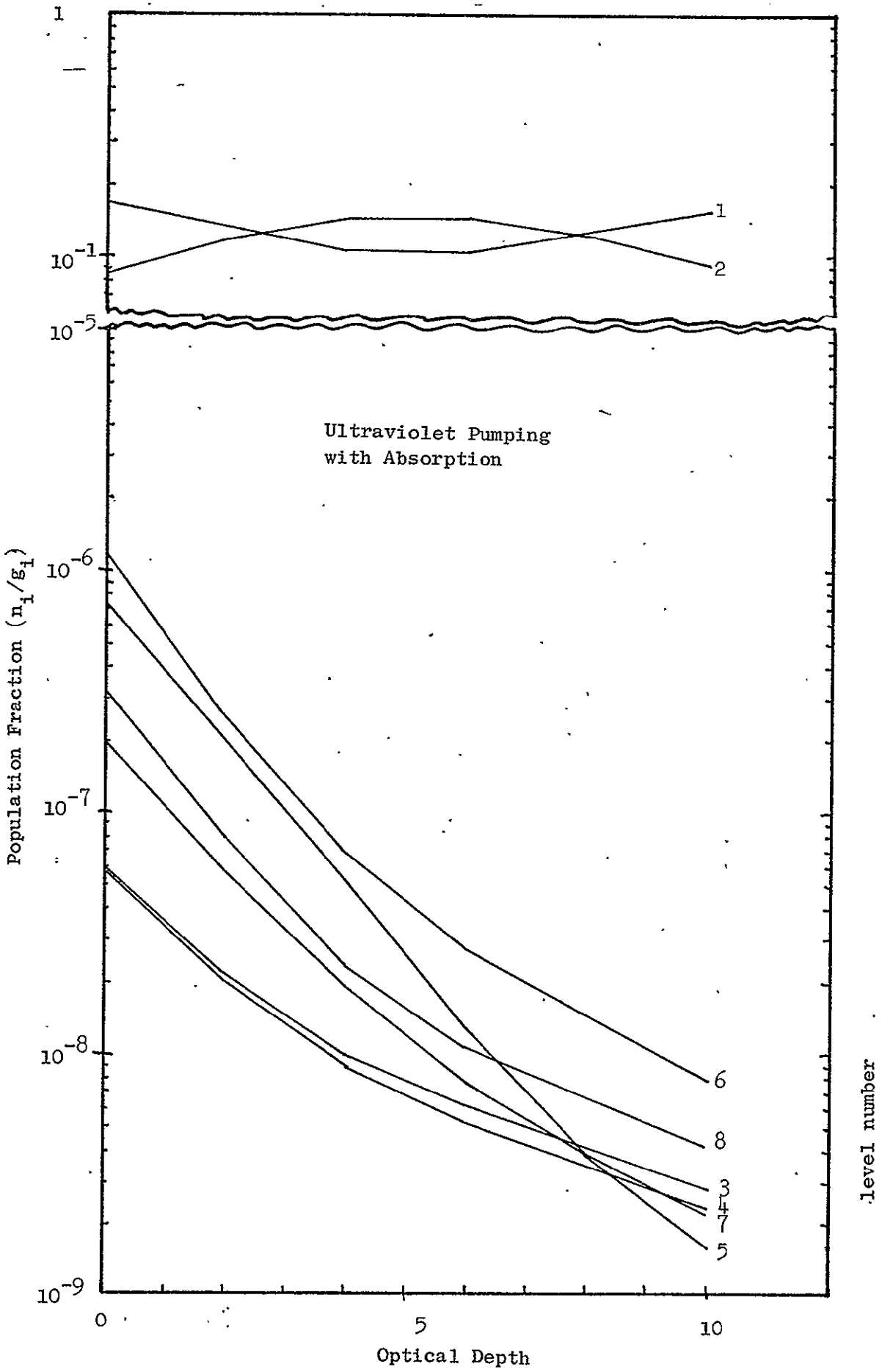
1
10^{-1}
10^{-5}
10^{-6}
10^{-7}
10^{-8}
10^{-9}
Ultraviolet Pumping
with Absorption
Population Fraction (n_i/g_i)
1
2
6
8
3
4
7
5
level number
0
5
10
Optical Depth

Figure 13

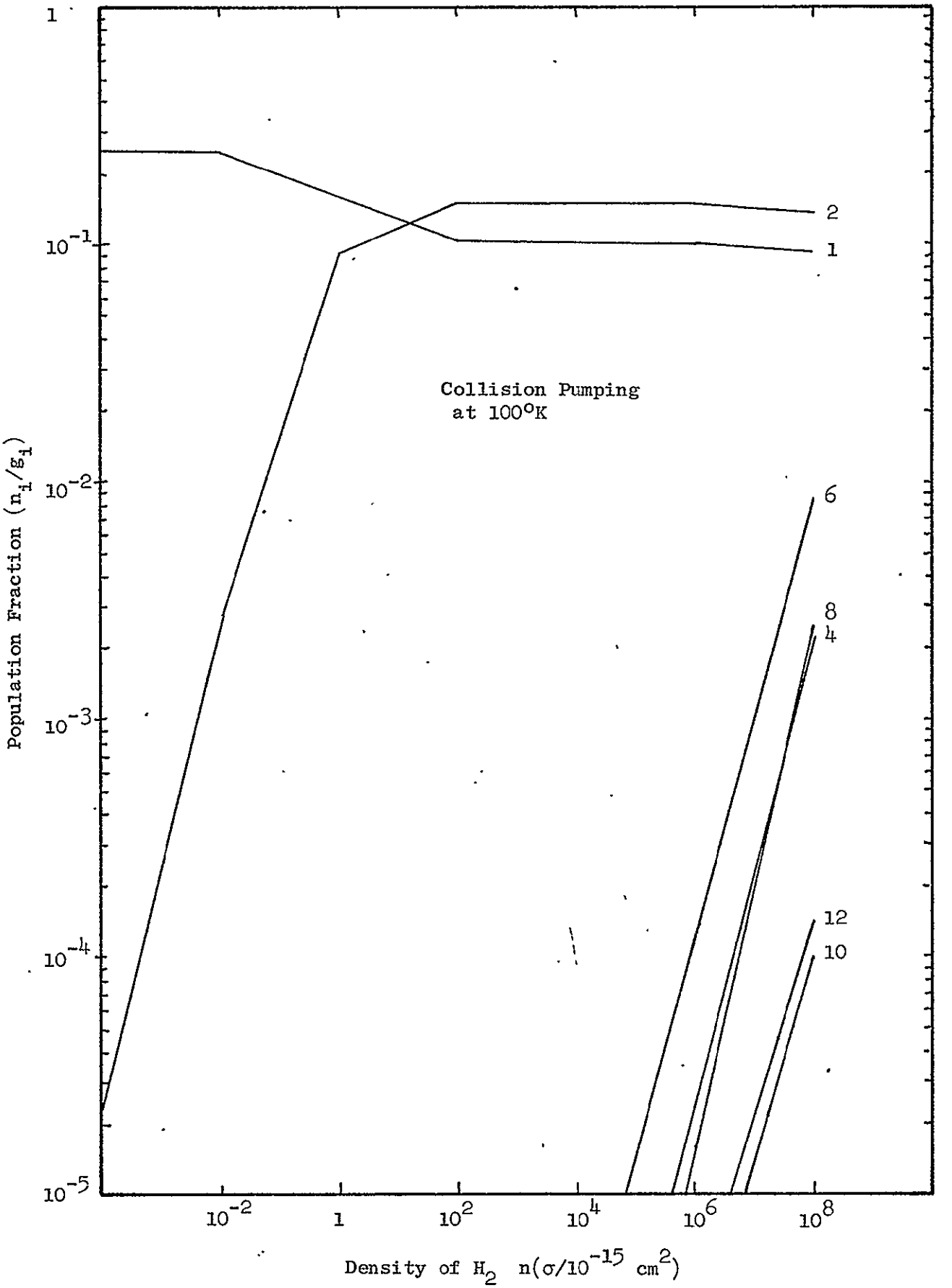
Collision Pumping
at 100°K
Population Fraction (n_i/g_i)
Density of H_2 $n(\sigma/10^{-15}$ cm^2)
level number
1
10^{-1}
10^{-2}
10^{-3}
10^{-4}
10^{-5}
10^{-2}
1
10^{2}
10^{4}
10^{6}
10^{8}
2
1
6
8
4
12
10

Figure 14

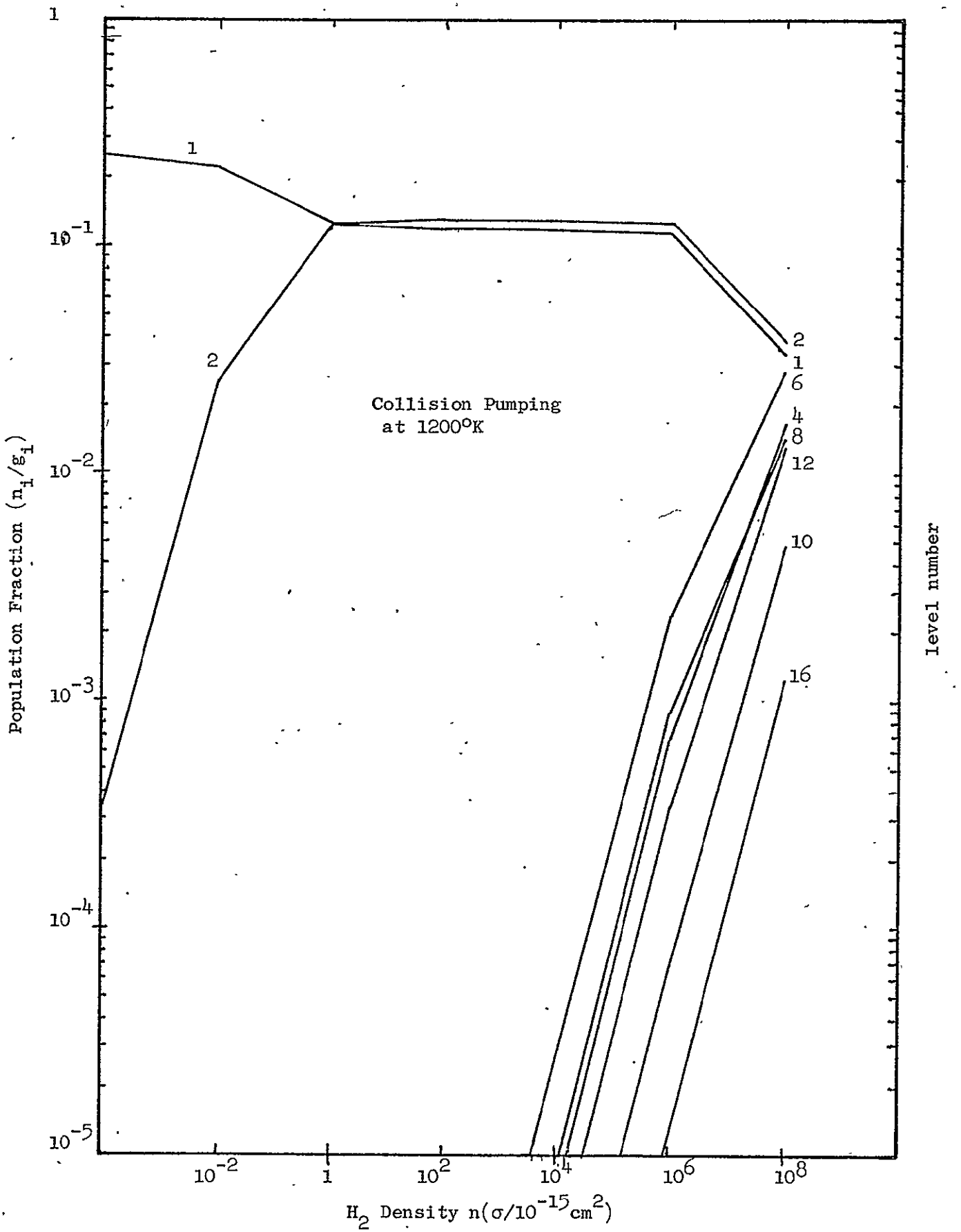
Collision Pumping
at 1200°K
Population Fraction (n_1/g_1)
H_2 Density $n(\sigma/10^{-15}cm^2)$
level number
1
10^{-1}
10^{-2}
10^{-3}
10^{-4}
10^{-5}
10^{-2}
1
10^2
10^4
10^6
10^8
1
2
2
1
6
4
8
12
10
16

Figure 15

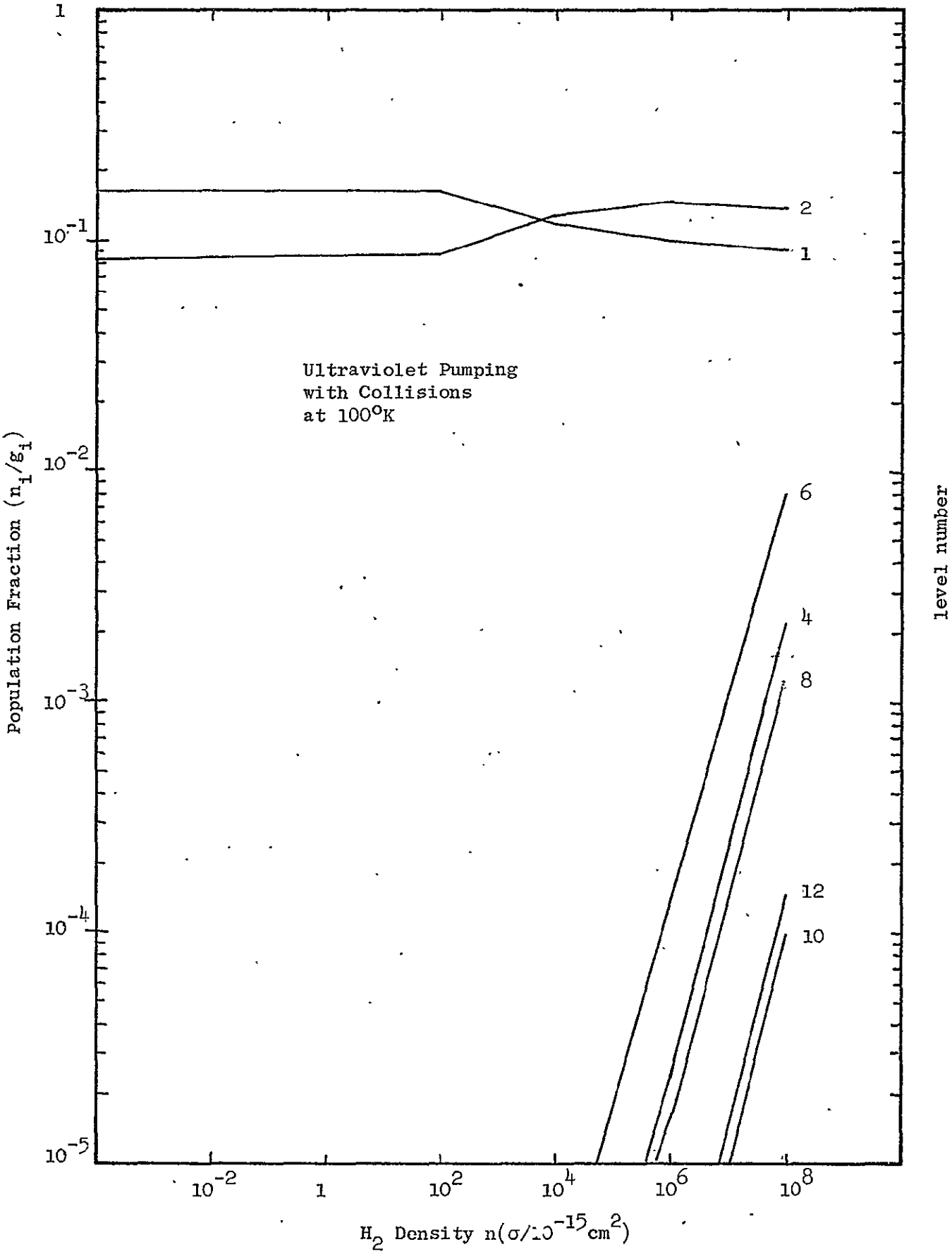
Ultraviolet Pumping
with Collisions
at 100°K
Population Fraction (n_i/g_i)
level number
H_2 Density $n(\sigma/10^{-15}cm^2)$
1
10^{-1}
10^{-2}
10^{-3}
10^{-4}
10^{-5}
10^{-2}
1
10^{2}
10^{4}
10^{6}
10^{8}
2
1
6
4
8
12
10

Figure 16

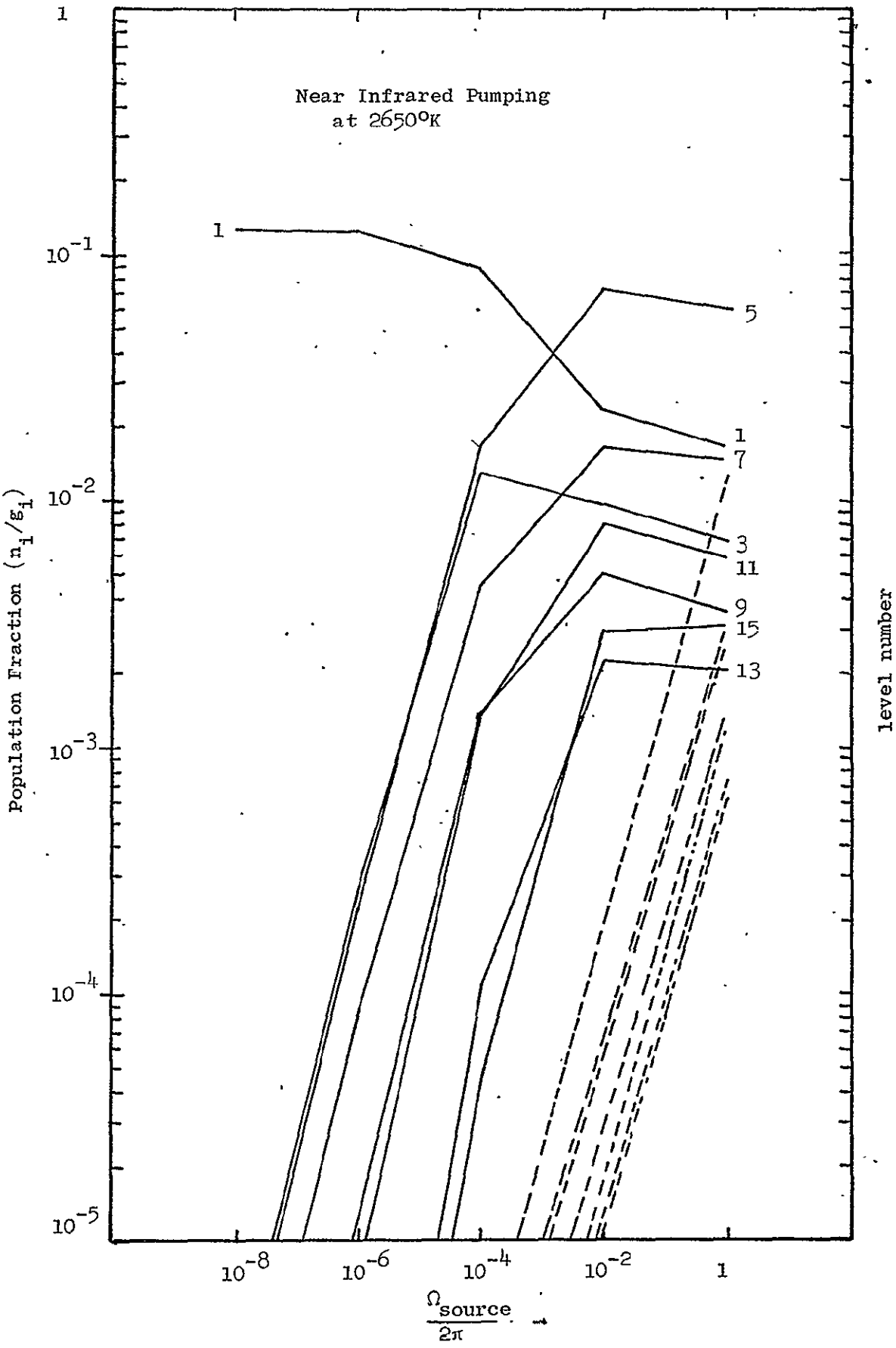
Near Infrared Pumping
at 2650°K
1
10^{-1}
10^{-2}
10^{-3}
10^{-4}
10^{-5}
Population Fraction (n_i/g_i)
5
1
7
3
11
9
15
13
level number
10^{-8}
10^{-6}
10^{-4}
10^{-2}
1
$\frac{\Omega_{source}}{2\pi}$ →

Figure 17

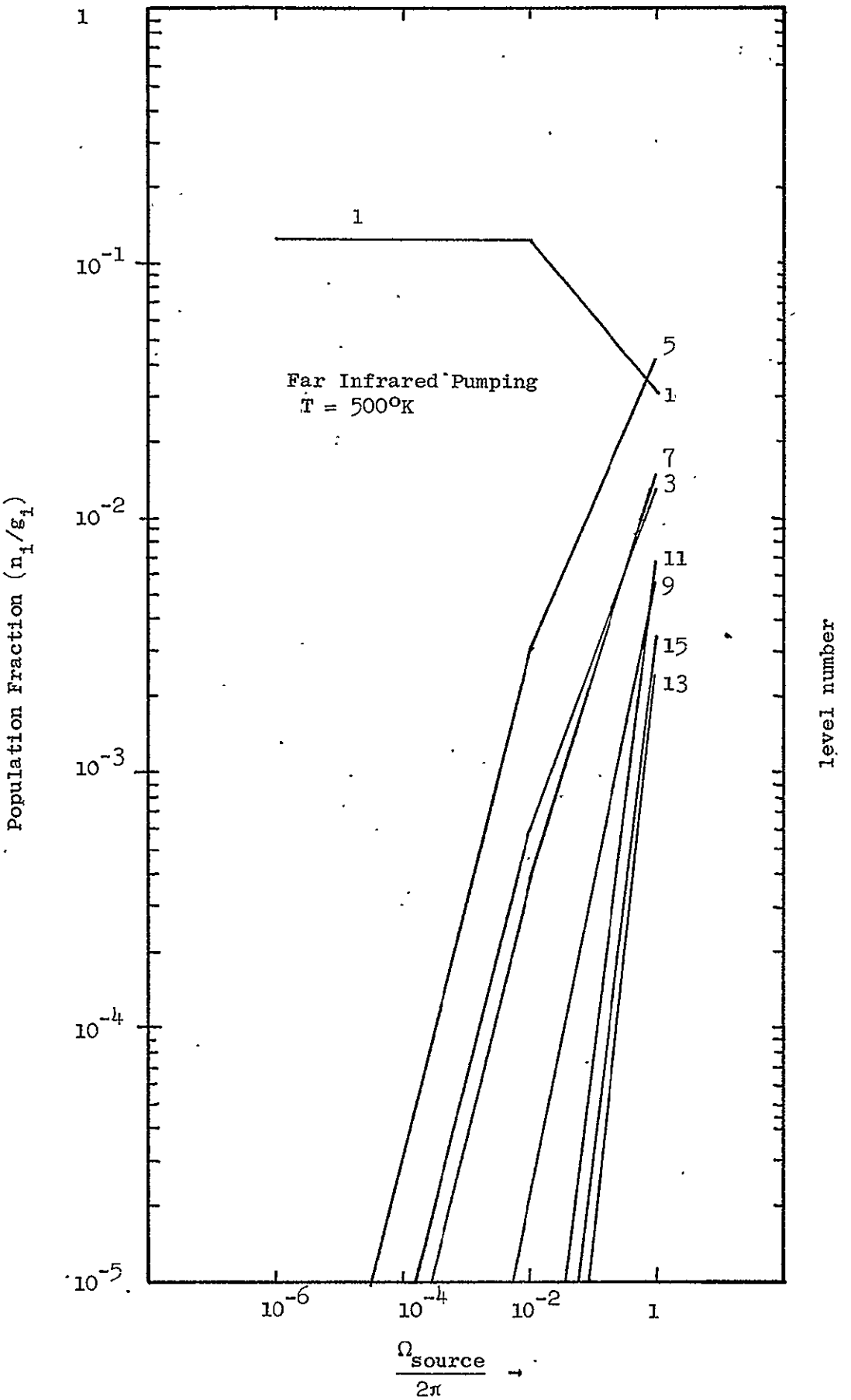
1
10^{-1}
10^{-2}
10^{-3}
10^{-4}
10^{-5}
Population Fraction (n_1/g_1)
Far Infrared Pumping
T = 500°K
1
5
1
7
3
11
9
15
13
level number
10^{-6}
10^{-4}
10^{-2}
1
$\frac{\Omega_{source}}{2\pi}$ →

Figure 18

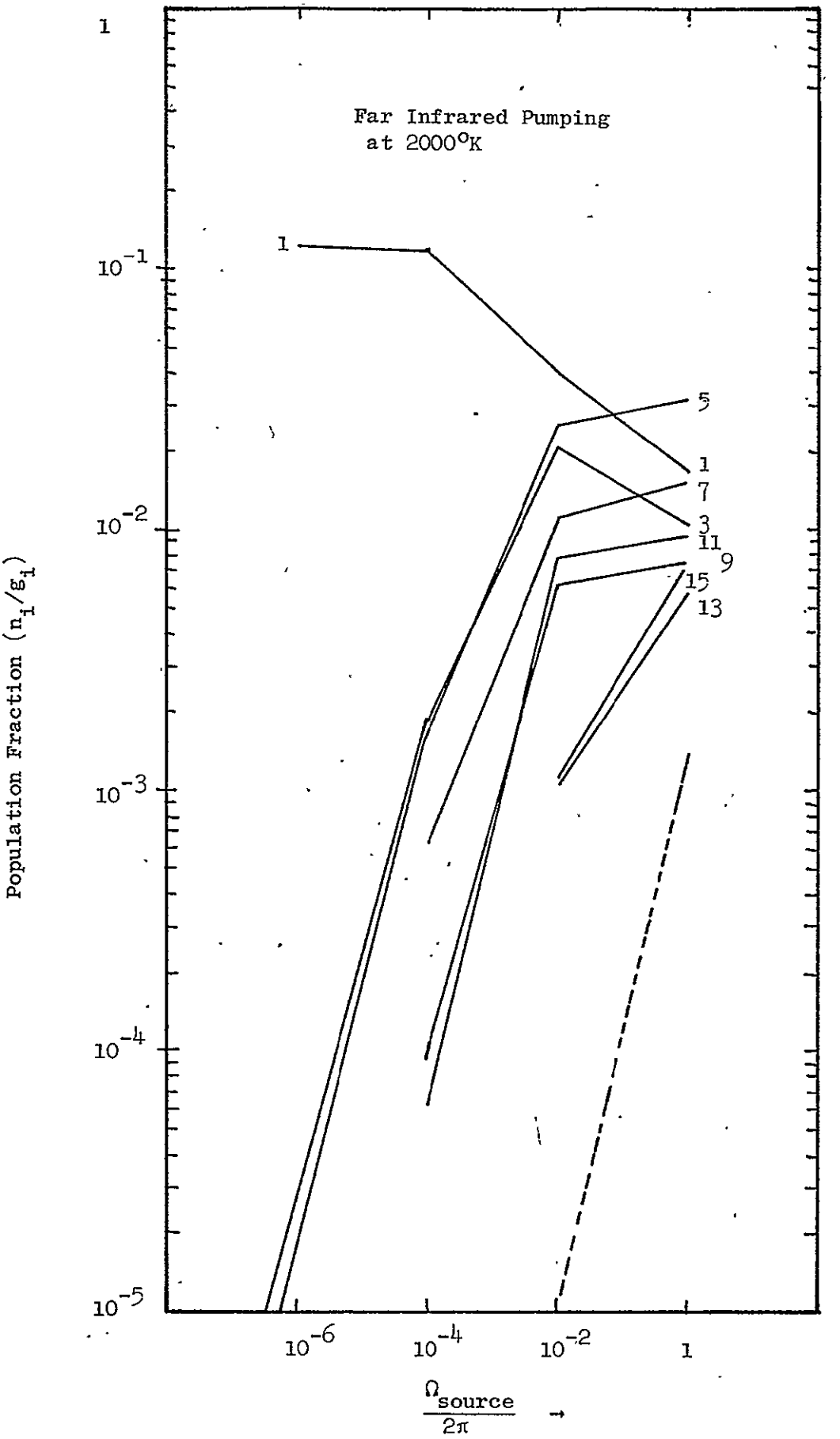
Far Infrared Pumping
at 2000°K
1
10^{-1}
10^{-2}
10^{-3}
10^{-4}
10^{-5}
Population Fraction (n_i/g_i)
1
5
1
7
3
11
9
15
13
level number
10^{-6}
10^{-4}
10^{-2}
1
$\frac{\Omega_{source}}{2\pi}$ →

Figure 19

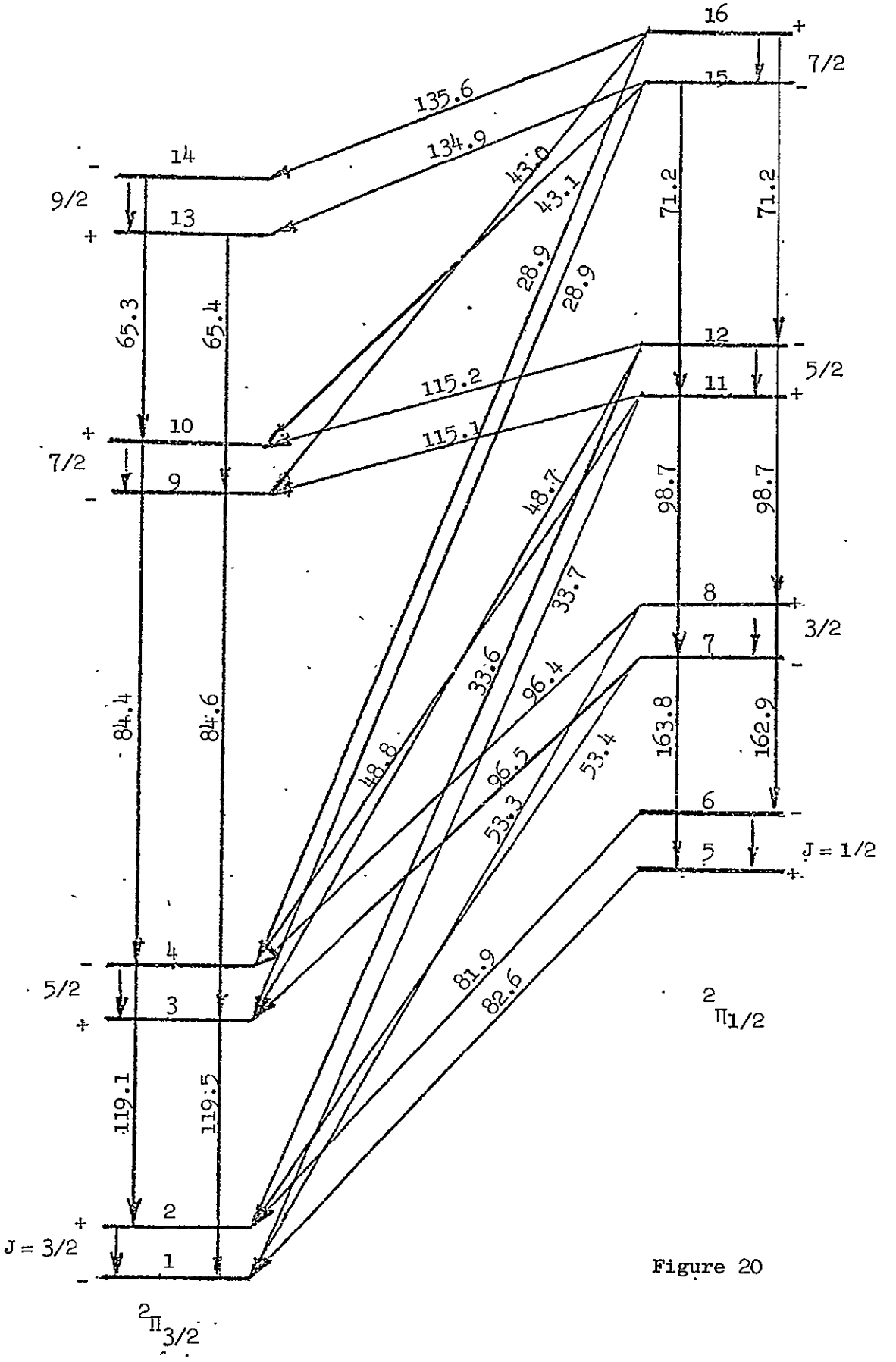
16
+
7/2
15
-
135.6
134.9
14
-
9/2
13
+
43.0
43.1
71.2
71.2
28.9
28.9
65.3
65.4
12
-
5/2
11
+
115.2
115.1
10
+
7/2
9
-
48.7
98.7
98.7
8
+
3/2
7
-
33.7
33.6
96.4
96.5
53.3
53.4
84.4
84.6
48.8
163.8
162.9
6
-
5
+
J = 1/2
4
-
5/2
3
+
81.9
82.6
2
Π1/2
119.1
119.5
2
+
J = 3/2
1
-
2
Π3/2

Figure 20

CHAPTER VI

THE INFRARED INTENSITIES OF OH MASERS

A. Introduction

The discovery of the OH emission in 1965 stimulated a steady stream of theoretical discussions which have attempted to explain some or all of the important characteristics of the OH maser emission. The problem of polarization of the OH emission has yielded least to the efforts in part because the polarization is a characteristic of the propagation of the emission as it passes through the cloud and is dependent on the pumping mechanism of the OH. Previous chapters of this work have analyzed several of the important pumping mechanisms available to the OH in interstellar space and along with the papers published by other authors have shown that the observed OH intensities can be explained by one or another of these pumps. To make further headway against the problems of polarization and observed size, and of the conditions in the OH regions, a determination of the active pumping mechanism for each emission source must be made. The results of the pumping analysis of Chapter V indicates that population inversions can occur in the infrared transitions of the OH molecule in different proportions depending on the active pumping mechanism involved. This implies that successful observation of the infrared line emission from the OH sources can aid in determining the pumping mechanism and physical conditions of the region.

Using the model of the maser emission in spherical regions presented in Chapters III and IV we can describe the conditions of the emitting region as derived from the observed microwave intensities under various pumping mechanisms, and apply these conditions to the prediction of the

infrared line emission. As shown in Chapter V a pumping mechanism which allows parity effects, such as the UV pump or one of the collisional models, and which produces a ground state population inversion also produces population inversion for some infrared lines. Of course mechanisms which require propagation effects to produce the microwave inversion can also have infrared inversion, but we cannot use the microwave observations to analyze the conditions of the OH regions in these cases using our simple transfer model. For these pumping mechanisms a set of physical conditions consistent with the observed emission can be assumed in order to estimate the resulting infrared emission. Section D will then consider the detectability limit of current and projected infrared instruments and the limits this sets on the possible OH emission.

B. Characteristics of OH Emitters

The complicated nature of the OH emission has been discussed in Chapter I; here we will mention the properties of the emission in the sources W3 and Orion OH which are appropriate to the models of the maser amplification and pumping mechanism discussed in Chapters III and IV.

The W3 region of OH emission is one of the most heavily studied and complicated of the microwave OH emitters. W3 is in a HII region, which is maintained by one or more stars of spectral class O. Infrared observations have also revealed significant near and far infrared emission similar to hot dust and IR stars in the vicinity of the OH microwave sources, and a number of other complex molecules have been detected in the region. The physical sizes observed may only be vaguely related to the actual dimensions of the OH emitters, but they indicate a number

of small regions with diameters between 10 and a few hundred astronomical units (A.U.) scattered over a region of about 2000 A.U. The lines observed in emission are at frequencies of 1665 and 1667 MHz, with line widths of 5 to 15 kHz. The effective brightness temperatures, given by:

$$T_B = \frac{I\lambda^2}{8\pi k} \times \frac{4\pi}{\Omega_{source}} .$$

have steadily increased from 10^5 °K to the presently accepted values between 10^{11} and 10^{13} degrees as the resolution of long baseline interferometry has lowered the observed size to 10^{-8} to 10^{-9} sterradians. Other observations of OH absorption clouds indicated that the OH concentration is between 1 and 10^3 cm^{-3} and the densities of other molecules and atoms less than 10^{10} cm^{-3}.

The OH source in Orion is located near the trapezium stars, an area generally associated with star formation. As in W3 there is significant observed infrared emission from a large region surrounding the OH source and an infrared star of about 2000°K nearby. The optical obscuration in the region has been estimated at 20 to 100 magnitudes due primarily to a large amount of dust and cool gas. The physical size observed is less than 2×10^{14} cm, and the linewidth at 1665 and 1667 MHz is about 2 kHz.

C. The Infrared Emission of the Orion and W3 OH Sources

For the ultraviolet and collisional pumping models discussed in Chapter V there is significant inversion of the microwave energy levels which would lead to the maser amplification of the 1665 and 1667 MHz lines. In these models we will use the observational properties

mentioned above to estimate the physical characteristics of the OH clouds, and then use these estimates to calculate the expected infrared emission. The other pumping models do not show inversion in the lambda doublet which gives rise to the 1966 and 1667 MHz lines, but propagation effects such as resonant scattering infrared trapping, or parametric conversion could lead to the inversion of the satellite lines at 1612 and 1720 MHz, or possibly in the main lines. For pumping models which do not have intrinsic microwave inversion we will assume some characteristics consistent with the microwave observations.

In order to determine the intensity of a maser amplified line using the relations of Chapter III or the graphs of Chapter IV the following procedure will be used. Chapter II gives the spontaneous coefficient and the wavelength of the transition; these are combined with the physical size and the OH density to determine the scaled size from (IV-B-1), also using the population of the upper state of the maser emission. The numerical pumping model calculation which determined the population also gives the population ratio and the pumping rate Γ_a of the transition using (II-E-5), (II-E-8), and (II-E-11). The scaled size, population ratio, and the pumping rate are then used with figures 4, 5, or 6 to determine the state and degree of saturation in the spherical region. For partially saturated regions figures 8 and 9 permit the determination of the core size using the calculated parameters. Finally, figures 10 and 11 determine the scaled intensity. The peak brightness temperature so determined is averaged with (III-E-1), (III-E-2), or (III-E-3), and the intensity can be found with the line width and source size using (IV-D-1).

If the microwave intensity is to be used to determine the parameters of the OH cloud, the above procedure is reversed. The pumping model and the observations are used to determine the scaled intensity, which sets

range on the scaled size that depends on the saturation state. The pumping rate from the pump model is combined with the population ratio and this range of sizes to choose a consistent set of values for the size and saturation. Then the density and molecular characteristics are used to determine the physical size. The procedure can be iterated to verify the chosen values. The parameters so found are then used in the foregoing manner to find the infrared intensities.

In the transition matrix of the OH molecule the rates connecting the J levels of the $^2\Pi_{1/2}$ states are greater by factors of 10 or more than the rates connecting the $^2\Pi_{1/2}$ states to the $^2\Pi_{3/2}$ states. This leads to population inversions in the crossing transitions under most of the pumping models considered, with the wavelengths and molecular constants of:

wavelength	A_{ij}	$T_\nu = \frac{hc}{\lambda k}$
82.6 μ	3.5×10^{-2} sec^{-1}	174°K
96.4 μ	8.9×10^{-3} sec^{-1}	149°K
115.1 μ	3.1×10^{-3} sec^{-1}	125°K
134.9 μ	1.2×10^{-3} sec^{-1}	107°K
18 cm	7.11×10^{-11} sec^{-1}	0.08°K
6.3 cm	1.16×10^{-9} sec^{-1}	0.22°K

1. Ultraviolet Pumping

In order to produce the microwave inversion with ultraviolet pumping the selective absorption of the UV radiation propagating into the cloud must be considered. The population distribution with this

absorption included is not significantly different for the infrared lines than when absorption is not included. The microwave inversion occurs over a limited distance, while the infrared inversions are maintained over significantly larger distances. With the infrared populations which occur under pumping from 2 light years the increased size of their inversion regions is not of importance, since the emission will remain below detectable levels. If the exciting source is moved closer, to 1000 A.U., the populations of the infrared transitions are much larger, and the population of the 6.3 cm transition has increased to detectable levels. Of course at this close distance the OH dissociation rate could increase to a degree which would destroy all the OH emission. If this dissociation is tempered by a high formation rate, the entire emission complex of the W3 region can be explained by the selective absorption creating a shell of microwave inversion. Density variations or turbulence in the OH cloud surrounding the exciting star could then lead to the formation of numerous spots of microwave emission, as is observed. However, the inversion in the 6.3 cm line of the $^2\Pi_{1/2}$, J = 1/2 doublet could occur over the entire region. Since the population in this line is an order of magnitude below the 18 cm populations and the pumping rate in this level is lower, the 6.3 cm emission could be lower in intensity, as is observed. The large extent of the population inversion for the infrared transitions leads to significant emission intensities.

For UV pumping from 1000 A.U. the inversions, their populations, their population ratios, and their pumping rates [found by numerical solution of equations (II-E-1), (II-E-5), (II-E-8), and (II-E-11)], are

λ	n_u/n_{OH}	(1-r)	Γ_a/A
6.3 cm	4.0×10^{-2}	0.32	3×10^9
96.4 μ	1.0×10^{-2}	0.8	200
96.5 μ	6.7×10^{-3}	0.6	105
115.1 μ	1.02×10^{-3}	0.9	290
115.2 μ	8.8×10^{-4}	0.95	300

In the UV pumping scheme there are three sources to model; the Orion OH source, the W3 source, and the extended W3 source with the emission region ten times larger for the infrared lines and for the 6.3 cm line than for the 18 cm line. The scaled size, saturation state, and average brightness temperature using figures 4 and 5 to determine the state of saturation, (and figure 6 for the microwave lines, which are fully saturated), and figure 10 and 11 for the intensity. The set of results which consistently fits the 18 cm observations of the Orion OH source are:

λ	C^*D	State*	$\langle T_B \rangle ^\circ K$	$I_\nu (w/cm^2 Hz\ str)$
6.3 cm	380	FS, K = 50	10^{11}	7.0×10^{-14}
96.4 μm	8.0	PS, a/R = 0.2	2×10^5	5.9×10^{-14}
96.5 μm	7.2		9×10^4	2.7×10^{-14}

*F.S. = fully saturated, the extent indicated by the parameter K.
P.S. = partially saturated.
U.S. = unsaturated.

The parameters and conditions of the region as determined from the 18 cm observations are:

$$\text{MW observed size} = 3 \times 10^{14} \text{ cm}$$

$$\text{physical size} = 8 \times 10^{14} \text{ cm}$$

$$n_{OH} = 10^{2} \text{ cm}^{-3}$$

For the W3 OH source the expected results are:

λ	C^{*}_{D}	State	$\langle T_B \rangle {}^{\circ}K$	I_ν (w/cm^{2}Hz str)
6.3 cm	500	F.S. K = 9	10^{12}	7.0×10^{-13}
96.4 μm	19.0	P.S. a/R = 0.2	1.5×10^{6}	4.4×10^{-13}
96.5 μm	11.6	P.S. = 0.2	7×10^{5}	2.1×10^{-13}
115.1 μm	3.4	P.S. = 0.8	3×10^{4}	6.3×10^{-15}
115.2 μm	2.3	P.S. = 0.8	1×10^{4}	2.1×10^{-15}

where the 18 cm observations gave

$$\text{MW observed size} = 9 \times 10^{14} \text{ cm}$$

$$\text{physical size} = 1.8 \times 10^{15} \text{ cm}$$

$$n_{OH} = 10^{2} \text{ cm}^{-3}$$

For the extended W3 source the results which match the 18 cm and the 6.3 cm observations (the latter being used to estimate the size of the entire OH region while the former determines the smaller 18 cm inversion region) are:

λ in μm	C^*D	State	$\langle T_B \rangle$ °K	I_ν (w/cm^{2}Hz str)
96.4	16.3	P.S. a/R = .3	3.2×10^7	9.5×10^{-12}
96.5	10.1	P.S. = .3	1.0×10^7	3.0×10^{-12}
115.1	9.7	P.S. = .9	4×10^5	8.4×10^{-14}
115.2	9.3	P.S. = .9	3×10^5	6.3×10^{-14}

with the 6.3 cm and 18 cm observations giving:

$$n_{OH} = 70 \text{ cm}^{-3}$$

physical size = 7.3×10^{15} cm

MW observed size = 1.0×10^{15} cm

2. Collisional Pumping

The pumping of the OH molecule by low temperature kinetic collisions with hydrogen molecules is not a likely model for the OH emission in the Orion vicinity because of the large amounts of infrared radiation with a spectrum similar to a 700°K black body. Further, if the observed line widths are due to thermal broadening, then the implied thermal temperatures are rather higher than the 100 degree temperature of the cool collision model. Nevertheless, this model is able to produce the inversion needed for the microwave emission, but the infrared emission level is below the detectability limit, unless the density of colliding particles becomes greater than 10^8 cm^{-3}. For a density equal to that value, the population results are:

λ	n_u/n_{OH}	(1-r)	Γ_a/A
96 μ	2.45×10^{-3}	0.05	90
115 μ	1.5×10^{-4}	0.3	70

and the emission determined from figure 10 and 6a is:

λ	C^*D	State	$\langle T_B \rangle$	I_ν(w/cm^{2}Hz str)
96 μ	29	F.S. K = 1	4.7×10^4 ^oK	1.4×10^{-14}

If the collisional temperature is increased to the thermal line width, 1200^{o}K, the emission in the infrared states becomes more visible. The population inversion of the microwave transitions is reduced by the de-exciting action of the collisions, but for densities above 10^4 cm^{-3} the microwave intensity is still achievable, and at 10^8 the infrared line emission is significant. The lines and their population parameters at that density are:

λ	n_u	(1-r)	Γ_a/A
115 μ	1.3×10^{-2}	0.6	470
135 μ	1.2×10^{-3}	1.0	1100

Applying these results to the determination of the intensities and saturation states with figures 4 through 11, we find for the Orion OH source that:

λ	C^*D	State	$\langle T_B \rangle$	I_ν(w/cm^{2}Hz str)
115 μ	7.2	U.S.	6.7×10^6 ^oK	1.4×10^{-12}
134 μ	11.6	P.S. a/R = .8	4.2×10^5 ^oK	6.4×10^{-14}

where the 18 cm observations give

$$n_{OH} = 10^2 \text{ cm}^{-3}$$

$$\text{physical size} = 6.3 \times 10^{14} \text{ cm}$$

For the W3 emission:

λ	C^*D	State	$\langle T_B \rangle$	I_ν(w/cm^{2}Hz str)
115 μ	10.8	P.S. a/R = .6	7.3×10^6 °K	1.5×10^{-12}
134 μ	16.3	F.S. K = 1	1.2×10^5 °K	1.8×10^{-14}

using the 18 cm value of:

$$n_{OH} = 10^2 \text{ cm}^{-3}$$

$$\text{physical size} = 5.1 \times 10^{15} \text{ cm}$$

In this pumping scheme the extended W3 source is inappropriate because the estimated 6.3 cm inversion is very small.

3. Near Infrared Pumping

The unusual near infrared pumping scheme described in Chapter V easily produces infrared population inversions. However, since there are no parity effects included in this model, there is no microwave inversion to match the emission with. If we make some assumptions about the size and density of the OH sources, the infrared emission can be predicted. The assumed diameter of the region is chosen to be three times the observed microwave size, to account for reduction in size expected in the microwave emission. Since OH absorption studies of the W3 region show $n_{OH}/n_H \sim 10^{-6}$ and other work finds $n_H \sim 10^8$ cm^{-3} the value of $n_{OH} = 10^2$ cm^{-3} will be used for this pumping model. The same parameters will be used for the far infrared pumping model which also does not produce a microwave inversion. If the twin delta function pumping source has an effective brightness temperature of 2650°K the infrared

populations reach a maximum for a sky fraction of $\Omega_p/2\pi = 10^{-2}$. For further increases in the pumping intensity the populations of the vibrationally excited state become significant, with little change in the $v = 0$ populations. The population results for a sky fraction of 10^{-2} are:

λ	n_u/n_{OH}	(1-r)	Γ_a/A
82 μ	7.6×10^{-2}	.6	93
96 μ	1.8×10^{-2}	.4	100
115 μ	8.2×10^{-3}	.4	560
135 μ	3.0×10^{-3}	.3	1090

These lead to the following intensities and conditions for the Orion OH source:

λ	C^*_D	State	$\langle T_B \rangle$	I_ν (w/cm^{2}Hz str)
82 μ	6.1	F.S. K = 1	2.0×10^6 °K	8.1×10^{-13}
96 μ	8.9	P.S. a/R = 0.4	1.0×10^6 °K	3.0×10^{-13}
115 μ	9.1	P.S. a/R = 0.4	7.2×10^5 °K	1.5×10^{-13}
134 μ	9.0	P.S. a/R = 0.5	1.0×10^5 °K	1.5×10^{-13}

With the chosen parameters of:

$$\text{physical size} = 6 \times 10^{14} \text{ cm}$$

$$n_{OH} = 10^2 \text{ cm}^{-3}$$

For the W3 source the results are:

λ	C^*D	State	$\langle T_B \rangle$	I_ν(w/cm^{2}Hz str)
82 μ	11.2	P.S. a/R = 0.5	1.5×10^7 °K	6.1×10^{-12}
96 μ	13	P.S. a/R = 0.1	9×10^6 °K	2.7×10^{-12}
115 μ	11.7	P.S. a/R = 0.7	1.4×10^6 °K	2.9×10^{-13}
134 μ	10.6	U.S.	9.5×10^5 °K	1.4×10^{-13}

using:

$$\text{physical size} = 6 \times 10^{15} \text{ cm}$$

$$n_{OH} = 10^2 \text{ cm}^{-3}$$

4. Far Infrared Pumping

For the OH source in the Orion region the far infrared pumping mechanism can be appropriate for an exciting temperature of 500°K. The presence of the HII region in the vicinity of the W3 source might indicate that the exciting temperature of 2000°K could be a more valid estimate. The infrared emission in the trapezium region of the Orion source could also produce 2000°K exciting radiation for the far infrared pump. The lower pumping temperature produces a lower total intensity, so that the populations of the infrared transitions is not sufficient unless the pumping source occupies most of the sky as seen by the OH cloud. In this instance the population results for the Orion OH source are:

λ	n_u	(1-r)	Γ_a/A
96 μ	1.4×10^{-2}	0.06	76
115 μ	7.0×10^{-3}	0.27	290
135 μ	3.5×10^{-3}	0.3	130

and the emission from Orion OH is:

λ	C^*D	State	$\langle T_B \rangle$	I_ν(w/cm^{2}Hz str)
96 μ	43	P.S. a/R = 0.3	6×10^5 ^oK	1.8×10^{-13}
115 μ	23	F.S. K = 1	3.2×10^4 ^oK	6.7×10^{-15}
135 μ	20	F.S. K = 3	1.6×10^3 ^oK	2.4×10^{-16}

where the parameters used are:

$$\text{physical size} = 6 \times 10^{14} \text{ cm}$$

$$n_{OH} = 10^2 \text{ cm}^{-3}$$

At the higher pumping temperature of 2000^{o}K population inversions in the infrared lines become detectable for sky fractions above ten percent. For a sky fraction of 50 percent the far infrared lines will be strongly inverted, and the pumping rate sufficient to keep the infrared emission almost unsaturated. The population results at $\Omega_p/2\pi = 0.1$ are:

λ	n_u/n_{OH}	(1-r)	Γ_a/A
82 μ	3.0×10^{-2}	0.1	160
115 μ	9.0×10^{-3}	0.16	73
134 μ	3.2×10^{-3}	0.20	62

and at $\Omega_p/2\pi = 0.50$ the excitation results in:

λ	n_u/n_{OH}	(1-r)	Γ_a/A
82 μ	3.1×10^{-2}	0.3	800
96 μ	1.5×10^{-2}	0.1	300
115 μ	9.1×10^{-3}	0.2	250
134 μ	5.0×10^{-3}	0.1	1340

For the OH emission of the Orion region this means an intensity pattern given by the following at $\Omega_s/2\pi = 0.50$:

λ	C^*D	State	$\langle T_B \rangle$	I_ν(w/cm^{2}Hz str)
82 μ	32	P.S. a/R = .9	1.3×10^6	5.3×10^{-13}
96 μ	21	P.S. a/R = 0.5	5.7×10^5	1.7×10^{-13}
115 μ	12	P.S. a/R = 0.1	2.6×10^4	5.4×10^{-15}
134 μ	6.2	F.S. K = 1	1.0×10^3	1.5×10^{-16}

where we have used the values of:

$$\text{physical size} = 6 \times 10^{14} \text{ cm}$$

$$n_{OH} = 50 \text{ cm}^{-3}$$

For the W3 OH source the intensity pattern is:

λ	C^*D	State	$\langle T_B \rangle$	I_ν(w/cm^{2}Hz str)
82 μ	47	P.S. a/R = .5	7.2×10^6	2.9×10^{-13}
96 μ	40	P.S. a/R = .6	1.5×10^6	4.5×10^{-13}
115 μ	24	F.S. K = 2	2.8×10^5	5.9×10^{-14}
134 μ	20	P.S. a/R = 0.1	1.3×10^4	2.0×10^{-15}

$$\text{physical size} = 6 \times 10^{15} \text{ cm}$$

$$n_{OH} = 10 \text{ cm}^{-3}$$

In these last two calculations, values of n_{OH} below 10^2 cm^{-3} have been used to show that detectable IR emission can be produced even for low OH densities if the pumping is strong enough.

D. The Detectability Limit for OH Emission

The formula of Chapter IV can be used to determine the emission intensities of the OH sources in engineering units, or the characteristics of potential infrared instruments can be used to estimate the detectability limit in terms of the average brightness temperature of OH sources. Most of the current infrared instruments are designed as wideband detectors, and are mediocre tools for detecting narrow line emission in the infrared spectrum. A reasonable sensitivity limit for the narrow emission lines of the OH masers for the one meter infrared telescope of the NASA Ames Research Center when used as a broadband receiver is at an effective brightness temperature of 10^5 ^oK. At this level several of the emission lines given in the previous section would be easily detected, but distinguishing the line component may be difficult. The regions where substantial OH emission is possible are already known to have significant amounts of near and far infrared emission from extended dust clouds. Since the angular resolution of a one meter IR telescope is 20 arc seconds, or an order of magnitude larger than the OH sources, a significant amount of diffuse background radiation will also be measured. Unless care is taken to switch the beam between areas of similar background, the OH line emission will be indistinguishable from the background. The use of

high resolution infrared spectrometers can ease this difficulty and also lower the limit of detectability.

The detectability of an infrared source of limited size is set by the available integration time during the observation and the power collected by the instrument. The total power on the detector from a source smaller than the beam size with an effective brightness temperature of T_B extending over a disc of D" arc seconds in diameter in an emission line $\Delta\nu$ wide is:

$$P = 0.96 \times 10^{-13} \left(\frac{100\mu}{\lambda}\right)^3 \left(\frac{T_B}{10^5\ ^oK}\right) \left(\frac{D''}{1\ sec}\right)^2 \left(\frac{\Delta\nu/\nu}{10^{-6}}\right) \left(\frac{A}{1\ m}\right)^2 \text{ watts} \qquad \text{(VI-D-1)}$$

where A is the aperature of the instrument in meters. For a sensitivity of 3×10^{-14} watts $(Hz)^{-1/2}$ an integration time of 100 seconds will give a signal to noise of 30 if the factors in the above relation are all unity, using a detection band between 50 and 300 microns. Longer integration times will improve this figure, but guidance stability can become a problem. At this figure an effective brightness temperature of $10^5\ ^oK$ can be considered a detectable signal if the emission can be distinguished from the background. The extended W3 OH model would have an angular extent of about 2 arc seconds, therefore detectable IR emission is expected for most pumping models. The Orion OH source has a physical extent that puts D" at less than 0.1 arc seconds, thus the IR lines would be detectable only if the pumping was very strong.

E. Summary and Conclusions

A number of infrared emission lines from the OH molecule have been shown to undergo maser amplification to detectable levels from the Orion OH

and the W3 OH radio sources. The energy structure of the transition matrix of the OH molecule was carefully studied to determine the available pathways of excitation in molecular OH. A transfer equation which was coupled to the complete population solution was solved for a spherical geometry of general saturation state for the characteristic degree of saturation and intensity as controlled by the physical parameters of the cloud and the strength of the pumping. The transfer matrix of the OH molecule was then combined with the effects of pumping by ultraviolet, infrared, and collisional mechanisms to determine the population distributions and to determine the degree of population inversion occurring. These population solutions combined with the transfer equation to estimate infrared line intensities at wavelengths near one hundred microns, and to predict effective brightness temperatures between 10^5 and 10^7 ^oK for the detectable infrared lines.

Because the microwave masers are fully saturated the effects of the background radiation are minimized. Since the gain in the saturated cloud is a linear function of the diameter, adding a sizeable background brightness just allows the required size of the OH cloud to be reduced somewhat, or the pumping rate lowered. If amplified background radiation contributes one third of the emitted intensity and the background of the OH region in W3 or W49 is the infrared radiation observed nearby, then the time correlation suggested between infrared and microwave emissions can be explained as the result of varying the background component of the amplified emission. Then the variations expected in the infrared emission will be very large. The factor for the background intensity in the maser emission is nearly three orders of magnitude smaller for the infrared

lines than for the microwave lines, but the infrared emission is nearly unsaturated, so that these small variations will be greatly amplified. The infrared intensities for these OH sources would thus vary over a range at least as large as the microwave emission, to an order of magnitude greater variation.

For all the pumping models considered for the OH emission there has been at least one proposed manner in which the microwave inversions could be produced. For pumping by radiational processes a complex propagation effect is necessary in order to produce the parity selection which populates one of the lambda doublet levels over the other and hence creates the microwave emission. For infrared pumping the effects of radiation trapping in the 82 micron line are needed, and it is difficult to understand the needed amounts of trapping in regions only 10^{14} to 10^{15} cm across. The population inversion produced by a collisional pumping model which greatly simplifies the expected differential collision effects is in its simplicity a marked contrast. The collisions with moderate density H_2 molecules easily produced the needed microwave inversion even at densities which precluded detectable infrared emission, so that it is difficult to see how collisions cannot play an important role in the excitation of the OH masers.

In some of the OH sources similar to the Orion OH source the presence of large amounts of dust and other obscuration could significantly attenuate the infrared line emission; however this process itself results in significant amounts of heating for the obscuring dust, and could be a significant factor in the processes occurring in the region such as the formation of condensations and protostars. The mechanism of transferring energy from a very hot source such as an O star to the dust is easily

accomplished by such line radiation. If the OH emission is pumped by a collisional process, on the other hand, the extraction of the kinetic energy from the cloud by the infrared radiation could lead the gas and dust evolution in a different direction. It seems then that in regions where significant infrared OH emission occurs that emission can be an important element in the local evolution.

Figure 10a shows that for values of C^*D under ten there is little more than an order of magnitude between the unsaturated limit intensity and the inversion limit intensity. Since the inversion limit is the point at which the population difference becomes zero, it is expected that the intensity of the emission for small enough values of C^*D will be nearly independent of the population of the lower state. This of course is the case of integrated spontaneous emission, where

$$\langle I_\nu \rangle = \frac{(n_u/n_{OH}) n_{OH} A_{ul} h\nu \langle D \rangle}{\Delta\nu}$$

with D the physical diameter. Since most of the IR emission occurs at small values of C^*D this allows us a check of the maser calculated intensities. The 135 micron line of the collisional pumping model with $n_{H_2} = 10^4$ cm^{-3} would have a spontaneous emission of 1.9×10^{-15} w cm^{-2} Hz^{-1} str^{-1}, or less than two orders of magnitude below the maser emission, as expected. That the maser amplification only provides a gain of a hundred is not unreasonable for the relatively low populations found in the IR excited states. Further, the pumping rates, while high enough to prevent complete saturation, have the IR masers rather close to the critical core size. The exponential gain of the

maser comes only from this unsaturated core and little intensity is contributed by the saturated shell. Finally, this level of spontaneous emission is available only for the pumping described, since normal thermal mechanisms could not provide sufficient population to achieve even the above intensity.

REFERENCES

Barrett, A.H. and Lilley, A.E., 1957, Astron. J. 62, 4.

Benedict, W.S., Plyer, E.K., and Humphreys, C.J., 1953, J. Chem. Phys. 21, 3, p. 398.

Booth, 1972, Annals of N.Y. Acad. Sci. 194, 5.

Carrington, A. and Miller, T.A., 1967, Nature 214, 995.

Cheung, A.C., Rank, D.M., Townes, C.H., Thornton, D.C., and Welch, W.J., 1968, Phys. Rev. Letters 21, 1701.

Chiu, L.C., 1964, J. Chem. Phys. 40, 8, p. 2276.

Dieke, G.H. and Crosswhite, H.M., 1962, J. Quant. Spec. Rad. Trans. 2, 97.

Dousmanis, G.C., Sanders, T.M., and Townes, C.H., 1955, Phys. Rev. 100, 6, p. 1735.

Earls, L.T., 1935, Phys. Rev. 48, 423.

Elasson, B. and Bartlett, J.F., 1969, Astrophys. J. Letters 155, L79.

Fontana, P.R., 1962, Phys. Rev. 125, 1, p. 220.

Goldreich, P. and Keeley, D.A., 1972, Astrophys. J. 174, 517.

Goss, W.M., 1967, "OH Absorption in the Galaxy", Ph.D. Thesis, Univ. of California, Berkeley.

Goss, W.M. and Field, G.B., 1968, Astrophys. J. 151, 177.

Golden, D.M., DelGreco, F.P., and Kaufman, F., 1963, J. Chem. Phys. 39, 11, p. 3034.

Gunderman, E.J., 1965, "Observations of the Interstellar Hydroxyl Radical", Ph.D. Thesis, Harvard University.

Gwinn, W.D., Turner, B.E., Goss, W.M., and Blackman, G.L., 1973, Astrophys. J. 179, 789.

Heiles, C.E., 1968, Astrophys. J. 151, 919.

Herzberg, G., 1950, Molecular Spectroscopy and Molecular Structure, Vol. I, Van Nostrand Co.

Hill, E. and Van Vleck, J.H., 1928, Phys. Rev. 32, 250.

Hughes, V.A., 1967, Nature 215, 942.

d'Incan, J., Effantin, C., and Roux, F., 1971, J. Quant. Spec. Rad. Transfer 11, 1215.

Julienne, D.S. and Krauss, M., 1971, Astrophys. J. 170, 65.

Lang, R. and Bender, P.L., 1973, Astrophys. J. 180, 647.

Learner, R.C., 1962, Proc. Roy. Soc. Lon. A269, 311.

Lide, D.R., 1967, Nature 213, 694.

Litvak, M.M., 1973, Astrophys. J. 182, 711.

Litvak, M.M., 1970, Phys. Rev. A. 2, 3, p. 937.

Litvak, M.M., 1969, Astrophys. J. 156, 471.

Litvak, M.M., 1969, Science 165, 855.

Litvak, M.M., McWhorter, A.L., Meeks, M.L., and Zeiger, H.J., 1966, Phys. Rev. 17, 821.

Litvak, M.M., Zuekerman, B., and Dickinson, D.F., 1969, Astrophys. J. 156, 875.

Mezger, P.G. and Hoglund, B., 1967, Astrophys. J. 147, 490.

Murphy, R.E., 1971, J. Chem. Phys. 54, 11, p. 4852.

Rogers, A.E.E. and Barrett, A.H., 1968, Astrophys. J. 151, 163.

Shklovsky, I.S., 1966, Astr. Tsirk. no. 424.

Solomon, P.M., 1968, Nature 217, 334.

Townes, C.H., 1970, "Nonequilibrium Distribution of Molecular States in Interstellar Space", preprint University of California, Berkeley.

Turner, B.E., 1970, R.A.S.C. Jour. 64, 4, p. 221.

Turner, B.E., 1966, Nature 212, 184.

Turner, B.E. and Heiles, C., 1971, Astrophys. J. 170, 453.

Van Vleck, J.H., 1929, Phys. Rev. 33, 467.

Weaver, H.E., Williams, D.R.W., Dieter, N.H., and Lum, W.T., 1965, Nature 208, 29.

Wilson, W.J., Barrett, A.H., and Moran, J.M., 1970, Astrophys. J. 160, 545.

Zeiger, H.J., 1966, Phys. Rev. 17, 821.